


2014

Subdiffraction instrumentation development and application to the elucidation of biological systems, thin films, and organic photovoltaic devices

Michael David Lesoine
Iowa State University

Follow this and additional works at: <https://lib.dr.iastate.edu/etd>

 Part of the [Analytical Chemistry Commons](#), and the [Nanoscience and Nanotechnology Commons](#)

Recommended Citation

Lesoine, Michael David, "Subdiffraction instrumentation development and application to the elucidation of biological systems, thin films, and organic photovoltaic devices" (2014). *Graduate Theses and Dissertations*. 13893.
<https://lib.dr.iastate.edu/etd/13893>

This Dissertation is brought to you for free and open access by the Iowa State University Capstones, Theses and Dissertations at Iowa State University Digital Repository. It has been accepted for inclusion in Graduate Theses and Dissertations by an authorized administrator of Iowa State University Digital Repository. For more information, please contact digirep@iastate.edu.

Subdiffraction instrumentation development and application to the elucidation of biological systems, thin films, and organic photovoltaic devices

by

Michael D. Lesoine

A dissertation submitted to the graduate faculty
in partial fulfillment of the requirements for the degree of
DOCTOR OF PHILOSOPHY

Major: Analytical Chemistry

Program of Study Committee

Emily A. Smith, Major Professor

Joseph Burnett

Ning Fang

Mei Hong

Robert S. Houk

Iowa State University

Ames, Iowa

2014

Copyright © Michael D. Lesoine, 2014. All rights reserved.

DEDICATION

For my family past, present, and future as well as the romance that is the journey of life.

TABLE OF CONTENTS

DEDICATION	ii
TABLE OF CONTENTS	iii
ACKNOWLEDGEMENTS	v
ABSTRACT	vii
CHAPTER 1 : INTRODUCTION TO IMAGING WITH AN EMPHASIS ON DEPLETION-BASED SUBDIFFRACTION TECHNIQUES	1
Background on Imaging	1
Fluorescence and Raman Imaging	3
Subdiffraction Imaging Techniques	4
<i>Wide field imaging</i>	4
<i>Raster imaging</i>	4
<i>Axial resolution enhancement with total internal reflection</i>	5
Overview of Thesis	6
References	7
CHAPTER 2 : SUPER-CONTINUUM STIMULATED EMISSION DEPLETION (STED) FLUORESCENCE LIFETIME IMAGING	19
Abstract	19
Introduction	19
Materials and Methods	21
<i>Instrumentation.</i>	21
<i>Sample preparation.</i>	23
<i>Imaging.</i>	24
Results and Discussion	24
<i>Instrumental spatial resolution: fluorescent beads.</i>	24
<i>SC STED fluorescence lifetime imaging.</i>	26
<i>Sub-diffraction fluorescence lifetime imaging of cultured cells.</i>	27
Conclusions	29
Acknowledgements	29
References	30
CHAPTER 3 : SUBDIFFRACTION LUMINESCENCE-DEPLETION OF ISOLATED, GIANT, CdSe/CdS NANOCRYSTAL QUANTUM DOTS	39
Abstract	39
Experimental	42
<i>Sample preparation and characterization</i>	42
<i>Imaging</i>	43

Results and Discussion	44
<i>Luminescence depletion efficiencies of g-NQDs</i>	44
<i>Determination of G-NQDs on/off Time and photobleaching rates</i>	45
<i>Subdiffraction spatial resolution using g-NQDs</i>	46
Conclusions	48
Acknowledgements	49
References	49
CHAPTER 4 : HIGH ANGULAR-RESOLUTION AUTOMATED VISIBLE- WAVELENGTH SCANNING ANGLE RAMAN SPECTROSCOPY	59
Abstract	59
1. Introduction	59
2. Experimental Methods	62
2.1. <i>Instrumentation</i>	62
2.2. <i>Sample preparation</i>	63
2.3. <i>Data processing and calculations</i>	64
3. Results and Discussion	64
3.1. <i>Characterization of instrument specifications</i>	64
3.2. <i>Considerations of the excitation wavelength for SA Raman spectroscopy: Increased signal and surface sensitivity.</i>	67
3.3. <i>Considerations of the excitation wavelength for SA Raman spectroscopy: Decreased scanning angular range.</i>	68
4. Conclusions	68
Acknowledgements	69
References	69
Chapter 5 : QUANTITATIVE COMPARISON OF HIGH EFFICENCY HETEROJUNCTION SOLAR CELL STABILTY UNDER LASER INDUCED PHOTODEGRADATION	81
Abstract:	81
Introduction:	82
Experimental Methods:	83
<i>Film preparation:</i>	83
<i>Spectral measurements:</i>	84
<i>Data collection and analysis:</i>	85
Results And Discussion:	85
<i>Heterojunction solar cell's crystallinity measured by resonance Raman microscopy:</i>	85
<i>Comparison of polymer order after different annealing conditions:</i>	86
<i>Stability measurements with increasing laser power density:</i>	88
Conclusion:	89
Acknowledgments:	90
References	90
Chapter 6 : Conclusion	105

ACKNOWLEDGEMENTS

Choices are fundamental in the life we ultimately live and define the path that is followed. Along the many forks in our journey there are chance intersections where we may have the privilege to meet others that make us better simply for knowing them. Though I lack the proper eloquence to do so, I wish to thank a small fraction of the people who have had an effect on my life.

Family is an important constant that got me through my Graduate School experience. My parents John and Jean will always have my love, gratitude, and respect for supporting me in my times of hope as well as despair. Since my childhood I have been able to count on my older brother John to help this old soul and that has not changed to this day. Though not strictly “family” by the dictionary definition Matthew and Andrew are two friends who have undeniably earned the title in my eyes.

In my early academic career I encountered two individuals who greatly shaped the person I would become. Mr. Hatcher saw an ability in me to make the illogical logical, while teaching me that direction was just as important as enthusiasm. I owe the archetype of my personality to Mr. Trausche who in all honesty had one of the largest effects on my life of all the individuals I have encountered.

I would like to thank my committee for aiding me through the trials and tribulations that were Graduate life. In regards to my adviser Emily, I am glad to have had the privilege to be in her group and can only extend my heartfelt thanks for the experience. As part of the Smith Group I met many individuals who I hope to retain lasting relationships in the future Kristopher I will always admire for showing a cool head and also taking the time help me out when I was in a jam, even when he lacked the time. Vy, Aleem, Jon, and Danny had enthusiasm that helped

motivate me when I needed it the most. Even now as Jason journeys in his self-helmed schooner he still provides sage advice and counsel for which I am unequivocally grateful.

I know I am not who I was yesterday and I know I am not who I will be tomorrow. As for today, well, I think I know the answer to that...

ABSTRACT

Fluorescence and Raman instrumentation was developed to elucidate morphology, information on local environment, and material properties of target systems. Far-field fluorescence and luminescence spectroscopic measurements were performed using a pulsed super-continuum laser source and detector with high temporal resolution. With this arrangement morphologies of structures were coupled with time-correlated data. Polymeric beads and Alexa Fluor 594-phalloidin labeled cellular actin structures of cultured cells were imaged below the diffraction limit using stimulated emission depletion to resolve structures to ≈ 40 nm. Lifetime imaging revealed a 2.0 ± 0.1 ns lifetime for fluorescently-labeled beads in confocal and depletion imaging modes. Depletion imaging was also able to display a change of 2.2 to 2.9 ns for different regions of the cellular actin network of cultured cells with a possible difference in lifetime caused by tryptophan quenching of the dye. Subdiffraction imaging with a resolution of ≈ 40 nm was also accomplished using luminescence depletion of photostable giant CdSe/14CdS nanocrystal quantum dots in air. Nanocrystal quantum dots, typically not prone to depletion, exhibited this phenomenon when excited with an energy of 50 pJ and 2 nJ of depletion energy. Luminescence depletion required half the energy compared to stimulated emission depletion to achieve the same resolution limit. The luminescence was depleted by as much as $\approx 92\%$ with no observable photobleaching. Raman measurements of polymer films were performed with 532-nm laser illumination using scanning angle and conventional 180° backscattering modes to determine chemical information. The scanning angle mode achieved an angle resolution of 0.09° and was used to probe a thin layer of polystyrene as well as a diblock copolymer of polystyrene and poly(3-hexylthiophene-2,5-diyl). Enhancements to the Raman signals at selected angles lower than the critical angle for total internal reflection, characteristic of waveguides, were

measured. An additional enhancement in the Raman signal results from resonant conditions for the diblock copolymer. The epi-collection geometry was used to gain spectroscopic information regarding to the stability of heterojunction solar cells with the aid of resonance Raman spectroscopy. Raman spectral characteristics corresponding to thiophene-based functional groups were used to relate stability of the polymers under different processing conditions such as solvent and thermal annealing while undergoing laser induced photodegradation.

CHAPTER 1 : INTRODUCTION TO IMAGING WITH AN EMPHASIS ON DEPLETION-BASED SUBDIFFRACTION TECHNIQUES

Background on Imaging

Spectroscopic imaging techniques utilizing electronic, vibronic, and vibrational information can primarily be split into the categories of wide-field and point/raster imaging. In wide-field imaging the observable area can easily be on the order of hundreds of microns with collection times as fast as milliseconds to microseconds with some imaging devices. Two typical imaging devices are charged-coupled device (CCD) and complementary metal-oxide semiconductor (CMOS) cameras. Raster scanning develops an image point wise and can result in long imaging times. However, the issue of time can be alleviated by using fast scanning stages or scanning mirrors to obtain images on the order of tens of milliseconds.¹⁻³ Raster imaging typically utilizes avalanche photodiodes (APDs) and photo-multiplier tubes (PMTs) for detection. These single channel detectors provide the ability to elucidate the arrival times of collected photons allowing for the potential of additional image generation beyond the standard intensity modality.⁴⁻⁸

When imaging, the Nyquist criterion should be considered. The pixel size follows a rule of being at least half the size of the spatial resolution of the instrumentation in order to not lose any information while imaging.⁹ Figure 1 shows an example of how image pixels are generated differently in wide-field and raster imaging. In wide-field applications the generated pixel size is determined by a combination of the optics and the physical dimensions of detection elements (Figure 1A). Raster scanning relies on movements of scanning mirrors or electronic stages to determine the size of a pixel in imaging.¹⁰ The Nyquist criterion can sometimes be disregarded

when a sample has features much larger than the resolution limit or could also be easily degraded.¹¹ Figure 2 shows the consequence of using a pixel size at the resolution limit or $0.5\times$ the Nyquist criterion. The result of the former is an image with a deviation from the object. When a pixel size is below the Nyquist criterion no resolution enhancement is achieved.

The resolution of optical instrumentation is a function of the wavelength of light, numerical aperture of the optics, quality of the optics, and stability of the instrumentation for the imaging platform. Instrumentation with ideal optics is limited by diffraction as defined by Equation 1 and 2 in the lateral and axial directions, respectively.¹²

$$\text{Equation 1: } d_{x-y} = \frac{\lambda}{2 \cdot NA}$$

$$\text{Equation 2: } d_z = \frac{2 \cdot \lambda}{NA^2}$$

Where λ is the wavelength of light and NA is the numerical aperture of the optics used, while d_{x-y} is the lateral resolution (in the image plane) and d_z is the axial resolution (perpendicular to the imaging plane). It becomes apparent that to achieve the best resolution a low excitation wavelength and high NA objective should be utilized. Optics need to have limited defects and very flat surfaces to achieve a diffraction limited performance. The flatness of a reflecting optic in particular is important to preserve the wave-front of the incident laser light.¹³ Distortions to a wave-front are not necessarily apparent on a Gaussian profile, but for more complex modes such as a doughnut profile can be severely degraded.¹⁴ In order to prevent wave-front degradation thick optical substrates up to 6 mm have been utilized.^{7-8, 13} An example of 1mm versus 6 mm substrates are outlined by the point spread functions shown in Figure 3. The distortion from using the 1 mm substrate (Figure 3A) is a result of astigmatism imparted to the laser profile due to a wave-front distortion caused by the non-uniform glass surface. A thicker 6 mm substrate is less prone to having a distorted surface and yields a much more uniform profile (Figure 3B), yet

slight misalignments can still cause degradation to portions of the doughnut (Figure 3C). Image quality is also affected by vibrational considerations that can complicate wide-field in addition to laser scanning techniques. System drift can be close to a micron in scale; however, vibrations can be dampened with the use of air regulated optical tables and suitable optical mounts.¹⁵

Fluorescence and Raman Imaging

Photons emitted from endogenous or exogenous fluorescence can be measured in wide-field and raster scanning to generate images containing information about morphology as well as local environmental information. Images generated from intensity information are useful for elucidating structural information^{7, 16-17} and properties such as diffusion rates¹⁸⁻²⁰ for cellular materials.

Pulsed laser excitation on a picosecond or faster time-scale allows for lifetime determination of luminescence. In the context of biological systems the lifetime associated with a fluorophore can be effected by different cellular conditions such as pH.²¹⁻²³ In addition, interactions of molecules with dyes, such as the quenching effect tryptophan has on rhodamine dyes, can give useful information as to a cell's local environment.²⁴⁻²⁸

Changes in vibrational states are utilized in Raman spectroscopy to generate morphological information coupled to chemical information. Images following a wide-field scheme use specific Raman shifts and can utilize devices such as an acousto-optical tunable filter (AOTF). An AOTF allows the precise changes to the wavenumber regions being observed to focus on different Raman shifts for the molecule(s) of interest.²⁹⁻³⁰ In this way the abundance of spectral features can be generated with a series of images of wavenumber regions. Raster scanning is another avenue to Raman image generation where spectra are collected point wise using a spectroscopic CCD.³¹⁻³²

Subdiffraction Imaging Techniques

Diffraction that limits the resolution of features closer than about 200-300 nm in the visible spectrum can be overcome in far-field optical microscopies, which have benefits over near-field techniques. When imaging biological samples important information can be convoluted within a diffraction limited volume. Techniques such as transmission electron microscopy (TEM) could resolve features in biological systems; however, the requirement of a vacuum prevents the use of physiological conditions. Fluorescence imaging techniques can be run under physiological conditions, and have the benefit of simplified sample preparation when compared to TEM. An example of the resolution enhancement possible with fluorescence is shown in Figure 4 where a mass of fluorescent beads are convoluted by diffraction (A) and resolved (B) to individual beads.

Wide field imaging

Subdiffraction images can be obtained in the wide-field from techniques such as stochastic optical reconstruction microscopy (STORM)³³⁻³⁶ and photo-activated localization microscopy (PALM)³⁷⁻³⁸. STORM³³ and PALM³⁷⁻³⁸ are very similar techniques that take advantage of the stochastic nature of on or off events from fluorescent labels and endogenous fluorophores. Image reconstruction algorithms localize the fluorescence emission and can yield resolutions of ~20 nm or better in the lateral direction.^{33-34, 36-38}

Raster imaging

Point scanning techniques that achieve subdiffraction spatial resolutions typically follow a confocal laser scanning format. These techniques include luminescence depletion (LD)⁸, stimulated emission depletion (STED)^{7, 39-41}, and ground state depletion (GSD)⁴²⁻⁴³ microscopies.

LD, STED, and GSD are similar techniques that make use of a doughnut shaped depletion beam to deplete the emission of luminescence from the periphery of a Gaussian shaped excitation beam. The area around the Gaussian excitation beam is sent to the ground state in the case of LD and STED and excited to long lived dark states for GSD. For all three techniques the signal intensity remaining at the doughnut's center is of a subdiffraction size. The lateral resolutions that are typically obtained are routinely below 50-nm regime with sufficient power in the depletion beam.^{5, 7-8, 37, 43-47} Resolutions for the techniques of LD and STED may be optimized by time-gating the data by removing photons from time points that have not been completely or sufficiently depleted.^{6-8, 48} The improvement to the measured lateral resolution for the subdiffraction modalities have been shown to increase by at least a factor of two.⁷⁻⁸

Depletion techniques depend heavily on the quality of the doughnut and Gaussian profile uniformity and overlap. When astigmatism is present in the system Figure 5 depicts the confocal (A) and STED (B) modes with the resulting resolution enhancement, which occurs in only one direction for STED. Overfilling the objective with removal of astigmatism (Figure 5C) from the imaging system gives uniform resolution enhancement, but still can leave imaging artifacts from fringes where depletion has not occurred (Figure 5D). Underfilling the objective causes a decrease in the measured resolution for a confocal image (Figure 5E); however, the artifacts from the fringes are removed as depicted in the STED image in Figure 5F. The preparation for the fluorescence microspheres is the same as previously reported.⁷

Axial resolution enhancement with total internal reflection

Total internal reflection (TIR) is a technique used to obtain subdiffraction axial resolution with improved detection limits.⁴⁹ The improvement to axial resolution is generated by probing a

sample with illumination incident at an angle greater than a critical value determined by Snell's law (Equation 3).

$$\text{Equation 3: } \theta_c = \sin^{-1} \left(\frac{\eta_{\text{sample}}}{\eta_{\text{prism/objective}}} \right)$$

The critical angle, refractive index of the sample, and refractive index of the prism or objective used correspond to θ_c , η_{sample} , and $\eta_{\text{prism/objective}}$, respectively. From Equation 2 the diffraction limited axial resolution in the visible spectrum is approximately 500-1000 nm. For 532 nm excitation the penetration depth over which signal is collected for a sapphire/polystyrene interface reaches a minimum of approximately 60 nm at higher incident angles (Figure 6). This is about an order of magnitude improvement over the diffraction limit. In addition to an improvement in the axial resolution, the detection limit for TIR is improved by an enhancement in the signal at the critical angle with a reduction in the background.⁴⁹ Ultimately, this improves the signal-to-noise ratio compared to epi-illumination.⁴⁹

Through the objective and through a high index of refraction prism are two variants used for TIR.⁵⁰⁻⁶⁰ Through the objective TIR uses a wide-field scheme to generate images over a large field of view on the order of tens of microns. TIR through a prism generates images of Raman scattering data as a function of known incident angles and can be used to model properties such as thickness.^{57, 59-60}

Overview of Thesis

The material presented covers: (1) the development and application of a lab-built stimulated emission depletion (STED) microscope and (2) a lab-built scanning angle and conventional Raman microscope's validation and application. Chapter 1 gave a brief overview of imaging fundamentals and techniques that can be used to circumvent the diffraction barrier in the lateral and axial directions. Fluorescently-labeled polystyrene beads and the elucidation of

the F-actin structure present in the cytoskeleton of cultured cells measured by STED microscopy make up the focus of chapter 2. LD microscopy is discussed in chapter 3 utilizing giant nanocrystal quantum dots in air to achieve subdiffraction imaging. Chapter 4 covers the instrumentation for a 532-nm SA Raman microscope and its application to measuring thin films by taking advantage of resonance Raman spectroscopy. In addition, an increased signal from an enhanced surface sensitivity when compared to 785 nm excitation is examined. The focus of chapter 5 is bulk heterojunction solar films with order determinations for different preparation conditions and also while undergoing laser induced photodegradation. Further utility to the work presented is covered in chapter 6 with a brief review and implications to future research.

References

1. Westphal, V.; Rizzoli, S. O.; Lauterbach, M. A.; Kamin, D.; Jahn, R.; Hell, S. W., Video-Rate Far-Field Optical Nanoscopy Dissects Synaptic Vesicle Movement. *Science* 2008, 320 (5873), 246-249.
2. Lauterbach, M. A.; Keller, J.; Schönle, A.; Kamin, D.; Westphal, V.; Rizzoli, S. O.; Hell, S. W., Comparing video-rate STED nanoscopy and confocal microscopy of living neurons. *Journal of Biophotonics* 2010, 3 (7), 417-424.
3. Lee, J.; Miyanaga, Y.; Ueda, M.; Hohng, S., Video-Rate Confocal Microscopy for Single-Molecule Imaging in Live Cells and Superresolution Fluorescence Imaging. *Biophysical Journal* 103 (8), 1691-1697.
4. Auksorius, E.; Boruah, B. R.; Dunsby, C.; Lanigan, P. M. P.; Kennedy, G.; Neil, M. A. A.; French, P. M. W., Stimulated emission depletion microscopy with a supercontinuum source and fluorescence lifetime imaging. *Opt. Lett.* 2008, 33 (2), 113-115.
5. Bückers, J.; Wildanger, D.; Vicidomini, G.; Kastrup, L.; Hell, S. W., Simultaneous multi-lifetime multi-color STED imaging for colocalization analyses. *Opt. Express* 2011, 19 (4), 3130-3143.
6. Vicidomini, G.; Moneron, G.; Han, K. Y.; Westphal, V.; Ta, H.; Reuss, M.; Engelhardt, J.; Eggeling, C.; Hell, S. W., Sharper low-power STED nanoscopy by time gating. *Nat Meth* 2011, 8 (7), 571-573.

7. Lesoine, M. D.; Bose, S.; Petrich, J. W.; Smith, E. A., Supercontinuum Stimulated Emission Depletion Fluorescence Lifetime Imaging. *The Journal of Physical Chemistry B* 2012, 116 (27), 7821-7826.
8. Lesoine, M. D.; Bhattacharjee, U.; Guo, Y.; Vela, J.; Petrich, J. W.; Smith, E. A., Subdiffraction, Luminescence-Depletion Imaging of Isolated, Giant, CdSe/CdS Nanocrystal Quantum Dots. *The Journal of Physical Chemistry C* 2013, 117 (7), 3662-3667.
9. The Digital Image. In *Optical Imaging Techniques in Cell Biology*, CRC Press: 2006; pp 77-85.
10. Paddock, S., Over the rainbow: 25 years of confocal imaging. *BioTechniques* 2008, 44 (5), 643-4, 646, 648.
11. Gao, Y.; Grey, J. K., Resonance Chemical Imaging of Polythiophene/Fullerene Photovoltaic Thin Films: Mapping Morphology-Dependent Aggregated and Unaggregated C=C Species. *Journal of the American Chemical Society* 2009, 131 (28), 9654-9662.
12. Abbe, E., Beiträge zur Theorie des Mikroskops und der mikroskopischen Wahrnehmung. *Archiv für Mikroskopische Anatomie* 1873, 9 (1), 413-418.
13. Lauterbach, M. *Fast STED Microscopy*. Universität Göttingen, Göttingen, 2009.
14. Boruah, B. R.; Neil, M. A., Susceptibility to and correction of azimuthal aberrations in singular light beams. *Optics Express* 2006, 14 (22), 10377-10385.
15. Fisher, J.; Ryaboy, V. M., Effective vibration reduction stabilizes laser beams. *Laser Focus World* 2008, 44 (8), 92-97.
16. Madisen, L.; Zwingman, T. A.; Sunkin, S. M.; Seung Wook, O.; Zariwala, H. A.; Hong, G.; Ng, L. L.; Palmiter, R. D.; Hawrylycz, M. J.; Jones, A. R.; Lein, E. S.; Hongkui, Z., A robust and high-throughput Cre reporting and characterization system for the whole mouse brain. *Nature Neuroscience* 2010, 13 (1), 133-140.
17. Eng, J.; Lynch, R. M.; Balaban, R. S., Nicotinamide adenine dinucleotide fluorescence spectroscopy and imaging of isolated cardiac myocytes. *Biophysical Journal* 1989, 55 (4), 621-630.
18. Sander, S.; Arora, N.; Smith, E., Elucidating the role of select cytoplasmic proteins in altering diffusion of integrin receptors. *Analytical & Bioanalytical Chemistry* 2012, 403 (8), 2327-2337.

19. Arora, N.; Mainali, D.; Smith, E., Unraveling the role of membrane proteins Notch, Pvr, and EGFR in altering integrin diffusion and clustering. *Analytical & Bioanalytical Chemistry* 2012, 404 (8), 2339-2348.
20. Mainali, D.; Smith, E., Select cytoplasmic and membrane proteins increase the percentage of immobile integrins but do not affect the average diffusion coefficient of mobile integrins. *Anal Bioanal Chem* 2013, 405 (26), 8561-8568.
21. Tantama, M.; Hung, Y. P.; Yellen, G., Imaging Intracellular pH in Live Cells with a Genetically Encoded Red Fluorescent Protein Sensor. *Journal of the American Chemical Society* 2011, 133 (26), 10034-10037.
22. Islam, M.; Honma, M.; Nakabayashi, T.; Kinjo, M.; Ohta, N., pH Dependence of the Fluorescence Lifetime of FAD in Solution and in Cells. *International Journal of Molecular Sciences* 2013, 14 (1), 1952-1963.
23. Orte, A.; Alvarez-Pez, J. M.; Ruedas-Rama, M. J., Fluorescence Lifetime Imaging Microscopy for the Detection of Intracellular pH with Quantum Dot Nanosensors. *ACS Nano* 2013, 7 (7), 6387-6395.
24. Marmé, N.; Knemeyer, J.-P.; Sauer, M.; Wolfrum, J., Inter- and Intramolecular Fluorescence Quenching of Organic Dyes by Tryptophan. *Bioconjugate Chem.* 2003, 14 (6), 1133-1139.
25. Chen, Y.; Vela, J.; Htoon, H.; Casson, J. L.; Werder, D. J.; Bussian, D. A.; Klimov, V. I.; Hollingsworth, J. A., "Giant" Multishell CdSe Nanocrystal Quantum Dots with Suppressed Blinking. *Journal of the American Chemical Society* 2008, 130 (15), 5026-5027.
26. Chen, H.; Ahsan, S. S.; Santiago-Berrios, M. E. B.; Abruña, H. D.; Webb, W. W., Mechanisms of Quenching of Alexa Fluorophores by Natural Amino Acids. *Journal of the American Chemical Society* 2010, 132 (21), 7244-7245.
27. Mansoor, S. E.; DeWitt, M. A.; Farrens, D. L., Distance Mapping in Proteins Using Fluorescence Spectroscopy: The Tryptophan-Induced Quenching (TriQ) Method. *Biochemistry* 2010, 49 (45), 9722-9731.
28. Doose, S.; Neuweiler, H.; Sauer, M., A Close Look at Fluorescence Quenching of Organic Dyes by Tryptophan. *ChemPhysChem* 2005, 6 (11), 2277-2285.
29. Treado, P. J.; Levin, I. W.; Lewis, E. N., High-Fidelity Raman Imaging Spectrometry: A Rapid Method Using an Acousto-optic Tunable Filter. *Applied Spectroscopy* 1992, 46 (8), 1211-1216.

30. Morris, H. R.; Hoyt, C. C.; Treado, P. J., Imaging Spectrometers for Fluorescence and Raman Microscopy: Acousto-Optic and Liquid Crystal Tunable Filters. *Applied Spectroscopy* 1994, 48 (7), 857-866.
31. Uzunbajakava, N.; Lenferink, A.; Kraan, Y.; Volokhina, E.; Vrensen, G.; Greve, J.; Otto, C., Nonresonant Confocal Raman Imaging of DNA and Protein Distribution in Apoptotic Cells. *Biophysical Journal* 2003, 84 (6), 3968-3981.
32. Lee, K. E.; Gomez, M. A.; Elouatik, S.; Demopoulos, G. P., Further Understanding of the Adsorption Mechanism of N719 Sensitizer on Anatase TiO₂ Films for DSSC Applications Using Vibrational Spectroscopy and Confocal Raman Imaging. *Langmuir* 2010, 26 (12), 9575-9583.
33. Rust, M. J.; Bates, M.; Zhuang, X., Sub-diffraction-limit imaging by stochastic optical reconstruction microscopy (STORM). *Nat Meth* 2006, 3 (10), 793-796.
34. Huang, B.; Wang, W.; Bates, M.; Zhuang, X., Three-Dimensional Super-Resolution Imaging by Stochastic Optical Reconstruction Microscopy. *Science* 2008, 319 (5864), 810-813.
35. Bates, M.; Huang, B.; Dempsey, G. T.; Zhuang, X., Multicolor Super-Resolution Imaging with Photo-Switchable Fluorescent Probes. *Science* 2007, 317 (5845), 1749-1753.
36. Huang, B.; Jones, S. A.; Brandenburg, B.; Zhuang, X., Whole-cell 3D STORM reveals interactions between cellular structures with nanometer-scale resolution. *Nat Meth* 2008, 5 (12), 1047-1052.
37. Betzig, E.; Patterson, G. H.; Sougrat, R.; Lindwasser, O. W.; Olenych, S.; Bonifacino, J. S.; Davidson, M. W.; Lippincott-Schwartz, J.; Hess, H. F., Imaging Intracellular Fluorescent Proteins at Nanometer Resolution. *Science* 2006, 313 (5793), 1642-1645.
38. Boldt, K.; Bruns, O. T.; Gaponik, N.; Eychmüller, A., Comparative Examination of the Stability of Semiconductor Quantum Dots in Various Biochemical Buffers. *The Journal of Physical Chemistry B* 2006, 110 (5), 1959-1963.
39. Hell, S. W.; Wichmann, J., Breaking the diffraction resolution limit by stimulated emission: stimulated-emission-depletion fluorescence microscopy. *Opt. Lett.* 1994, 19 (11), 780-782.
40. Klar, T. A.; Hell, S. W., Subdiffraction resolution in far-field fluorescence microscopy. *Opt. Lett.* 1999, 24 (14), 954-956.
41. Syed, A.; Lesoine, M. D.; Bhattacharjee, U.; Petrich, J. W.; Smith, E. A., The Number of Accumulated Photons and the Quality of Stimulated Emission Depletion Lifetime Images. *Photochemistry and Photobiology* 2014, n/a-n/a.

42. Hell, S. W.; Kroug, M., Ground-state-depletion fluorescence microscopy: A concept for breaking the diffraction resolution limit. *Appl. Phys. B* 1995, 60 (5), 495-497.
43. Bretschneider, S.; Eggeling, C.; Hell, S. W., Breaking the Diffraction Barrier in Fluorescence Microscopy by Optical Shelving. *Physical Review Letters* 2007, 98 (21), 218103.
44. Willig, K. I.; Keller, J.; Bossi, M.; Hell, S. W., STED microscopy resolves nanoparticle assemblies. *New Journal of Physics* 2006, 8 (6), 106-106.
45. Willig, K. I.; Kellner, R. R.; Medda, R.; Hein, B.; Jakobs, S.; Hell, S. W., Nanoscale resolution in GFP-based microscopy. *Nat. Methods* 2006, 3 (9), 721-723.
46. Wildanger, D.; Rittweger, E.; Kastrup, L.; Hell, S. W., STED microscopy with a supercontinuum laser source. *Opt. Express* 2008, 16 (13), 9614-9621.
47. Wildanger, D.; Medda, R.; Kastrup, L.; Hell, S. W., A compact STED microscope providing 3D nanoscale resolution. *Journal of Microscopy* 2009, 236 (1), 35-43.
48. Leutenegger, M.; Eggeling, C.; Hell, S. W., Analytical description of STED microscopy performance. *Opt. Express* 2010, 18 (25), 26417-26429.
49. Paige, M. F.; Bjerneld, E. J.; Moerner, W. E., A Comparison of Through-the-Objective Total Internal Reflection Microscopy and Epifluorescence Microscopy for Single-Molecule Fluorescence Imaging. *Single Molecules* 2001, 2 (3), 191-201.
50. Fujiwara, K.; Watarai, H., Total Internal Reflection Resonance Raman Microspectroscopy for the Liquid/Liquid Interface. Ion-Association Adsorption of Cationic Mn(III) Porphine. *Langmuir* 2003, 19 (7), 2658-2664.
51. Greene, P., Total internal reflection Raman spectroscopy. *SpectroscopyEurope* 2004, 16 (4).
52. Greene, P. R.; Bain, C. D., *Spectroscopy Europe* 2004, 16 (8), 8-15.
53. Tisinger, L. G.; Sommer, A. J., Attenuated Total Internal Reflection (ATR) Raman Microspectroscopy. *Microscopy and Microanalysis* 2004, 10 (Supplement S02), 1318-1319.
54. Greene, P. R.; Bain, C. D., Total internal reflection Raman spectroscopy of barley leaf epicuticular waxes in vivo. *Colloids and Surfaces B: Biointerfaces* 2005, 45 (3-4), 174-180.
55. Beattie, D. A.; Larsson, M. L.; Holmgren, A. R., In situ total internal reflection Raman spectroscopy of surfactant adsorption at a mineral surface. *Vibrational Spectroscopy* 2006, 41 (2), 198-204.

56. McKee, K. J.; Smith, E. A., Development of a scanning angle total internal reflection Raman spectrometer. *Review of Scientific Instruments* 2010, 81 (4), -.
57. McKee, K. J.; Meyer, M. W.; Smith, E. A., Near IR Scanning Angle Total Internal Reflection Raman Spectroscopy at Smooth Gold Films. *Analytical Chemistry* 2012, 84 (10), 4300-4306.
58. Woods, D. A.; Bain, C. D., Total internal reflection Raman spectroscopy. *Analyst* 2012, 137 (1), 35-48.
59. Meyer, M. W.; McKee, K. J.; Nguyen, V. H. T.; Smith, E. A., Scanning Angle Plasmon Waveguide Resonance Raman Spectroscopy for the Analysis of Thin Polystyrene Films. *The Journal of Physical Chemistry C* 2012, 116 (47), 24987-24992.
60. Meyer, M. W.; Nguyen, V. H. T.; Smith, E. A., Scanning angle Raman spectroscopy measurements of thin polymer films for thickness and composition analyses. *Vibrational Spectroscopy* 2013, 65 (0), 94-100.

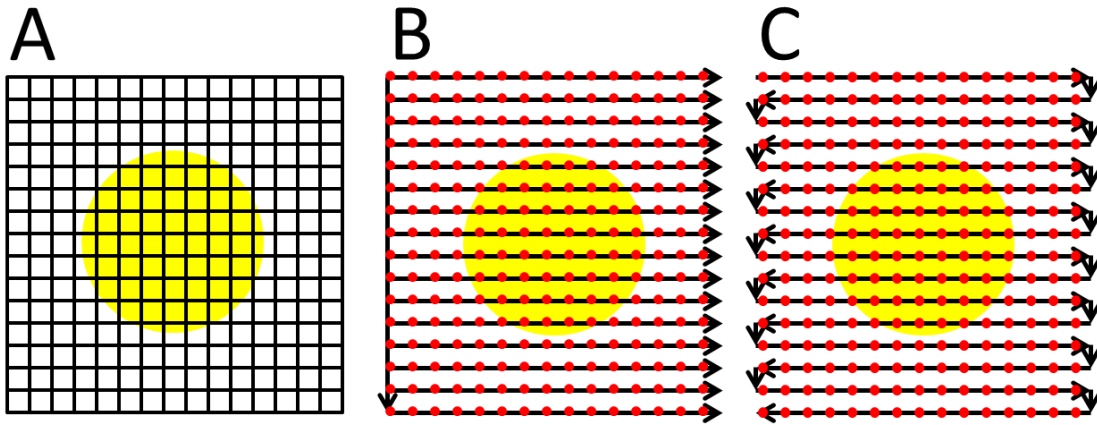


Figure 1 : An object of interest (large yellow circle) is observed as if it was imaged in the wide-field (A), raster scanning (B), or a variant of point scanning (C). The squares in A depict the pixels on a CCD or CMOS. The direction of the arrows outline the progression of image acquisition and the red dots correspond to discrete points where image data is acquired.

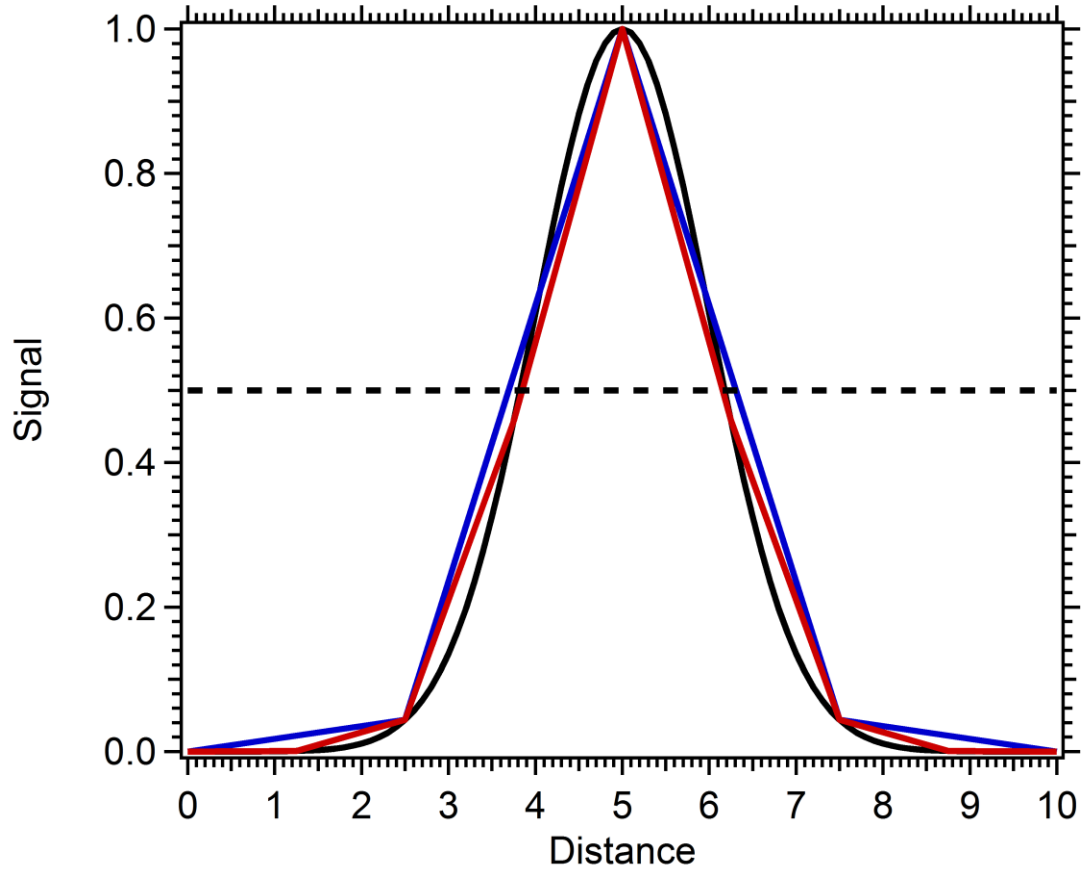


Figure 2 : A theoretically generated Gaussian function with a FWHM of 2.35 sampled at 10× (black), 1× (red), and 0.5× (blue) the Nyquist criterion (1.675). The black dotted line corresponds to the FWHM.

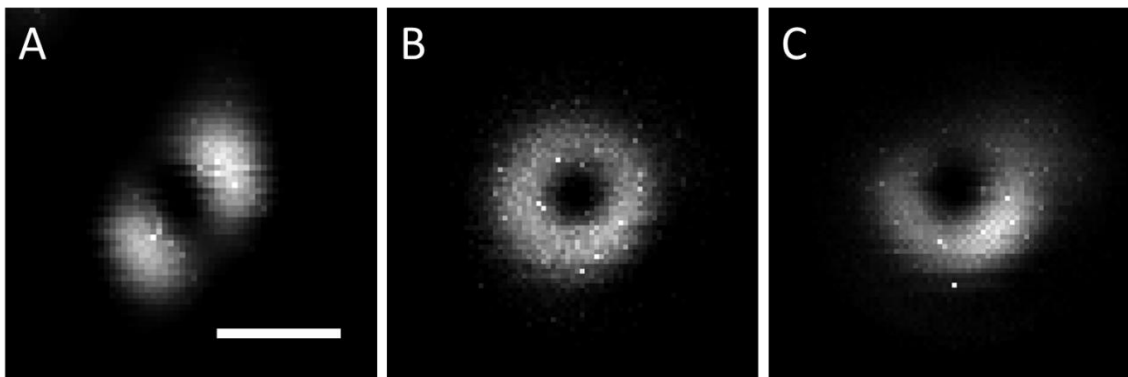


Figure 3 : Doughnut profiles generated with 1 mm (A) and 6 mm (B-C) thick dichroic mirrors. Scale-bar equals 500 nm.

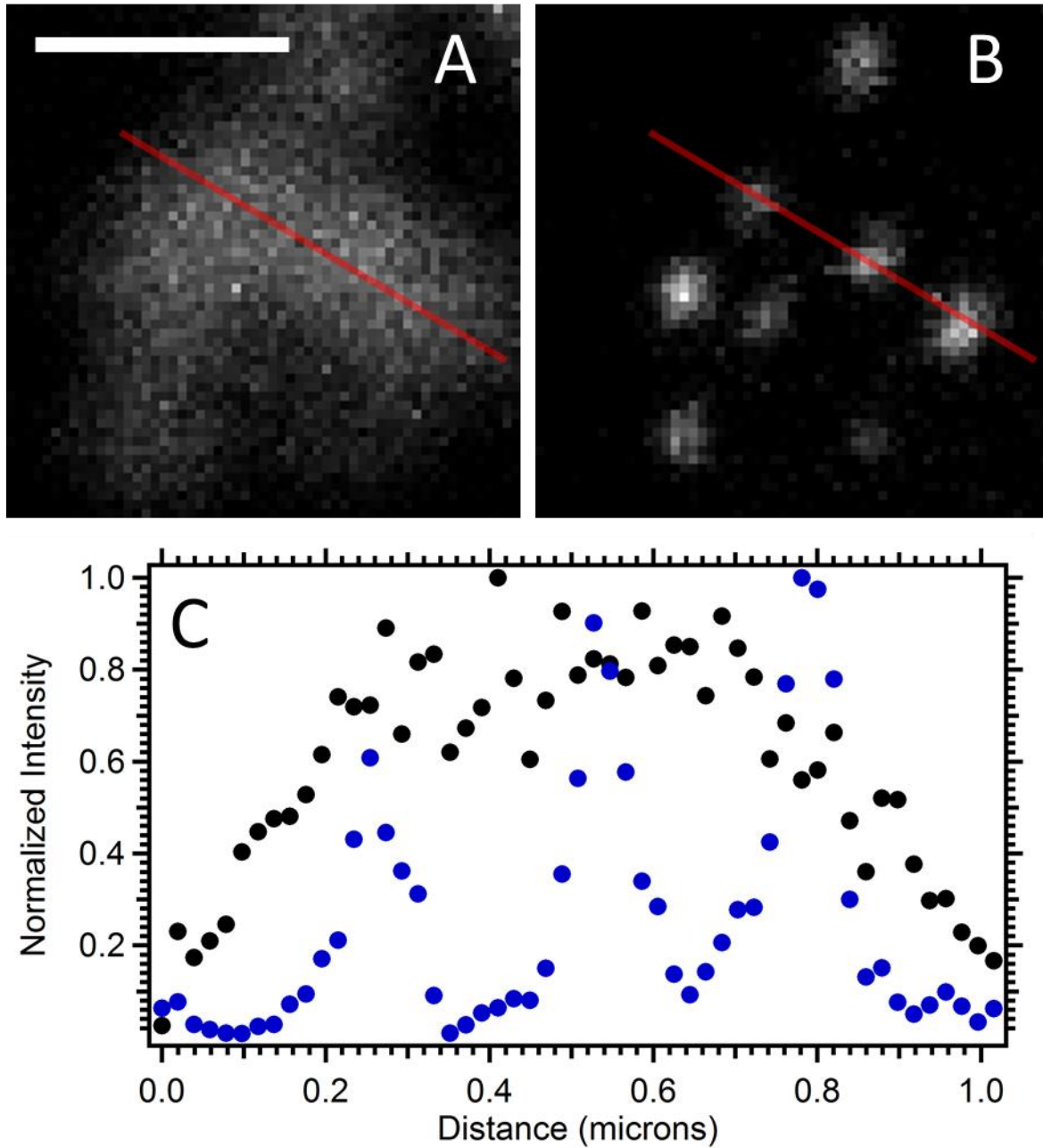


Figure 4 : Fluorescently labeled microspheres imaged at the diffraction limit (A) and with subdiffraction resolution (B). The red lines correspond to where cross-sections were measured and plotted in (C) for diffraction limited (black circles) and subdiffraction (blue circles) data. Scale-bar corresponds to a distance of 500 nm.

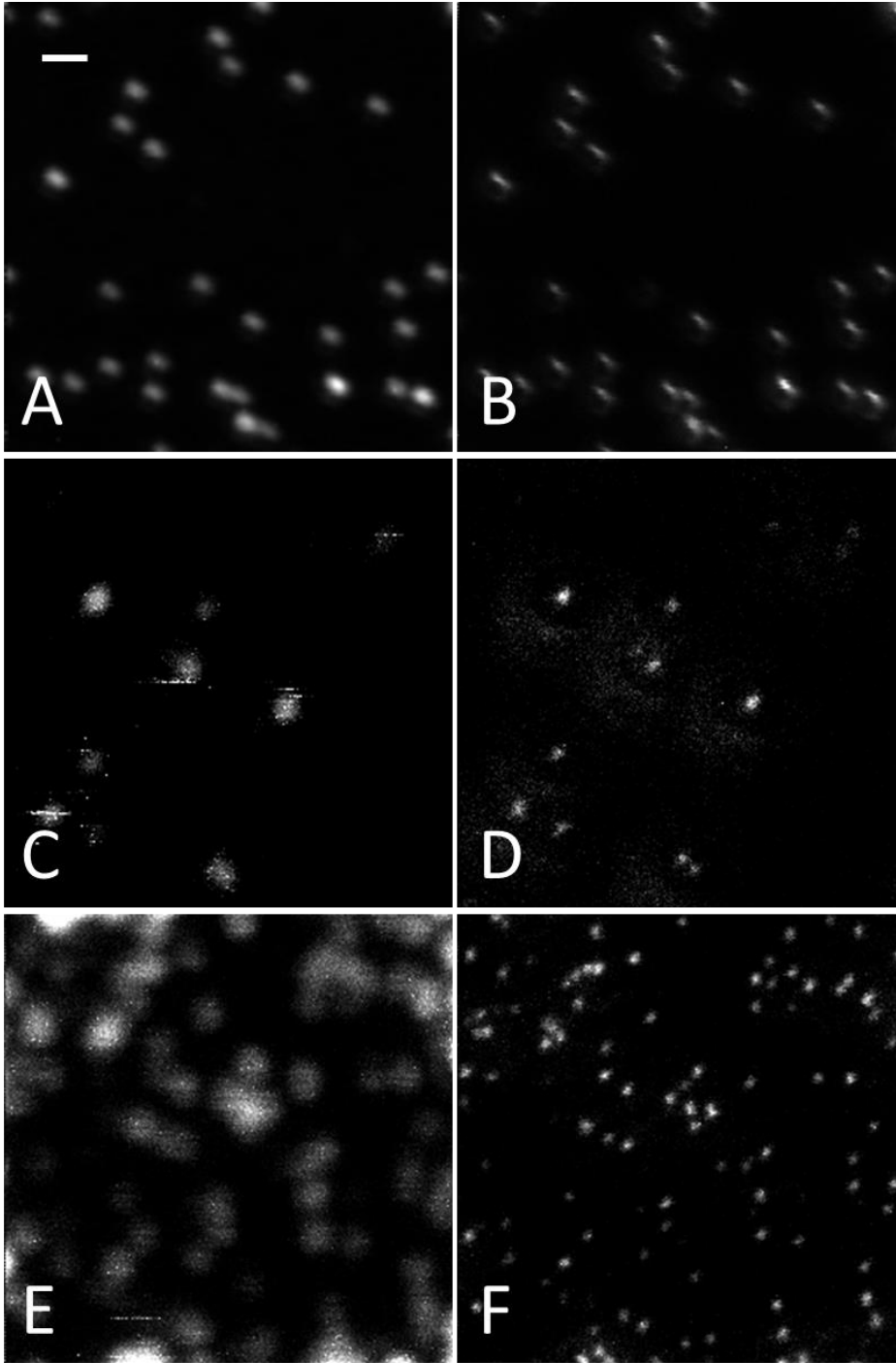


Figure 5 : Confocal (A,C,E) and STED (B,D,F) images of 40-nm fluorescent microspheres. Astigmatism is present in (A) and (B), the objective is overfilled and underfilled with the Gaussian excitation profile for (C-D) and (E-F), respectively. Powers of 1 pJ and 2.5 nJ were used for confocal and STED modes, respectively. The Scale-bar corresponds to a distance of 500 nm.

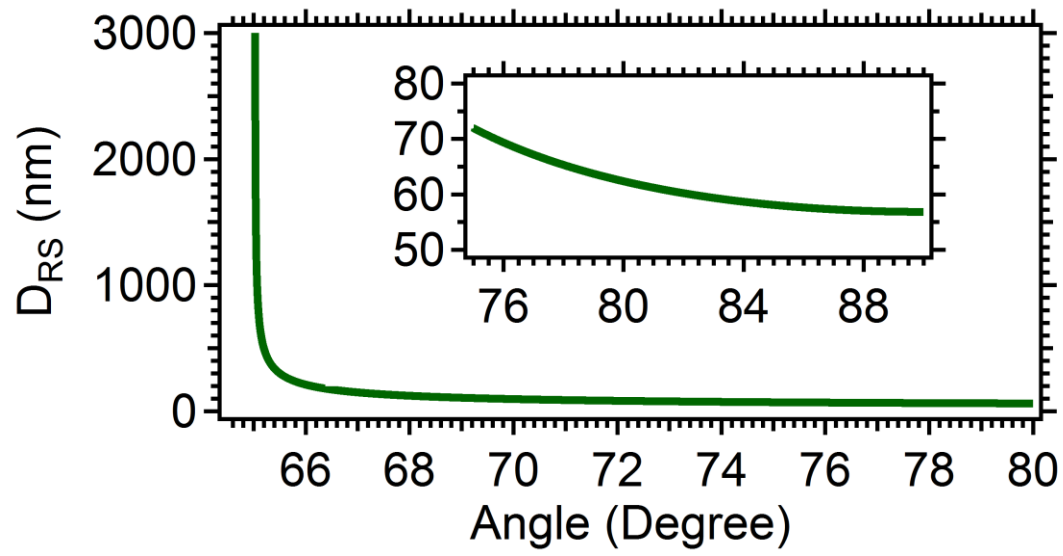


Figure 6 : Penetration depth for 532 nm excitation of a sapphire/polystyrene interface as a function of incident angle.

CHAPTER 2 : SUPER-CONTINUUM STIMULATED EMISSION DEPLETION (STED) FLUORESCENCE LIFETIME IMAGING

Reproduced with permission from [Lesoine, M. D.; Bose, S.; Petrich, J. W.; Smith, E. A., Supercontinuum Stimulated Emission Depletion Fluorescence Lifetime Imaging. *The Journal of Physical Chemistry B* 2012, 116 (27), 7821-7826.] Copyright [2014] American Chemical Society.

Michael D. Lesoine, Sayantan Bose, Jacob W. Petrich, and Emily A. Smith

Abstract

Super-continuum (SC) stimulated emission depletion (STED) fluorescence lifetime imaging is demonstrated using time-correlated single-photon counting (TCSPC) detection. The spatial resolution of the developed STED instrument was measured by imaging monodispersed 40-nm fluorescent beads and then determining their FWHM, and was 36 ± 9 and 40 ± 10 nm in the X and Y coordinates, respectively. The same beads measured by confocal microscopy were 450 ± 50 and 430 ± 30 nm, which is larger than the diffraction limit of light due to under filling the microscope objective. Under filling the objective and time gating the signal were necessary to achieve the stated STED spatial resolution. The same fluorescence lifetime (2.0 ± 0.1 ns) was measured for the fluorescent beads using confocal or STED lifetime imaging. The instrument has been applied to study Alexa Fluor 594-phalloidin labeled F-actin-rich projections with dimensions smaller than the diffraction limit of light in cultured cells. Fluorescence lifetimes of the actin-rich projections range from 2.2 to 2.9 ns as measured by STED lifetime imaging.

Introduction

Diffraction limits traditional far-field optical microscopies to a lateral resolution of $\sim \lambda/2NA$, where λ is the wavelength of light and NA is the numerical aperture of the optical system.¹ The diffraction limit is greater than 200 nanometers using visible wavelengths. There

are several optical imaging techniques that circumvent the diffraction limit and enable the study of phenomena that occur in sub-diffraction spatial regimes. Stochastic techniques such as stochastic optical reconstruction microscopy (STORM) rely on turning a subset of fluorophores on and then off in combination with localization procedures.² Near-field techniques require a probe in close proximity to the sample, and may not be suitable for corrugated or sensitive samples.³ Hell and coworkers⁴⁻¹⁰ described and demonstrated the technique referred to as stimulated emission depletion (STED), whereby the diffraction limited resolution in far-field fluorescence microscopy is circumvented using point spread function engineering.

The basic operating principle of STED microscopy is inhibiting the fluorescence at the periphery of a diffraction limited spot by stimulated emission. A tightly-focused, scanning excitation laser pulse of tens-of-picoseconds duration and a toroid-shaped STED laser pulse of hundreds-of-picosecond duration are used. The STED pulse is shaped by phase modulation, and has zero intensity at its center. The stimulated emission pulse depopulates the excited electronic states of the fluorophores within the toroidal beam profile, leaving a spot of excited fluorophores, which is smaller than the diffraction limit, at the center of the toroid. The net result enables signal collection from an excitation volume that is smaller than the dimensions set by diffraction. Resolution in the 15-20-nm range has been reported, with molecular-scale resolution fluorescence measurements fundamentally possible in the far-field.⁵ STED has been demonstrated using various instrumental configurations. The use of pulsed lasers is well-suited to gating the fluorescence signal, while continuous-wave lasers simplify the instrumentation and are a cost-effective choice. Spatial light modulators or vortex phase plates are commonly used to generate the required STED toroid profile.^{7,9,11} Crucial to achieving optimum spatial resolution is the ability to obtain a minimum approaching zero in the toroid. STED microscopy using a

super-continuum (SC) laser to supply both the excitation and STED wavelengths simplifies instrument setup, and the wavelength tunability opens the possibility of using an increased range of dyes.^{11,12} A ~9-fold improvement in the lateral (i.e., in the focal plane) spatial resolution has been reported with SC STED microscopy.^{11,13}

Besides obtaining sub-diffraction resolution images, STED can be coupled with fluorescence-lifetime imaging microscopy (FLIM) to perform time-resolved experiments^{12,14} and to acquire lifetime images. Time-gating the signal has been shown to improve signal-to-background values noticeably and also to improve the spatial resolution.¹² Time-gating improves the lateral resolution by selectively rejecting photons from signal not originating from the center of the toroid. To date, a few groups have used TCSPC in STED experiments, but have not exploited the ability of this photon counting technique to obtain kinetic data from sub-diffraction spots.^{12,14,15} Hell and coworkers have, however, used lifetimes obtained from TCSPC to distinguish different fluorophores.¹⁴ Fluorescence lifetime measurements provide details about molecular dynamics and molecular environments, and when combined with STED can reveal information about local environments on the tens-of-nanometer scale. Herein, SC STED fluorescence lifetime microscopy is demonstrated and tested using two very different systems: monodispersed, fluorescent beads and Alexa Fluor 594-phalloidin labeled actin fibers in cultured cells. The data show that high quality fluorescence lifetime data can be obtained in sub-diffraction spots as small as 36-40 nm in diameter.

Materials and Methods

Instrumentation.

Figure 1 shows a schematic of the home-built STED microscope that uses a SC laser (SC-450-pp-he, Fianium, Southampton, UK) for the excitation and STED pulses, which ensures

that both pulses are inherently synchronized. A 2-MHz repetition rate is used to limit photobleaching of the fluorophore. The energies of the excitation and STED pulses are 1 pJ and 4 nJ, as measured before the microscope objective. The instrument response functions for the excitation and STED pulses are 90 and 150 ps, respectively, as measured by the traditional method of monitoring the profile obtained from light scattered from a suspension of nonfluorescent nondairy creamer in water. Dielectric mirrors are used in the beam paths (10Q20BB.1, Newport, Irvine, California) to remove the infrared wavelengths from the SC.

The laser output is initially split using a polarizing beam cube (DMLP605R, Thorlabs, Newton, New Jersey). Band-pass filters isolate the desired wavelengths for the excitation (570 ± 5 nm, product Z570/10X, Chroma, Bellows Falls, Vermont) and STED beams (695 ± 10 nm, product D695/20, Chroma). Half-wave plates (AHWP05M-600, Thorlabs) are used in both beam paths to ensure matching polarizations. The toroidal STED beam is generated using a vortex phase plate (RPC Photonics, Rochester, NY, USA), which attenuates the intensity at the center of the beam profile by 99.7% (Figure 2). An optical delay line is also added to the STED path to ensure the desired temporal profile of the excitation and STED pulses, where the latter precedes the excitation pulse with a peak to peak difference of ~ 80 -ps. The STED pulse needs to lag behind the excitation pulse enough to allow the latter to populate the excited state, before the arrival of the STED pulse. The STED beam profile was measured as previously reported.¹⁶ Beam expanders are used in both the excitation and STED paths to adjust the beam-size and spatially filter the beam. The beams are recombined with a dichroic mirror (ZT594RDC, Chroma). A quarter-wave plate (AQWP05M-600, Thorlabs) placed before the microscope generates circular polarization, which has been previously shown to optimize the STED signal.¹⁷

The collinear pulses are directed to a microscope (Eclipse Ti, Nikon, Melville, New York) objective (CFI Apo TIRF 100x, 1.49 NA, Nikon) using a dichroic mirror (635-70BPDC, Chroma) that reflects both the excitation and STED wavelengths while allowing transmission of the resulting fluorescence. The excitation pulse slightly under fills the objective to minimize artifacts in the periphery of the excitation pulse that deteriorate image quality at higher STED powers.¹⁸ The fluorescence signal is directed to the detection path containing stacked emission filters (FF01-629/56-25, Semrock, Rochester, New York) and a multimode fiber (Thorlabs) coupled to a hybrid PMT (HPM-100-40, Becker and Hickl, Berlin, Germany). The PMT is linked to a single-photon counting card (SPC-830, Becker and Hickl) that allows for both intensity and lifetime measurements.

Sample preparation.

The instrument's spatial resolution was measured using monodispersed fluorescent beads, prepared by attaching carboxylate modified fluorescent beads (FluoSpheres® red, 40 nm, Invitrogen, Grand Island, New York) to a lysine coated glass coverslip (474030-9000-000, Carl Zeiss Microscopy, Thornwood, New York).¹⁹ These samples were embedded (VECTASHIELD® Hardest Mounting Medium, Burlingame, California), covered with a coverslip, and left to dry for 30 minutes before imaging.

Details of the cultured *Drosophila* S2 cells used in this study and their propagation have been previously described.²⁰ A 50- μ L solution of cells (1.5×10^6 cells/mL) was allowed to spread on a glass substrate for one hour, followed by removing unspread cells with phosphate buffered saline (PBS) rinses. The cells were fixed with 4% paraformaldehyde for ten minutes, and then rinsed with PBS. Cells were permeabilized with a 0.1% Triton® X-100 solution in PBS for two minutes and rinsed with PBS followed by a 1% bovine serum albumin solution in PBS to

prevent nonspecific binding of the Alexa Fluor 594-phalloidin to the glass. A 50- $\mu\text{g}/\text{mL}$ solution of Alexa Fluor 594-phalloidin was used to stain the cells for 6 hours. After rinsing with PBS, the cells were embedded as described above.

Imaging.

Images were generated by raster scanning the sample over the beams using a piezo stage (Nano-PDQ375, Mad City Labs, Madison, Wisconsin) that has sub-nanometer accuracy. Data were collected using the Single Photon Counter v9.30 software (Becker and Hickl) and further analyzed using SPCImage (Becker and Hickl). All of the TCSPC measurements were made in a ~ 8 ns time window with a total of 64 channels, and a 5-ms collection time per pixel to obtain sufficient counts for determining and resolving the lifetime data. The pixel size was 19.5 nm over a 256 x 256 or 512 x 512 pixel scan area, unless otherwise noted. Because stimulated emission is not complete at early times, the initial 0.5 ns of the fluorescence decay traces were discarded prior to fitting them with a single exponential. All measurements were performed at room temperature. Cross-sections showing fluorescence intensity of a line of adjacent pixels were generated using Image-J 1.44p (National Institutes of Health, USA), and all subsequent data processing was performed using Origin (OriginLab, Northampton, MA).

Results and Discussion

Instrumental spatial resolution: fluorescent beads.

The system's spatial resolution was measured by scanning 40-nm fluorescent beads immobilized on a coverslip with confocal (excitation beam with STED beam blocked) or STED (excitation and STED beams) illumination. Figure 3 presents confocal (A) and STED (B) images of the fluorescent beads. Cross sections of fluorescence intensity (Figure 3C) taken from the region shown with white arrows in the images indicate there is an improvement in the spatial

resolution measured by STED. Two fluorescent beads are merged into one feature in the confocal image, but are resolved in the STED cross section. The STED cross sections were fit to a Lorentzian, for which there is precedent in the literature.^{15,21} The FWHM were 49 and 39 nm for the left and right bead, respectively.

Table 1 shows the FWHM obtained by fitting the X- and Y- fluorescence intensity cross-sections of 15 beads with confocal or STED illumination. For the confocal images, the average FWHM are 450 ± 50 nm and 430 ± 30 nm. These values are larger than expected for the diffraction limit (~ 280 nm) for this system for two reasons: the objective is slightly under filled; and there is an index of refraction mismatch at the sample interface arising from embedding medium. Under filling the objective was required to minimize excitation artifacts that are otherwise prominent in the STED images. The embedding medium enables the use of the microscope's auto-focus function, which ensures that the focus is maintained over long scan-times. Unlike the STED cross sections, which seem to be well represented by Lorentzians, the confocal intensity distributions are better described by Gaussians.

The average FWHM of the STED cross sections for 15 beads are 36 ± 9 nm for the X-coordinate and 40 ± 10 nm for the Y-coordinate (Table 1). The small difference in the X and Y spatial resolution is due to subtle differences in the STED profile (Figure 2). The above resolution is achieved by time-gating the signal. A 0.5-ns gate provided the best spatial resolution. Without time-gating, the average FWHM of the beads was 80 nm. (Using a gate longer than 0.5 ns resulted in an apparent worsening of the spatial resolution, most likely owing to a reduction of the signal-to-noise ratio accompanying the detection of a reduced amount of fluorescence.) Time-gating also reduced the background and improved the uncertainty of the

measurement, as obtained from the full-width at half-maximum of the cross section of the beads. The uncertainty decreased from 44% without gating the signal to 26% with gating.

SC STED fluorescence lifetime imaging.

Fluorescence lifetime images acquired from confocal and STED illumination, and their representative decay curves, are given for the 40-nm fluorescent bead sample in Figure 4. The main challenge to obtaining fluorescence lifetimes using STED is a ~200-fold drop in the probed volume compared to confocal imaging. There would be ~200 molecules in the confocal probe volume assuming a homogenous 1- μ M solution compared to 1 molecule in the STED probe volume. Hell and coworkers previously reported an increase in the collection time per pixel from 1 ms (for intensity images) to 3 ms for TCSPC detection.¹⁴ The longer collection time is required to acquire sufficient counts in the fluorescence decay traces, and to obtain a reliable fit. Theoretically ~185 photons in the peak channel are necessary to resolve an exponential decay of single molecules in solution.²² On the other hand, Xie and coworkers resolved two exponentials in single molecule fluorescence decay traces with 64 counts in the peak channel.²³ It is noteworthy that the collection time cannot be increased significantly, because longer exposure of the fluorophores causes photobleaching. A similar issue is encountered when attempting finer movement of the sample stage. We thus scan a region once with only the excitation beam and then a second time with both the excitation and STED beams. Considering the trade-off between collection time and photobleaching rate, we chose to use a 5-ms collection time per pixel, which not only provided 50-100 counts in the peak channel to resolve exponential decays, but also prevented the fluorophores from extensively photobleaching. The confocal (A) and STED (B) lifetime images reveal a homogenous lifetime distribution, which is expected given the similar size of the fluorescent beads and the spatial resolution obtained with STED

illumination. The fluorescence lifetime of the beads (2.0 ± 0.1 ns) obtained from confocal and STED illumination is identical within the uncertainty of the measurement, as shown in Figure 4C. This indicates that the STED beam does not perturb the lifetime measurement, even with time gating.

Sub-diffraction fluorescence lifetime imaging of cultured cells.

STED fluorescence lifetime imaging was applied to F-actin in cultured cells. The protein, actin, is in monomeric (G actin) and filamentous (F actin) forms within the cell; and proper function of the actin cytoskeleton is important for most basic cellular functions. F-actin can be found in cellular structures that are smaller than the diffraction limit of light,²⁴ and traditional far-field imaging techniques provide few details of these structures. The small molecule, phalloidin, binds with high specificity to F-actin.²⁵ With a Alexa Fluor 594 fluorophore conjugated to phalloidin it is possible to visualize the distribution of F-actin in the cell. STED microscopy (intensity images) has been previously applied to measure actin fibers in cultured cells with 100-nm resolution.²⁶ A confocal intensity image of a whole cultured cell labeled with Alexa Fluor 594-phalloidin is shown in Figure 5A. Several F-actin structures are visible in the cell, including actin-rich projections around the periphery of the cell. An expanded view of two projections is shown with confocal (Figure 5B) and STED (Figure 5C) illumination. The images and the corresponding cross-sections (Figure 5D) of the narrowest point in one projection has the expected improvement in the STED spatial resolution. The FWHM of the confocal cross section is 290 nm and the same location measures 38 nm by STED.

Differences in the local actin environment could be measured as a distribution of the lifetimes for the fluorophore conjugated to F-actin bound phalloidin. A confocal fluorescence lifetime image of the entire cell (Figure 6A) was obtained in order to choose a specific region of

interest for which to compare confocal lifetime images (Figure 6B) with STED lifetime images (Figure 6C). As with the intensity-based comparison presented in Figure 5, the STED fluorescence lifetime image of the region of interest reveals F-actin structural details that are blurred due to the diffraction limit in the confocal lifetime image. The fluorescence decay curves obtained from two locations from the STED image, indicated with white arrows, are presented in (Figure 6D). These decay curves correspond to lifetimes of ~ 2.9 and ~ 2.2 ns. It is well known that fluorescein-type dyes (e.g., ATTO, Alexa Fluor) are strongly quenched by tryptophan due to photoinduced electron transfer from tryptophan (which acts as a donor) to the fluorescein moiety (which acts as acceptor).^{27,28} We note, however, that in a cell, because of its inherent complexity, tryptophan may be one of the quenchers of Alexa Fluor 594; but it is not necessarily the only one.

For purposes of comparison, the fluorescence decay profile obtained from the Alexa Fluor 594-phalloidin conjugate in the same medium used to prepare the cells is presented in Figure 6D. This profile was obtained with the same instrumentation used to obtain the STED lifetimes and an excitation wavelength of 570 nm. It can be superposed over the 2.9-ns STED profile; and this suggests that the 2.9-ns lifetime arises from unquenched fluorescent marker and that the difference in the STED lifetimes from one site to another in the cells may be attributed to the differential quenching of the Alexa Fluor 594 fluorescence by neighboring tryptophan residues and possibly other unknown species. The histogram (Figure 6E) of fluorescence lifetimes measured for every pixel in the STED image is well fit to a Gaussian.

As noted above, the decay curves obtained from the STED measurement that are presented in Figure 6D correspond to lifetimes of ~ 2.9 and ~ 2.2 ns, which we attribute to specific quenching interactions between Alexa Fluor and components of the cell. Because the data from Figure 6 represent only one measurement of one cell, means and associated errors could not be directly obtained for the

lifetimes we cite. In order to obtain an estimate, we measured a solution of ATTO 590 in ethanol using the STED instrument. The data collected from 4096 pixels yielded a lifetime of 3.56 ± 0.06 ns, i.e., an error of about 2%. It is a reasonable assumption that the percent error for the STED-obtained Alexa Fluor 594-phalloidin lifetimes is similar. Even assuming an uncertainty of 10% for each lifetime, ~ 2.9 and ~ 2.2 ns lifetimes would be distinguishable from each other. Finally, in the interest of completeness, we present an alternate interpretation for the origin of the different lifetimes. The observation of a distribution of Alexa Fluor lifetimes that is very well described by a Gaussian (Figure 6E) could suggest that the spread in lifetimes merely reflects statistical error in measuring the fluorescent probe in different parts of the cell.

Conclusions

Fluorescence lifetime images with ~ 40 -nm lateral spatial resolution have been reported. Fluorescence lifetimes were statistically similar in confocal and STED measurements for both fluorescent beads and Alexa Fluor 594-phalloidin in cultured cells, and suggest a level of Alexa Fluor 594 quenching in cultured cells. These results open the door to measurements of lifetimes in heterogeneous domains smaller than the diffraction limit.

Acknowledgements

This research is supported by the U.S. Department of Energy, Office of Basic Energy Sciences, Division of Chemical Sciences, Geosciences, and Biosciences through the Ames Laboratory. The Ames Laboratory is operated for the U.S. Department of Energy by Iowa State University under Contract No. DE-AC02-07CH11358. The SC STED fluorescence lifetime microscope was built using funds from the National Science Foundation Chemical Research Instrumentation and Facilities program (CHE-0845236). We thank Mr. Ujjal Bhattacharjee, Dr. Suzanne Sander and Dr. Kristopher J. McKee for technical assistance.

References

- (1) Abbe, E. Archiv für Mikroskopische Anatomie 1873, 9, 413.
- (2) Rust, M. J.; Bates, M.; Zhuang, X. Nat Meth 2006, 3, 793.
- (3) Binnig, G.; Quate, C. F.; Gerber, C. Physical Review Letters 1986, 56, 930.
- (4) Hell, S. W.; Wichmann, J. Opt. Lett. 1994, 19, 780.
- (5) Donnert, G.; Keller, J.; Medda, R.; Andrei, M. A.; Rizzoli, S. O.; LÃ¼hrmann, R.; Jahn, R.; Eggeling, C.; Hell, S. W. Proceedings of the National Academy of Sciences 2006, 103, 11440.
- (6) Klar, T. A.; Engel, E.; Hell, S. W. Physical Review E 2001, 64, 066613.
- (7) Klar, T. A.; Hell, S. W. Opt. Lett. 1999, 24, 954.
- (8) Rittweger, E.; Han, K. Y.; Irvine, S. E.; Eggeling, C.; Hell, S. W. Nat Photon 2009, 3, 144.
- (9) Willig, K. I.; Harke, B.; Medda, R.; Hell, S. W. Nat Meth 2007, 4, 915.
- (10) Willig, K. I.; Keller, J.; Bossi, M.; Hell, S. W. New Journal of Physics 2006, 8, 106.
- (11) Wildanger, D.; Rittweger, E.; Kastrup, L.; Hell, S. W. Opt. Express 2008, 16, 9614.
- (12) Auksorius, E.; Boruah, B. R.; Dunsby, C.; Lanigan, P. M. P.; Kennedy, G.; Neil, M. A. A.; French, P. M. W. Opt. Lett. 2008, 33, 113.
- (13) Wildanger, D.; Medda, R.; Kastrup, L.; Hell, S. W. Journal of Microscopy 2009, 236, 35.
- (14) Bückers, J.; Wildanger, D.; Vicidomini, G.; Kastrup, L.; Hell, S. W. Opt. Express 2011, 19, 3130.
- (15) Vicidomini, G.; Moneron, G.; Han, K. Y.; Westphal, V.; Ta, H.; Reuss, M.; Engelhardt, J.; Eggeling, C.; Hell, S. W. Nat Meth 2011, 8, 571.
- (16) Schrader, M.; Hell, S. W. Journal of Microscopy 1996, 184, 143.
- (17) Dedecker, P.; Muls, B.; Hofkens, J.; Enderlein, J.; Hotta, J.-i. Opt. Express 2007, 15, 3372.
- (18) Leutenegger, M.; Eggeling, C.; Hell, S. W. Opt. Express 2010, 18, 26417.

- (19) Wurm, C. A.; Neumann, D.; Schmidt, R.; Egner, A.; Jakobs, S. Sample Preparation for STED Microscopy. In *Live Cell Imaging*, 2009; Vol. 591; pp 185.
- (20) Ditya, D.; Arora, N.; Smith, E. A. *Biophysical Journal* 2010, 99, 853.
- (21) Fitzpatrick, J. A. J.; Yan, Q.; Sieber, J. J.; Dyba, M.; Schwarz, U.; Szent-Gyorgyi, C.; Woolford, C. A.; Berget, P. B.; Waggoner, A. S.; Bruchez, M. P. *Bioconjugate Chemistry* 2009, 20, 1843.
- (22) Köllner, M.; Wolfrum, J. *Chem. Phys. Lett.* 1992, 200, 199.
- (23) Dunn, R.; Holtom, G.; Mets, L.; Xie, X. J. *Phys. Chem.* 1994, 98, 3094.
- (24) Fuchs, E.; Cleveland, D. W. *Science* 1998, 279, 514.
- (25) Lengsfeld, A. M.; Löw, I.; Wieland, T.; Dancker, P.; Hasselbach, W. *Proceedings of the National Academy of Sciences* 1974, 71, 2803.
- (26) Farahani, J.; Schibler, M.; Bentolila, L. Stimulated Emission Depletion (STED) Microscopy: from Theory to Practice. In *Microscopy: Science, Technology, Applications and Education*; Méndez-Vilas, A., Díaz, J., Eds.; Formatex Research Center: Badajoz, Spain, 2010; Vol. 2; pp 1539.
- (27) Chen, H.; Ahsan, S.; Santiago-Berrios, M.; Abruña, H.; Webb, W. J. *Amer. Chem. Soc.* 2010, 132, 7244.
- (28) Marmé, N.; Knemeyer, J.-P.; Sauer, M.; Wolfrum, J. *Bioconjugate Chem.* 2003, 14, 1133.

Table 1. Full width half maximum (FWHM) values obtained from X- and Y-cross sections of fluorescent beads obtained in the image shown in Figure 3, or similar images.

Fluorescent Beads	Confocal		STED	
	X	Y	X	Y
	FWHM (nm)	FWHM (nm)	FWHM (nm)	FWHM (nm)
1	504	451	39	33
2	484	448	41	55
3	454	468	52	39
4	561	412	33	22
5	462	415	33	35
6	408	411	54	45
7	435	400	34	46
8	450	452	43	20
9	398	457	33	27
10	451	400	27	44
11	441	429	37	78
12	355	376	41	52
13	514	486	26	41
14	382	410	31	42
15	480	427	23	57
AVERAGE	450 ± 50	430 ± 30	36 ± 9	40 ± 10

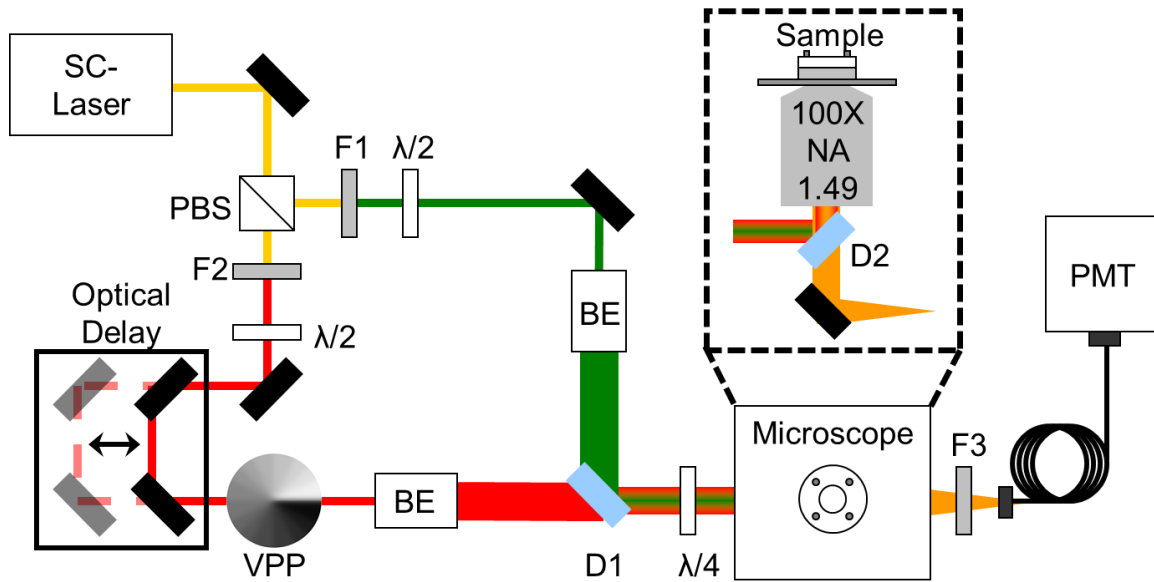


Figure 1. Schematic of the SC STED fluorescence lifetime microscope showing the SC being split into two paths by a polarizing beam splitter (PBS). The desired wavelengths are extracted by interference filters (F), F1 and F2- which isolate the excitation and STED wavelengths, respectively. Both paths have half-wave plates ($\lambda/2$) for adjusting the polarization. The STED path has an optical delay line to adjust the arrival of the pulses at the sample and the toroid shape is imparted using a vortex-phase plate (VPP). Both beams are expanded and collimated using beam expanders (BE) and recombined using a long-pass dichroic (D1). A quarter-wave plate ($\lambda/4$) generates circular polarization. The beams are reflected to the sample with a dichroic mirror (D2) that transmits the resulting fluorescence to the emission filters (F3). The fluorescence is then passed onto a multimode fiber (MMF) and detected by a photomultiplier tube (PMT). The portion of the schematic within the dashed lines presents a view perpendicular to the laser table.

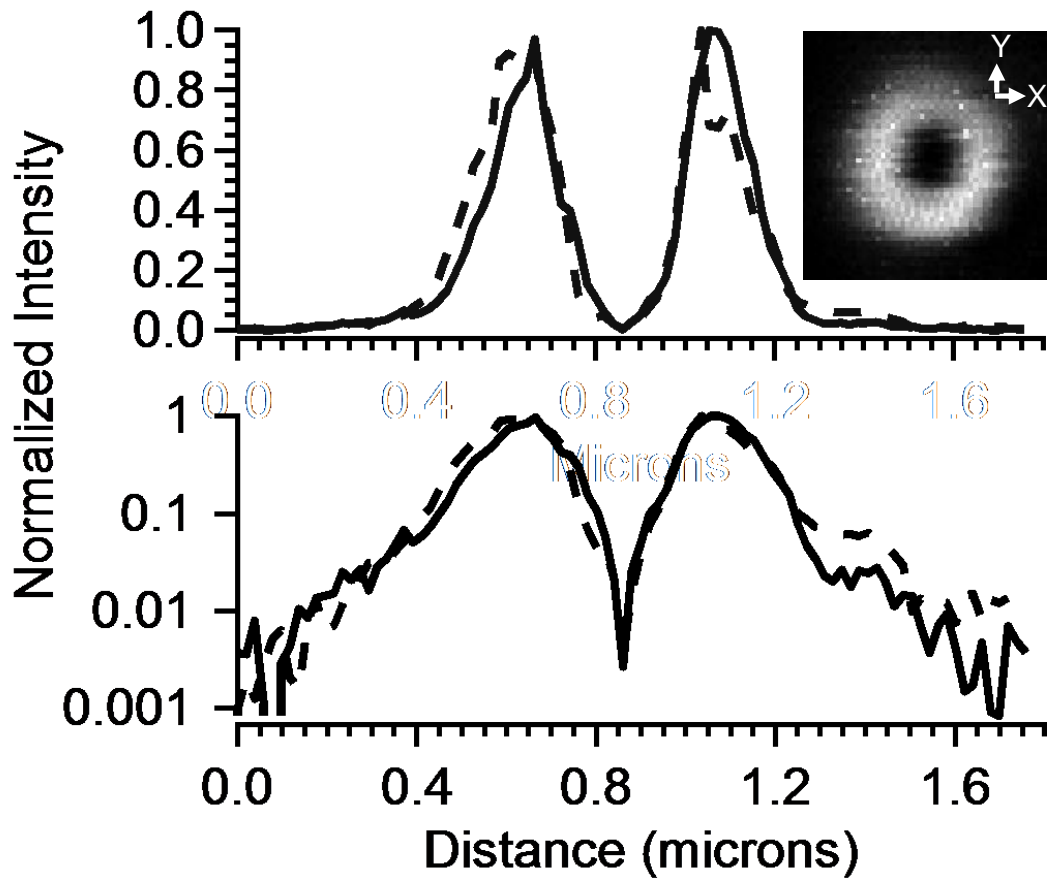


Figure 2. Orthogonal cross-sections of the toroidal STED beam profile (X-coordinate solid line, Y-coordinate dotted line) on a linear (top) and log scale (bottom). The log plot reveals an intensity drop in the center of the profile to $\sim 0.3\%$ of the maximum intensity. The inset image was obtained by measuring the scatter from 60-nm gold nanoparticles.

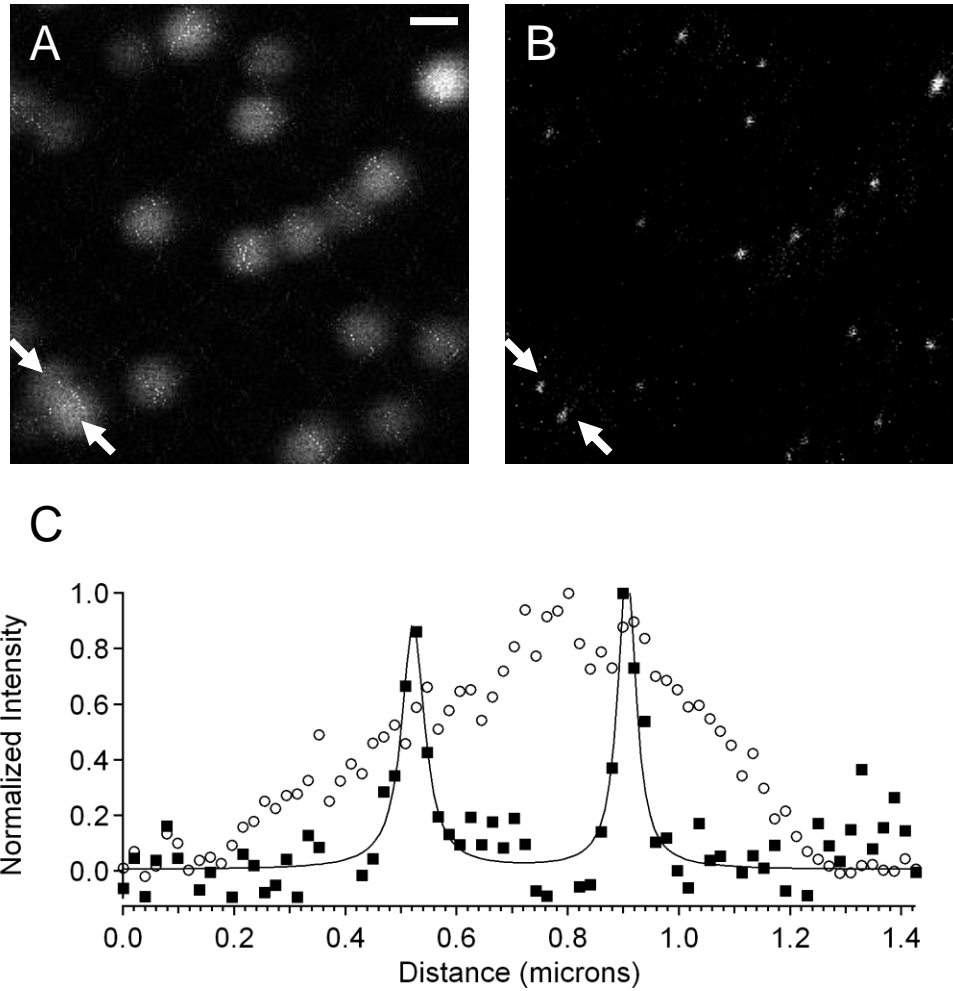


Figure 3. Confocal (A) and STED (B) fluorescence intensity images of 40-nm fluorescent beads. The white arrows highlight two beads that are unresolved in the confocal image but resolved with STED. (C) The STED cross section (solid squares) fit to a Lorentzian yields FWHMs of 49 and 39 nm. The confocal cross section (open circles) was not fit. The scale bar represents 500 nm and is the same for both images

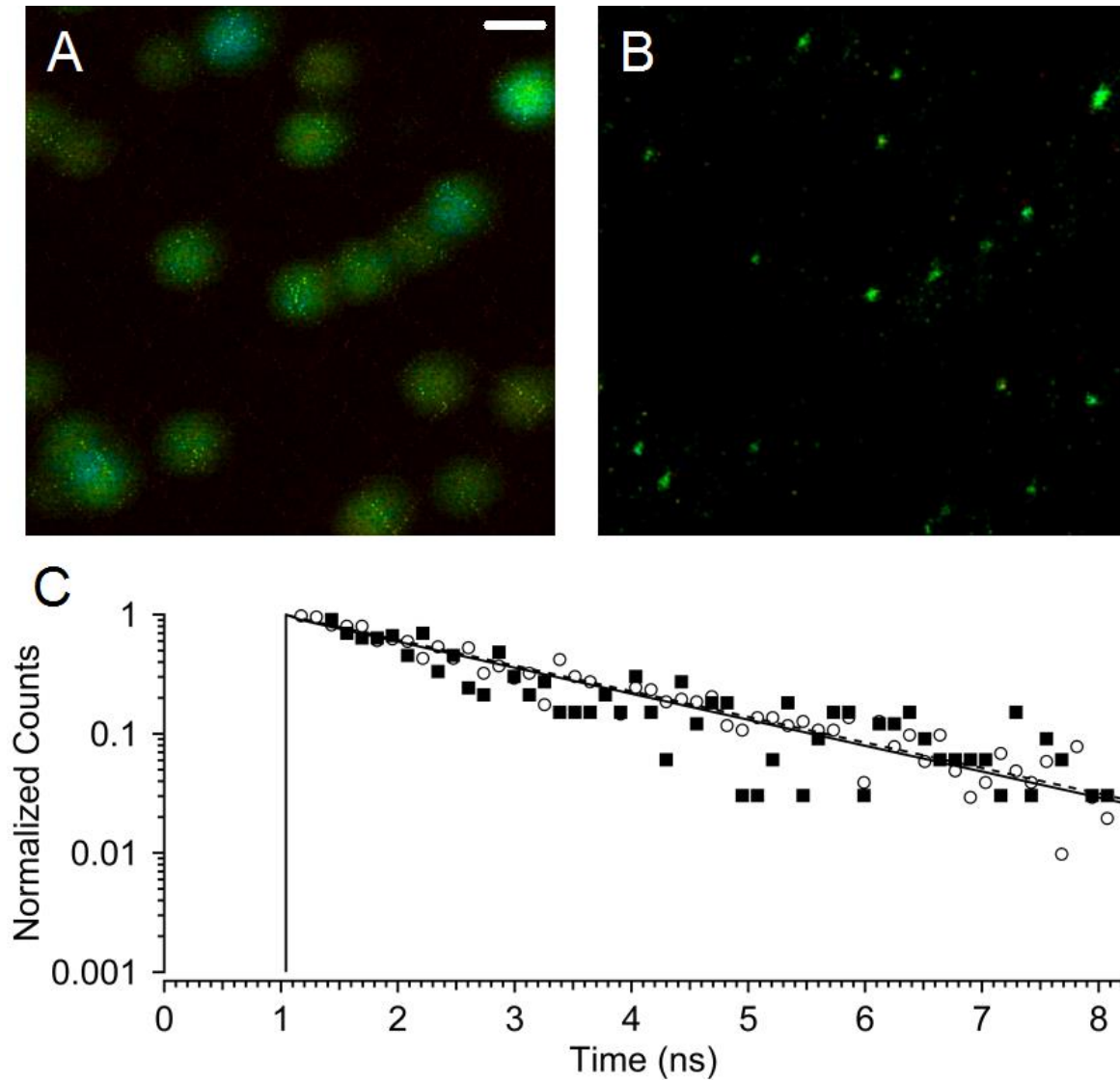


Figure 4. Confocal (A) and STED (B) fluorescence lifetime images of 40-nm fluorescent beads. Representative fluorescence decay curves (C) for the confocal (open circles, solid fit) and STED (solid squares, dashed fit) were fit to a single exponential with a 2.0 ± 0.1 ns fluorescence lifetime. The scale bar represents 500 nm and is the same for both images.

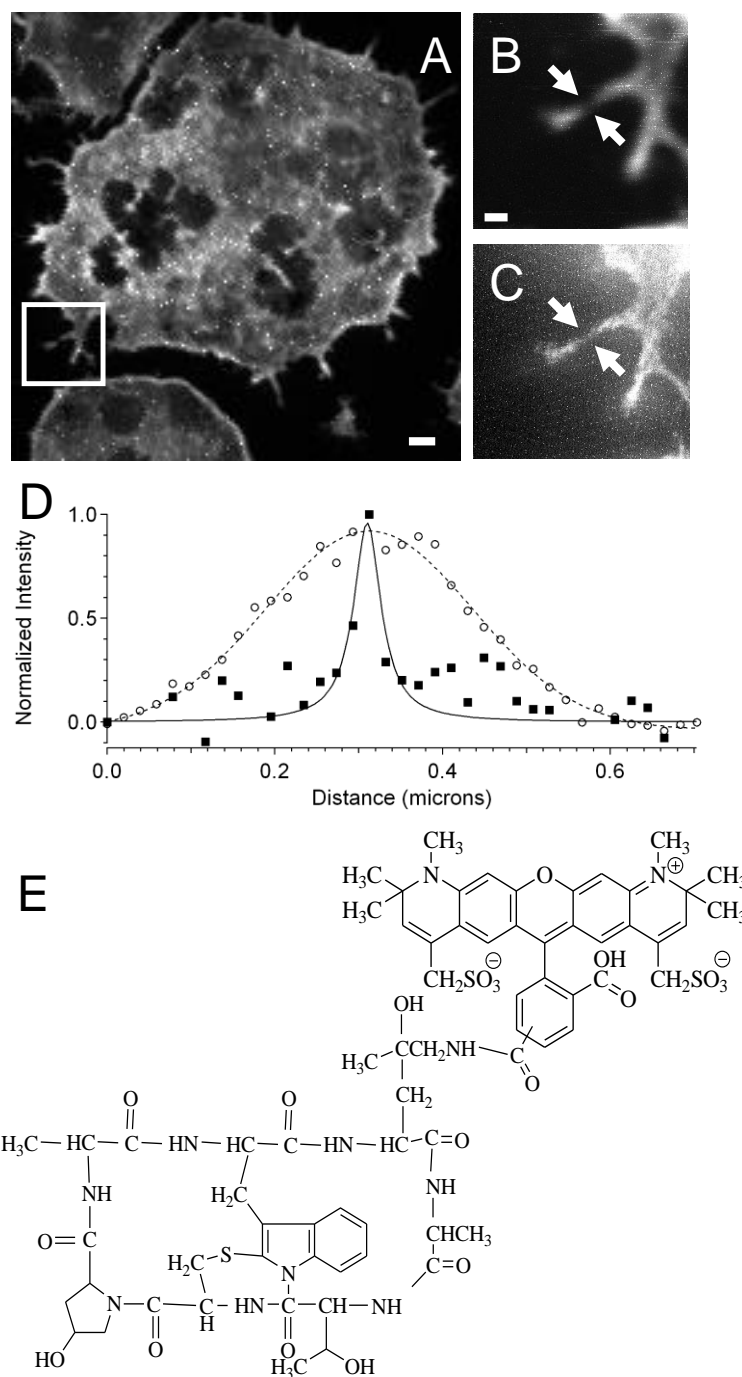


Figure 5. Fluorescence intensity images of a cell with Alexa Fluor 594-phalloidin labeled actin. (A) An overview confocal image with an ~ 195 -nm pixel size, scale bar of 2 microns. (B) Confocal and (C) STED images of a selected 5×5 micron region shown with a white box in (A). Scale bars for (B) and (C) represent 500 nm. The arrows in (B) and (C) represent the cross sections shown in (D) for the confocal (open circles) and STED (solid squares) images. The FWHMs from the Gaussian (confocal) and Lorentzian (STED) fits are 290 nm and 38 nm, respectively. (E) Structure of Alexa Fluor 594-phalloidin.

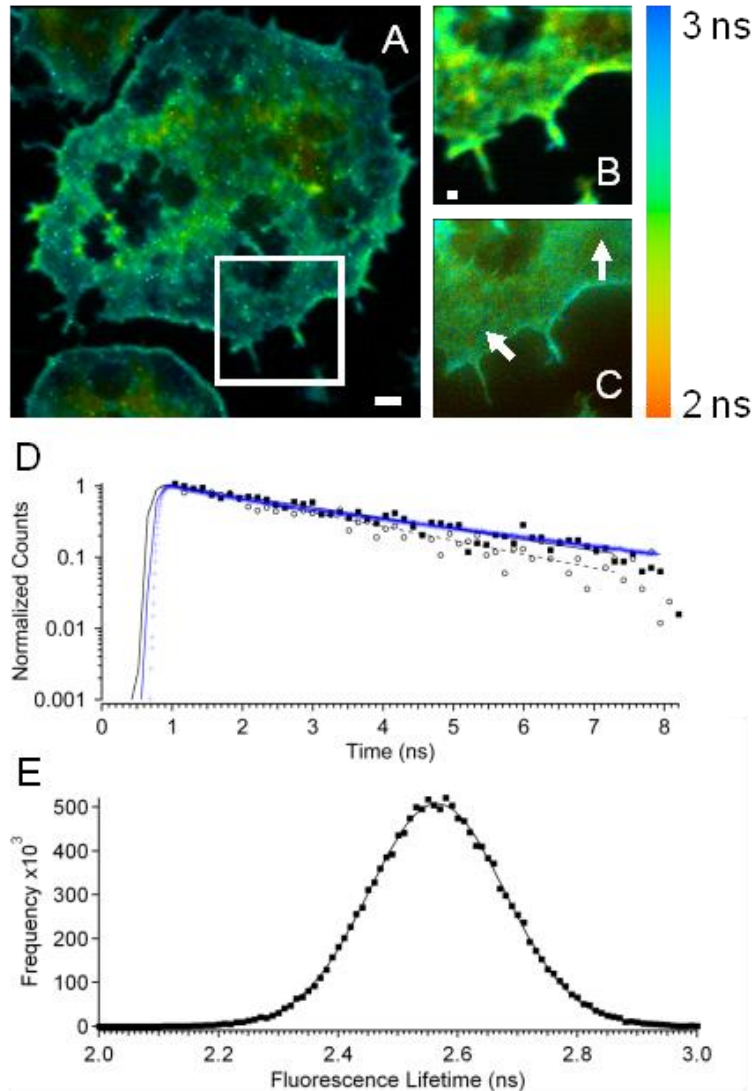


Figure 6. Fluorescence lifetime images of a cell with Alexa Fluor 594-phalloidin labeled actin. (A) An overview confocal image, ~ 195 -nm pixel size, scale bar of 2 microns. (B) Confocal and (C) STED images of a selected 10×10 micron region shown with a white box in (A). Scale bars for (B) and (C) represent 500 nm. (D) Representative fluorescence decay curves from two different regions (denoted by white arrows) from the image (C) fit to a single exponential with 2.9-ns (solid square) or 2.2-ns (open circle) fluorescence lifetimes. For purposes of comparison, the fluorescence decay profile (blue) obtained from the Alexa Fluor 594-phalloidin conjugate, in the same medium used to prepare the cells, is presented in panel (D). It is superposed over and is, within experimental error, identical to the 2.9-ns value obtained from the STED measurement. (E) A histogram of the STED fluorescence lifetime distribution from (C). The distribution of lifetimes obtained from the STED and confocal images are both well fit to Gaussians. The STED distribution has a mean of 2.6 ± 0.1 ns; the confocal distribution, a mean of 2.55 ± 0.08 ns.

CHAPTER 3 : SUBDIFFRACTION LUMINESCENCE-DEPLETION OF ISOLATED, GIANT, CdSe/CdS NANOCRYSTAL QUANTUM DOTS

Reproduced with permission from [Lesoine, M. D.; Bhattacharjee, U.; Guo, Y.; Vela, J.; Petrich, J. W.; Smith, E. A., Subdiffraction, Luminescence-Depletion Imaging of Isolated, Giant, CdSe/CdS Nanocrystal Quantum Dots. The Journal of Physical Chemistry C 2013, 117 (7), 3662-3667.] Copyright [2014] American Chemical Society.

Michael D. Lesoine, Ujjal Bhattacharjee, Yijun Guo, Javier Vela, Jacob W. Petrich, and Emily A. Smith

Abstract

Subdiffraction spatial resolution luminescence depletion imaging was performed with giant CdSe/CdS nanocrystal quantum dots (g-NQDs) dispersed on a glass slide. Luminescence depletion imaging used a Gaussian shaped excitation laser pulse overlapped with a depletion pulse, shaped into a doughnut profile, with zero intensity in the center. Luminescence from a subdiffraction volume is collected from the central portion of the excitation spot, where no depletion takes place. Up to 92% depletion of the luminescence signal was achieved. An average full-width at half-maximum of 40 ± 10 nm was measured in the lateral direction for isolated g-NQDs at an air interface using luminescence depletion imaging; whereas the average full-width at half-maximum was 450 ± 90 nm using diffraction-limited, confocal luminescence imaging. Time-gating of the luminescence depletion data was required to achieve the stated spatial resolution. No observable photobleaching of the g-NQDs was present in the measurements, which allowed imaging with a dwell time of 250 ms per pixel to obtain images

with a high signal-to-noise ratio. The mechanism for luminescence depletion is likely stimulated emission, stimulated absorption, or a combination of the two. The g-NQDs fulfill a need for versatile, photostable tags for subdiffraction imaging schemes where high laser powers or long exposure times are used.

Introduction

Lateral spatial resolution using visible wavelengths is limited by diffraction to ~ 250 nm in far-field optical microscopy.¹ There are several imaging techniques available to circumvent this constraint. Near-field techniques with a probe in close proximity to the sample can be used, but the probe can be too invasive for some applications.² In addition to using a near-field technique, there are several far-field techniques that have been developed. Stochastic optical reconstruction microscopy and several similar techniques utilize intermittent on/off states to limit the number of fluorophores emitting in a diffraction limited volume, and to generate a series of images that are reconstructed into a high resolution image.³ Stimulated emission depletion (STED) microscopy uses point-spread function engineering, and can yield measurements with high spatial and temporal resolution.⁴⁻¹² STED uses a doughnut shaped depletion beam that spatially and temporally overlaps a Gaussian shaped excitation beam. The depletion beam is tuned to the red edge of a fluorophore's emission spectrum providing depletion of the signal at the periphery of the Gaussian excitation profile. The resulting signal from the center of the excitation profile is below the diffraction limit.

In order to achieve subdiffraction spatial resolution imaging with STED, high laser powers or long acquisition times may be required. These conditions may lead to significant photobleaching of most small molecule fluorophores, which can degrade the achieved spatial resolution.¹³⁻¹⁴ Nanocrystal quantum dots (NQDs) display the highest photostability of the prominently used fluorescent labels,¹⁵⁻¹⁶ making them an ideal fluorophore for STED. On the

other hand, Auger recombination, for example, is known to prevent efficient stimulated emission of isolated NQDs.¹⁷ Stimulated emission can outpace Auger recombination in close-packed solids and highly concentrated colloidal solutions,¹⁸⁻¹⁹ but extended solids have limited utility as tags for imaging applications.

Hell and coworkers demonstrated 45-nm spatial resolution along a single axis for clusters of Mn-doped ZnSe QDs using a depletion beam with two nodes having zero intensity between them.²⁰ They attributed the improved spatial resolution to stimulated absorption to higher-lying excited states.²¹ Clusters of QDs were necessary for their study to avoid excessive exposure times as sufficient signal could not be obtained with isolated QDs due to a long lifetime (about 90 ns) of the luminescence transition.

So-called giant NQDs (g-NQD) with 10 to 20 monolayers of CdS shell added onto a 2- to 5-nm CdSe core exhibit suppression of luminescence intermittency (*i.e.*, blinking) and almost complete suppression of Auger recombination.²²⁻²⁵ The suppression of Auger recombination has the effect of increasing the lifetime of biexcitons and even allowing the observation of multiexciton states.²⁶ Radiative lifetime components of excitons, biexcitons, and up to 6th-order multiexcitons in g-NQDs were observed with excitation powers on the order of 1 kW cm⁻² at 4 K.²⁶ Furthermore, biexcitons and multiexcitons can undergo more effective stimulated emission, with the multiexcitons having a lower threshold for stimulated emission than biexcitons and indeed many dye molecules.²³

Here, we report luminescence depletion (LD) imaging using CdSe/14CdS g-NQDs with a lateral spatial resolution of 40 ± 10 nm. It is proposed that stimulated emission and excited-state absorption mechanisms may work either independently or synergistically to provide depletion. A

7-fold improvement over the diffraction barrier was generated at an air interface with excitation and depletion powers of 50 pJ and 2 nJ, respectively.

Experimental

Sample preparation and characterization

The g-NQDs have been previously described.²⁷ A dilute solution of CdSe/14CdS g-NQDs (average particle size 13 ± 2 nm as measured by transmission electron microscopy) in toluene was deposited on a glass slide (474030-9000-000, Carl Zeiss Microscopy, Thornwood, NY) and the solvent allowed to evaporate. The sample was dried in ambient conditions for 30 min before any measurements were performed.

Blinking statistics for the g-NQDs were determined by comparing the percent of time the signal was in a binary high (on) or low (off) state using sequential 25-ms measurements over a 95-s time window. Depletion efficiencies for the g-NQDs were measured as the attenuation of the luminescence signal after illumination with the excitation and depletion wavelengths compared to the signal with illumination of only the excitation wavelength. The depletion power was varied and sequential 250-ms measurements over a 45-s time window were collected. Depletion was also observed with a CMOS camera (Moticam 2, Motic, British Columbia, Canada) by illuminating a single QD with the excitation beam and blocking and unblocking the LD beam. Photobleaching rates for the g-NQDs were measured by illuminating the samples with the excitation beam at the same position and taking sequential time measurements over 3.5 minutes. For all measurements described above, the beams had a Gaussian profile.

Imaging

The imaging system used for these studies has been described previously.²⁸ Minor changes to the system are described below. The excitation and depletion beams derive from a SC laser, (SC-450-pp-he, Fianium, Southampton, UK), which has its output split into two paths using a polarizing beam splitter cube (DMLP605R, Thorlabs, Newton, New Jersey). The laser used a repetition rate of 2 MHz with instrument response function pulse widths for the excitation and LD pulses of approximately 120 and 160 ps, respectively, the two pulses were offset with the LD pulse trailing the excitation pulse by ~100 ps. Filters are used to select the excitation and LD wavelengths, which are shown in Figure 1. Measurements were performed using 50 pJ for excitation and 2 nJ for LD, as measured before the microscope objective. The excitation and LD pulses were 0.7 and 1.2 cm behind the objective, respectively. (~350 and 600 nm at the sample plane; excitation LD.) The LD beam was shaped into a doughnut with a vortex-phase plate. The beams are expanded and collimated before being recombined using a dichroic mirror (ZT594RDC, Chroma, Bellows Falls, Vermont). The collinear pulses are reflected via a dichroic mirror (635-70BPDC, Chroma) to an oil immersion objective and the resulting luminescence is directed to the detection path. The signal is sent to two stacked emission filters (FF01-629/56-25, Semrock, Rochester, New York) and subsequently through a 100 micron pinhole (NT36-392, Edmund Optics, Barrington, NJ) and a hybrid photomultiplier tube (HPM-100-40, Becker and Hickl, Berlin, Germany) coupled to a single-photon counting card (SPC-830, Becker and Hickl).

Raster scanning of a 1×1 micron (64×64 pixels) or 2×2 micron (128×128 pixels) region was used to generate the images. Images were collected at room temperature. All data were collected with Single Photon Counter v9.30 software (Becker & Hickl) and analyzed further using SPCImage (Becker & Hickl) or MATLAB version 2011b (Mathworks, Natick,

MA). A time window of 3.3 ns with 64 time channels and a dwell time of 250-ms per pixel were used. Time-gating was used to obtain the best spatial resolution, as further outlined below. Image-J 1.44p (National Institutes of Health, USA) was used to take cross-sections of contiguous pixels in the collected images and Origin (OriginLab, Northampton, MA) was used to perform all other data processing. All reported uncertainties are one standard deviation.

Results and Discussion

Luminescence depletion efficiencies of g-NQDs

The goal of this work was to explore the ability of giant nanocrystal quantum dots (g-NQDs) to serve as photostable tags for subdiffraction imaging techniques that require high laser powers and/or long exposure times. In practice, this required determining the experimental conditions, including wavelengths, laser powers, acquisition times, and signal gating, necessary for subdiffraction imaging using g-NQDs. As observed in Figure 1, the g-NQDs display the characteristic broad excitation curve (blue curve). The excitation wavelengths (green curve) were chosen to be as far red-shifted as possible in order to limit scattering, photodamage, and background luminescence in future applications where this may be an issue, such as in the case of biological samples, without compromising the desired signal collection. The amount of spectral overlap between the g-NQD's narrow emission profile (yellow curve) and the depletion wavelengths (red curve) had to be carefully balanced. A too small overlap would lead to inefficient depletion, while an unnecessarily large overlap would cause an unwanted decrease in signal collection from a narrow detection window (black curve). LD occurs with the chosen excitation and depletion wavelengths (Figure 1 inset). In this instance, both the excitation and depletion beams were Gaussian shaped, and the data reveal that the depletion is reversible.

The optimum power of the depletion beam results in 100% LD efficiency without excessive exposure of the sample to high photon fluxes, thus limiting sample heating and damage. In order to determine the optimal power for the depletion beam, the attenuation of the luminescence signal for isolated g-NQDs was recorded for varying depletion powers (Figure 2). The depletion efficiency increases with increasing depletion power up to the maximum output of the laser used for these studies (2.0 nJ). At the highest power, a 92% depletion was obtained after correcting for a 3% contribution to the luminescence signal caused by the depletion beam. The mechanism of the high depletion efficiency could be stimulated emission, stimulated absorption, or both. Stimulated absorption has been shown for Mn-Doped ZnSe NQDs.²⁰ A definitive assignment of the mechanism will, however, require further experiments that are beyond the scope of this work.

Determination of G-NQDs on/off Time and photobleaching rates

A zero or low frequency of blinking events is desirable for raster scan imaging to maintain the generated image's integrity. For an imaging application, a dwell time that is too short relative to the blinking characteristics of the nanoparticle will result in an undesired false negative at that pixel, on the other hand, it is not desirable to ensure there are no false negatives, as excessive imaging times may result. The blinking characteristics of the g-NQDs must be known to set a dwell time per pixel that limits false negatives and to quantify the probability of recording a false negative at an acceptable imaging speed. Therefore, the luminescence signal of isolated g-NQDs was recorded over a time window of 95 s using an excitation power of 50 pJ. Representative data from ten randomly chosen g-NQDs are shown in Figure 3. The average percent on-time for all nanoparticles was $98.40 \pm 0.04\%$. Hollingsworth and coworkers reported an on-time of greater than 99% and between 99 to 80% of the total analysis time as

corresponding to non-blinking and largely-non-blinking g-NQDs, respectively.²⁴ The percentage of particles with on-times greater than 99% was 90% and the average off-time for these particles was 100 ± 200 ms. While the percentage of particles with on-times between 99 to 80% was 10%.

No observable photobleaching was observed on the time-scale of any of the measurements performed, which included an extended 3.5-minute illumination of the g-NQDs. This allowed for dwell times per pixel not possible with typical fluorescent dyes used for STED, including the 250 ms dwell time used for subsequent experiments.

Subdiffraction spatial resolution using g-NQDs

The confocal and LD images of 12 quantum dots are shown in Figure 4. The confocal images were recorded using only the excitation beam, while both the excitation and depletion beams were incident upon the sample for the LD images. The improvement in the spatial resolution of the LD images is evident by the smaller feature size. In the confocal images, there are occasional rows of lower luminescence intensity compared to the rest of the pixels representing the g-NQD. This is attributed to a few intermittent blinking periods, characteristic of even the best g-NQDs. The amount of intermittent blinking recorded in the LD images is significantly lower than in the confocal images, and is only observed for g-NQD number 6. This is expected since the total time used to collect the nanoparticle's luminescence signal (not the time the nanoparticle is exposed to the laser) in the LD mode is 97.7 ± 0.8 % shorter than that used to collect the confocal image.

Cross-sections were measured for each g-NQD shown in Figure 4, and representative cross-sections are shown in Figure 5. The confocal cross-sections were best fit to Gaussians, while the LD cross-sections were best fit to Lorentzians. This is consistent with previously

reported STED data using small fluorophores.^{8,28-29} The representative cross-sections in Figure 5 show a resolution enhancement, as defined by the full-width at half-maximum (fwhm), from 398 nm for the confocal mode to 43 nm for the LD mode. The average fwhm values for 12 g-NQDs are given in Table 1. The average cross section is 450 ± 90 nm and 40 ± 10 nm for the confocal and LD modes, respectively. For comparison, the actual “physical” average particle size measured by transmission electron microscopy was 13 ± 2 nm.

In order to achieve the 40 ± 10 nm spatial resolution in the LD imaging mode, we had to time-gate the data. The average fwhm of the LD cross-sections prior to applying the time-gate was 90 ± 20 nm. A representative confocal and LD decay curve is shown in Figure 6. The applied time-gate is represented by the two vertical lines. The signal prior to 600 ps is higher in the LD curve than the confocal curve. This is likely the result of scatter due to the STED beam, which degrades the spatial resolution. A time-gate at 500 ps was previously applied to STED images using small molecule fluorophores because depletion was incomplete at earlier times.²⁸ At long times the decay curve is primarily dominated by noise that does not convey useful information. While gating the signal significantly improved the LD image, gating the confocal data did not significantly alter the average fwhm of the confocal data set (Figure 6 bottom).

Two lifetime components were extracted from the LD data (2400 ± 800 ps and 300 ± 100 ps). One or both of the lifetime components may originate from multiexcitons. Htoon et al.²⁶ measured higher-order excitons in similar g-NQD at 4K using a $21\times$ lower power density than used in the current study (21 kW cm^{-2} for the excitation beam). The percentage of the short component decreased from $70 \pm 6\%$ to $50 \pm 10\%$ for the confocal to LD imaging formats, respectively (Figure 6).

The overall quality of the confocal and luminescence decay curves are similar (Figure 6). In a previous experiment using small dye molecules, the noise in the STED decay curve was higher compared to that obtained in the confocal experiment.²⁸ This was because far fewer molecules were probed by STED, and this reduced the signal. For the small molecule fluorophores, the dwell time per pixel was limited to 5 ms due to excessive photobleaching at longer dwell times. The photostability of the g-NQDs allows the dwell time per pixel to be increased, increasing the signal and improving the quality of the decay curve. A 250 ms dwell time was used for these studies, but shorter dwell times could be used to increase the imaging speed, particularly if data are recorded with fewer time channels (i.e., if time-gating is applied but lifetimes are not extracted), while still generating high-quality images with good signal-to-noise ratios.

Conclusions

Luminescence depletion images of CdSe/14CdS giant nanocrystal quantum dots (g-NQDs) with 13 ± 2 nm particle size show a spatial resolution of 40 ± 10 nm. The mode of the resolution enhancement is through depletion of the g-NQDs luminescence, suggested to be the result of stimulated emission and absorption working individually or in concert. Time-correlated, single-photon counting detection allowed the signal to be time-gated, which is required for achieving 40-nm spatial resolution images. Critical for obtaining this result, is that photobleaching was not observed, permitting high quality measurements with extended dwell times that would be difficult to obtain under conditions where photobleaching was present. We conclude that g-NQDs show great promise as robust fluorescent labels for subdiffraction measurements in densely populated systems.

Acknowledgements

This research is supported by the U.S. Department of Energy, Office of Basic Energy Sciences, Division of Chemical Sciences, Geosciences, and Biosciences through the Ames Laboratory. The Ames Laboratory is operated for the U.S. Department of Energy by Iowa State University under Contract No. DE-AC02-07CH11358. *The STED microscope was built using funds from the National Science Foundation Chemical Research Instrumentation and Facilities program (CHE-1026028).* J. V. thanks Iowa State University and Plant Sciences Institute for seed funds.

References

- (1) Abbe, E. Archiv für Mikroskopische Anatomie 1873, 9, 413.
- (2) Binnig, G.; Quate, C. F.; Gerber, C. Phys. Rev. Lett. 1986, 56, 930.
- (3) Rust, M. J.; Bates, M.; Zhuang, X. Nat. Methods 2006, 3, 793.
- (4) Hell, S. W.; Wichmann, J. Opt. Lett. 1994, 19, 780.
- (5) Klar, T. A.; Hell, S. W. Opt. Lett. 1999, 24, 954.
- (6) Klar, T. A.; Engel, E.; Hell, S. W. Phys. Rev. E 2001, 64, 066613.
- (7) Bain, A. J.; Marsh, R. J.; Armoogum, D. A.; Mongin, O.; Porrès, L.; Blanchard-Desce, M. Biochem. Soc. Trans. 2003, 31, 1047.
- (8) Vicidomini, G.; Moneron, G.; Han, K. Y.; Westphal, V.; Ta, H.; Reuss, M.; Engelhardt, J.; Eggeling, C.; Hell, S. W. Nat. Methods 2011, 8, 571.
- (9) Donnert, G.; Keller, J.; Medda, R.; Andrei, M. A.; Rizzoli, S. O.; Lührmann, R.; Jahn, R.; Eggeling, C.; Hell, S. W. Proc. Natl. Acad. Sci. U.S.A. 2006, 103, 11440.
- (10) Willig, K. I.; Keller, J.; Bossi, M.; Hell, S. W. New J. Phys. 2006, 8, 106.
- (11) Willig, K. I.; Kellner, R. R.; Medda, R.; Hein, B.; Jakobs, S.; Hell, S. W. Nat. Methods 2006, 3, 721.
- (12) Rittweger, E.; Han, K. Y.; Irvine, S. E.; Eggeling, C.; Hell, S. W. Nat. Photonics 2009, 3, 144.

- (13) Wildanger, D.; Medda, R.; Kastrup, L.; Hell, S. W. *J. Microsc.* 2009, 236, 35.
- (14) Hotta, J.-i.; Fron, E.; Dedecker, P.; Janssen, K. P. F.; Li, C.; Müllen, K.; Harke, B.; Bückers, J.; Hell, S. W.; Hofkens, J. J. *Amer. Chem. Soc.* 2010, 132, 5021.
- (15) Chen, F.; Gerion, D. *Nano Letters* 2004, 4, 1827.
- (16) Boldt, K.; Bruns, O. T.; Gaponik, N.; Eychmüller, A. *The Journal of Physical Chemistry B* 2006, 110, 1959.
- (17) García-Santamaría, F.; Brovelli, S.; Viswanatha, R.; Hollingsworth, J. A.; Htoon, H.; Crooker, S. A.; Klimov, V. I. *Nano Letters* 2011, 11, 687.
- (18) Klimov, V. I.; Mikhailovsky, A. A.; Xu, S.; Malko, A.; Hollingsworth, J. A.; Leatherdale, C. A.; Eisler, H. J.; Bawendi, M. G. *Science* 2000, 290, 314.
- (19) Zhang, C.; Xu, J.; Zhu, T.; Zhang, F.; Tan, Z.; Schiff, S. J.; Su, H.; Gao, S.; Wang, A. Y. *Physical Review B* 2009, 80, 035333.
- (20) Irvine, S. E.; Staudt, T.; Rittweger, E.; Engelhardt, J.; Hell, S. W. *Angewandte Chemie International Edition* 2008, 47, 2685.
- (21) He, Y.; Wang, H.-F.; Yan, X.-P. *Analytical Chemistry* 2008, 80, 3832.
- (22) Chen, Y.; Vela, J.; Htoon, H.; Casson, J. L.; Werder, D. J.; Bussian, D. A.; Klimov, V. I.; Hollingsworth, J. A. *Journal of the American Chemical Society* 2008, 130, 5026.
- (23) García-Santamaría, F.; Chen, Y.; Vela, J.; Schaller, R. D.; Hollingsworth, J. A.; Klimov, V. I. *Nano Letters* 2009, 9, 3482.
- (24) Vela, J.; Htoon, H.; Chen, Y.; Park, Y.-S.; Ghosh, Y.; Goodwin, P. M.; Werner, J. H.; Wells, N. P.; Casson, J. L.; Hollingsworth, J. A. *Journal of Biophotonics* 2010, 3, 706.
- (25) Spinicelli, P.; Buil, S.; Quélin, X.; Mahler, B.; Dubertret, B.; Hermier, J. P. *Physical Review Letters* 2009, 102, 136801.
- (26) Htoon, H.; Malko, A. V.; Bussian, D.; Vela, J.; Chen, Y.; Hollingsworth, J. A.; Klimov, V. I. *Nano Letters* 2010, 10, 2401.
- (27) Guo, Y.; Marchuk, K.; Sampat, S.; Abraham, R.; Fang, N.; Malko, A. V.; Vela, J. *The Journal of Physical Chemistry C* 2011, 116, 2791.
- (28) Lesoine, M. D.; Bose, S.; Petrich, J. W.; Smith, E. A. *The Journal of Physical Chemistry B* 2012, 116, 7821.

- (29) Fitzpatrick, J. A. J.; Yan, Q.; Sieber, J. J.; Dyba, M.; Schwarz, U.; Szent-Gyorgyi, C.; Woolford, C. A.; Berget, P. B.; Waggoner, A. S.; Bruchez, M. P. *Bioconj. Chem.* 2009, 20, 1843.

Table 1. Full-width at half-maximum (fwhm) values obtained for cross-sections of g-NQDs obtained in the images shown in Figure 4.

g-NQD Number from Figure 4	Confocal fwhm (nm)	Luminescence Depletion (time- gated) fwhm (nm)
1	550	34
2	479	35
3	525	42
4	432	30
5	612	44
6	355	33
7	397	38
8	310	51
9	398	43
10	370	45
11	463	55
12	494	62
Average	450 ± 90	40 ± 10

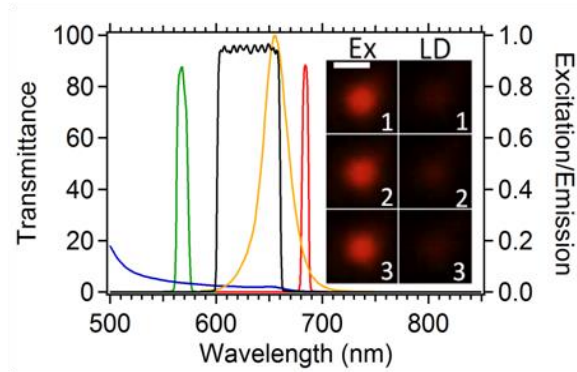


Figure 1. The CdSe/14CdS g-NQDs excitation (blue line) and emission (orange line) spectra and the transmission curves for the microscope's filters are shown. The laser pulses are selected with interference filters with the excitation (green line) and LD (red line) filters centered at 570 ± 10 nm and 684 ± 8 nm, respectively. The band-pass of the LD filter allows significant overlap with the g-NQDs emission spectrum while avoiding unwanted excitation. Two stacked emission filters (black line) centered at 629 ± 56 nm allow the signal to be transmitted to the detection path. The inset shows the QDs LD is reversible with successive images from top to bottom of a single quantum dot obtained with excitation beam illumination (left column) or excitation plus depletion beam illumination (right column), where all beams were Gaussian shaped. The scale-bar is 500 nm.

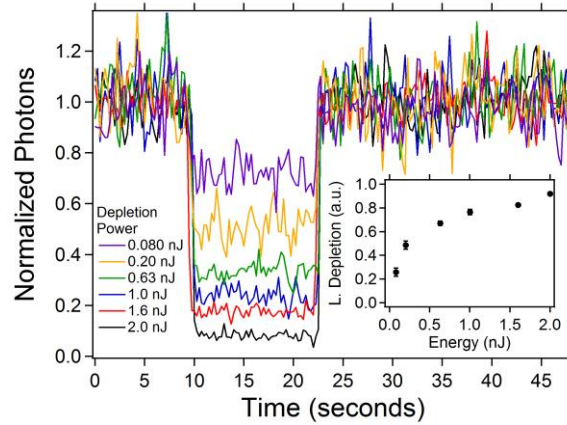


Figure 2. The g-NQD depletion efficiency was measured using continuous illumination with the 50 pJ excitation beam, and overlapping the depletion beam after approximately 10 s had elapsed. The depletion powers ranged from 0.08 to 2 nJ. The data were corrected for a small component of luminescence generated by the depletion beam, but did not need correction for photobleaching. The inset shows the fraction of LD versus depletion laser power.

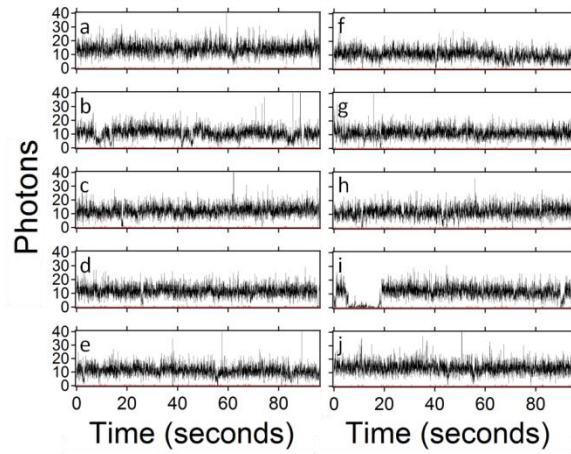


Figure 3. Graphs of the luminescence intensity versus time for 10 individual g-NQDs labeled a to j. The luminescence intensity was integrated every 25 ms for a total of 95 s. The excitation power was the same as used for collecting the LD images (50 pJ). The QD was considered off if the signal dropped below 5 counts for 3 adjacent data points. The data show g-NQDs under the experimental conditions used here were 90 % non-blinking with on-times greater than 99 % and 10 % largely non-blinking with on-times between 99 % and 80 %.

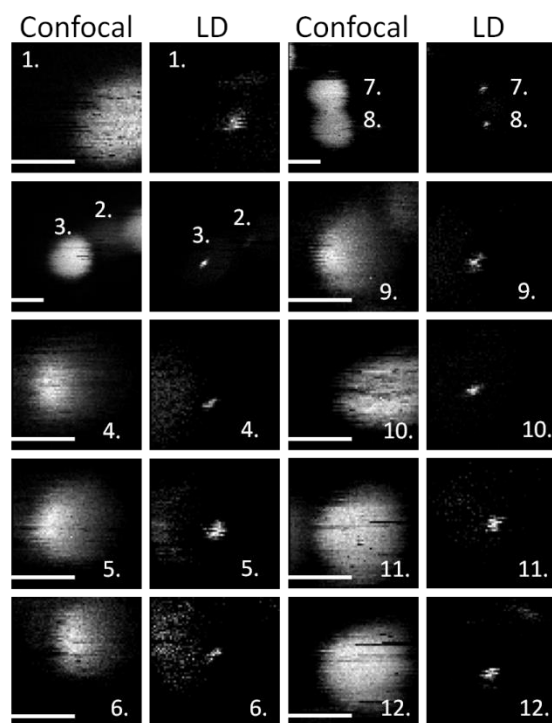


Figure 4. Images of 12 g-NQDs measured in the confocal and LD modes. The confocal images were collected after blocking the depletion beam, and the doughnut shaped depletion beam was unblocked to generate the LD images. The scan direction was from left to right or right to left at a step size of 15.6 nm. A stage repeatability of tens of nanometers results in a small shifts from the confocal to LD image. Scale-bars are all equal to 500 nm.

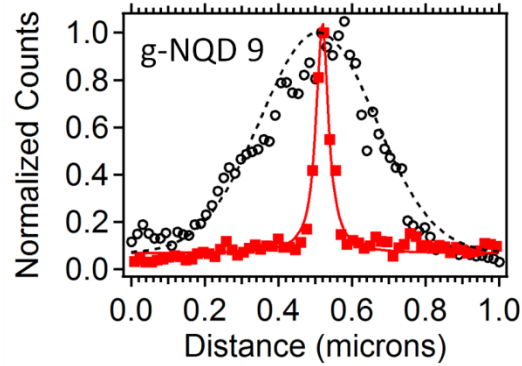


Figure 5. Representative cross-sections and associated fits for a g-NQD in confocal (open circles, Gaussian fit with 398 fwhm) and time-gated LD (solid squares, Lorentzian fit with 43 nm fwhm) modes. The time-gate applied to the LD images yields an improvement of 2.25 fold over the ungated LD data. A $7\times$ average lateral resolution improvement is observed for the time-gated STED data over the system's diffraction limit.

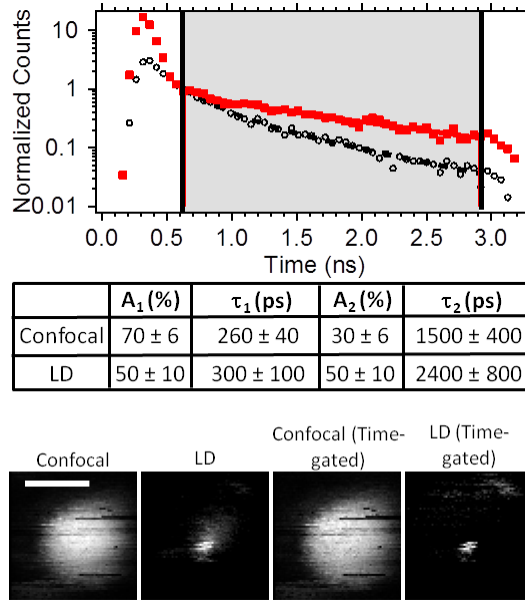


Figure 6. Top: Representative confocal (open circles with dotted line fit) and LD (solid squares with solid line fit) luminescence decay curves are shown at the top of the figure. The vertical lines represent the time-gate that was applied to the LD images in Figure 4. The data have been normalized to the value at 600 ps. Bottom: The two left images show confocal and LD data prior to applying the time-gate and the two right confocal and LD images show the effects of applying the time-gate. The scale-bar is equal to 500 nm

CHAPTER 4 : HIGH ANGULAR-RESOLUTION AUTOMATED VISIBLE-WAVELENGTH SCANNING ANGLE RAMAN SPECTROSCOPY

Michael D. Lesoine, Jonathan M. Bobbitt, Shaobin Zhu, Ning Fang, and Emily A. Smith

Abstract

A 532-nm excitation wavelength scanning angle Raman instrument has been developed to probe chemical content perpendicular to a sample interface. The instrument is fully automated to collect Raman spectra across a range of incident angles from 20.50 to 79.50° with an angular spread of $0.4 \pm 0.2^\circ$ and an angular uncertainty of 0.09° . Instrumental controls drive a rotational stage with a fixed axis of rotation relative to a prism-based sample interface that is mounted on an inverted microscope stage. Three benefits of SA Raman spectroscopy using visible wavelengths, compared to near infrared wavelengths, were demonstrated: (i) better surface sensitivity; (ii) increased signal due to the frequency to the fourth power dependence of the Raman signal, and the possibility for resonant enhancement; (iii) the need to scan a reduced range of angles to shorten data collection times. These benefits were demonstrated with SA Raman measurements of thin polymer films of polystyrene and a diblock copolymer of polystyrene and poly(3-hexylthiophene-2,5-diyl). Thin film spectra were collected with signal-to-noise ratios ranging from 30 to 120 using 0.25 s to 5 minute total acquisition times.

1. Introduction

Raman spectroscopy has been used in many fields to identify the chemical composition of diverse samples [1-7]. Several variants of Raman instruments have been developed, including portable units [8-10] and imaging systems [11, 12]. Another variant of Raman instruments has the capability to probe interfaces using total internal reflection (TIR) illumination [13-26]. These

measurements require the incident laser to be directed at an interface with an incident angle (θ_i) at or above the critical angle (θ_c) as given by Snell's law: $\theta_c = \sin^{-1}\left(\frac{\eta_{\text{sample}}}{\eta_{\text{prism/objective}}}\right)$, where η_{sample} and $\eta_{\text{prism/objective}}$ are the indices of refraction of the interfacial layers. An example sample setup for a TIR experiment is shown in Figure 1. Two layouts to achieve TIR are through the objective and through a high index of refraction prism [16-21, 24, 26, 27]. Through the objective TIR has the benefit of ease of implementation, but is limited to samples with a low index of refraction (e.g., aqueous) and the exact incident angle is rarely known. In addition, the incident angle for a typical TIR objective is limited to a maximum value in the 67° range [28]. The use of a prism generally presents a greater alignment challenge, however, a high index of refraction prism allows a much wider range of samples to be measured and the angle of incidence is easily determined.

We have previously reported a variation of Raman spectroscopy termed scanning angle (SA) Raman spectroscopy [20-23, 25]. SA Raman instruments have a controlled and variable incident angle upon a prism/sample interface in the range of around 25 to 75° with a resolution of a tenth of a degree or less. Three distinct regions in the scanned angular range are below, at, and above the critical angle for total internal reflection. Up to a few orders of magnitude enhancement in the Raman signal is measured at the critical angle. At angles greater than the critical angle, the penetration of the evanescent wave into the sample decreases and these angles are suitable for probing at or near the interface [14-19]. When the sample meets conditions required for a waveguide, spectra collected at angles below the critical angle provide simultaneous information on chemical content and sample thickness [22, 23]. The pattern of the Raman signal as the incident angle is changed upon a waveguide interface can be correlated to sample thickness.

Excitation wavelength is an important experimental parameter for any Raman spectroscopy experiment. The Raman intensity scales with the frequency to the fourth power of the excitation frequency, making shorter excitation wavelengths desirable. However, considerations of the spectral background often make longer excitation wavelengths necessary for many Raman experiments. In addition to these considerations, the excitation wavelength affects the predicted angular dependence of the SA Raman signal. A graph of predicted Raman intensity (i.e., MSEF) versus incident angle for a polystyrene waveguide film shows narrower features with 532 compared to 785-nm excitation (Figure 2A-C). This means sample thickness can be determined by scanning a narrower range of angles using visible excitation wavelengths, and this reduces experiment time. Under TIR, 98% of the Raman scattering is generated in the sample within a distance D_{RS} (equation 1), which is another important parameter that is dependent on the excitation wavelength (λ) and incident angle (θ_i) [26].

$$D_{RS} = \frac{\lambda}{4 \cdot \pi} \frac{1}{\sqrt{[(\eta_{prism}^2 \cdot \sin^2 \theta_i) - \eta_{sample}^2]}} \quad (1)$$

Figure 2D shows example graphs of D_{RS} versus incident angles greater than the critical angle for 785 and 532-nm excitation wavelengths. Visible excitation wavelengths are predicted to produce better surface sensitivity with smaller D_{RS} values for SA Raman measurements.

In this manuscript we characterize a newly developed 532-nm SA Raman instrument that has the benefits of improved design, increased signal due to the short excitation wavelength and resonant enhancement, and decreased D_{RS} for better surface sensitivity. The incident angular range, spread and uncertainty have been characterized, and a comparison of excitation wavelength on the SA Raman signal for several polymer interfaces has been conducted. The

instrument will be of use in a variety of fields where interfacial characterization is needed, particularly in applications that benefit from measurements at ambient laboratory conditions.

2. Experimental Methods

2.1. Instrumentation

The developed instrument can be used for epi-illumination or SA Raman imaging (Figure 3). A single frequency 532-nm laser (Sapphire SF 532 nm 150 mW, Coherent, Santa Clara, CA) set to s-polarization was used for the excitation source. For epi-illumination imaging, the light was directed via a flip down mirror to a 10× beam expander (59-127, Edmund Optics, Barrington, NJ) then the rear port of a DM IRBE microscope (Leica, Wetzlar, Germany). A dichroic mirror (LPD01-532RU-22×27×2.0, Semrock, Rochester, NY) directs the laser to a 10×-magnification 0.25-numerical aperture microscope objective (Leica) that focuses the laser onto the sample plane. For SA Raman imaging, the light was expanded via a 1-3× beam expander (64417, Edmund Optics) to backfill a focusing optic that sends the light into a polarization maintaining single mode fiber (P3-488PM-FC-2, Thorlabs, Newton, NJ). The focusing optic and fiber optic input coupler were mounted on separate translational stages that allow for fine tuning the alignment. The power incident on the fiber was 150 mW and the power exiting the fiber was ~15 mW. A fiber collimator (CFC-2X-A, Thorlabs) at the output end was mounted on a rotational stage (T-RSW60A, Zaber Technologies, Vancouver, British Columbia, Canada) that directs the light with fine control over the incident angles, facilitated by software developed in Labview (2010, National Instruments, Austin, TX), onto a 25.4-mm diameter hemispherical sapphire prism (ISP Optics, Irvington, NY) that was coupled to a 25.4-mm diameter 400- μm thick sapphire substrate. The laser spot size was ~75 μm in diameter at the sample interface in the SA mode.

The Raman signal was collected by a 10× objective, directed to a side port on the microscope, and focused onto the entrance of a HoloSpec $f/1.8i$ spectrograph (Kaiser Optical Systems, Ann Arbor, MI) in both the epi-illumination and SA imaging modes. The spectrometer contains a holographic notch filter (532-nm SuperNotch) and a 100- μ m slit (SLIT-100) and grating (HSG-532-LF). The spectra were collected with a charged coupled device (CCD) (Newton 940, Andor Technology, Belfast, UK) with 2048×512 pixels and Solis software version 4.23.30002.0 (Andor Technology). Two accumulations were collected to facilitate automatic solar ray removal. Images were generated by raster scanning the sample using a XY-translational stage (ProScan, Prior Scientific, Rockland, MA) with a 35 μ m step size.

The reflected light intensity from the prism/sample interface was collected along with the Raman scattering in the SA Raman imaging mode. An amplified photodiode (SM1PD1A and PDA200C, Thorlabs) on a second rotational stage (T-RSW60A, Zaber Technologies) moves in concert with the first rotational stage. The photodiode output voltage was measured with a National Instruments (Austin, TX) NI USB-6221 data acquisition device. Reflectivity measurements were collected at a rate of 1 KHz for 0.5 s per angle with an angular resolution of ~ 0.005 to 0.05° .

2.2. Sample preparation

A thin polystyrene film was made by spin coating 50 μ L of a 4.4 wt% solution of polystyrene (Sigma-Aldrich, St Louis, MO) in toluene (Fisher Scientific, Waltham, MA) on a sapphire substrate at 3000 RPM for one minute utilizing a W-4A spin coater (Chemat Technology, Inc. Northridge, CA). Optical contact between the prism and substrate was established with index matching fluid ($\eta = 1.7800$ Cargille Laboratories, Cedar Grove, NJ). 1.00 and 1.15 wt% NaCl (Fisher Scientific) solutions were prepared in deionized water from an Easy

Pure II purification system (Fisher Scientific). Preparation of a diblock copolymer of polystyrene (15 wt%) and poly(3-hexylthiophene-2,5-diyl) (85 wt%) film (PS-b-P3HT) was made by spin coating 100 μL of a 5 wt% solution in chloroform on a sapphire substrate at 1000 RPM for 40 seconds.

2.3. Data processing and calculations

All data were processed using the software Igor Pro 6.3.2.3 (Wavemetrics, Lake Oswego, OR) or Origin 8.6 (OriginLab, Northampton, MA). Fresnel reflectivity coefficients were calculated and used to fit the experimental reflectivity data to determine the instrumental angle spread and angle uncertainty [29]. The calculations allow the incident angle to have a spread of values rather than a discrete angle. MSEF calculation was performed using EM Explorer (EM Explorer, San Francisco, CA). The refractive indices used in all calculations were $n_{\text{sapphire}} = 1.76355$ [30], $n_{\text{polystyrene}} = 1.59861$ [31], and $n_{\text{air}} = 1.00027821$ [32]. Selected Raman peaks were fit to a Gaussian using Igor Pro's batch-fitting function [33].

To generate images, spectra collected with the Solis software were processed using Igor Pro (Wavemetrics) to obtain peak amplitude, width, and location. The desired properties were input into MATLAB version 2013b (Mathworks, Natick, MA) to construct images.

3. Results and Discussion

3.1. Characterization of instrument specifications

The goal of this work is to demonstrate a SA Raman instrument based on a simple layout and use it for measurements of polymer films that benefit from visible excitation wavelengths. The SA Raman spectrometer utilizes a fiber optic to direct the laser onto a prism/sample interface (Figure 3). The layout has the benefit of few moving parts; and the ability to compare

epi and SA-illumination geometries using a simple flip down mirror. A single rotational stage mounted on the microscope's translational stage was the only moving part required for collecting Raman data. A second rotational stage mounted on the opposite side of the translational stage was used to record the reflected light intensity from the interface. The reflectivity data allows for calibration of the incident angle. The design was compatible with any excitation wavelength. For this work, a 532-nm laser is utilized.

The parameters that need to be determined experimentally for any SA Raman instrument are the angular calibration, range, spread, and uncertainty. A summary of all measured parameters is shown in Table 1. The angular range and spread were characterized by collecting the reflected light intensities from a sapphire/ 364 ± 8 -nm polystyrene interface. The curve of reflected light intensity was fit using Fresnel reflectivity coefficients. First, the experimental curve was adjusted by 4.77° to overlap with the calculated curve at angles below approximately 30° (Figure 4A). This provides an angular calibration, which was necessary since the input angle in the software does not necessarily represent the true incident angle. There was a rapid drop in the reflected light intensity below 20.50° and above 79.50° , within this range was suitable for data collection. The angular range of this instrument was 9° larger than a previously reported instrument that utilized 2 translational stages and a galvanometer to control the incident angle of light upon the interface [20]. Next, the angular spread was characterized by fitting the experimental data in the region between 0.5° below the critical angle and 0.5° above the critical angle. The angular spread in the calculated Fresnel reflectivity coefficients was adjusted until the calculation coincides with extremes established by the uncertainty in the reflectivity data (Figure 4B). The angular spread was $0.4 \pm 0.2^\circ$. This was 2.5° smaller than a previously reported SA Raman instrument [20]. A small angular spread is desirable when measuring and fitting SA

Raman signals, as an average signal is obtained across all incident angles. Near the critical angle, the expected enhancement in the Raman signal decreases by 16% and 38% for a 0.4 and 2.9 degree angular spread, respectively.

Since the reflectivity values were used to calibrate the incident angle of the laser upon the interface, the uncertainty in the reflectivity data also affects the uncertainty in the incident angle. This in turn affects the ability to model SA Raman data. The angular uncertainty was measured using dilute NaCl solutions of varying concentration to alter their refractive index (Figure 5A). Three replicate reflectivity measurements were averaged and the standard deviations were calculated. The average standard deviation for all reflectivity data was 0.04. At the inflection point in both reflectivity curves shown in Figure 4B, a 0.04 uncertainty in the reflectivity corresponds to a 0.09° uncertainty in the incident angle. The mean in reported incident angles has a 0.09° uncertainty combined with a 0.4° spread, as discussed above.

SA Raman instruments require a precise alignment of the laser's axis of rotation with the center of the hemispherical prism. In order to test the sensitivity of the alignment on the resulting data, SA Raman measurements were collected at a fixed incident angle while translating the stage holding the prism/sample. A uniform 364 ± 8 nm thin polystyrene film was used, which should generate a uniform Raman signal. Deviations from a uniform Raman signal were assumed to be introduced as a result of misalignment. As shown in Figure 6 there was a ~ 100 μm oblong region around the center of the prism that yields an optimal signal-to-noise ratio. Outside of this maximal region the signal was considerably decreased. The sample translational stage aids in obtaining the optimal alignment in the SA optical path.

3.2. Considerations of the excitation wavelength for SA Raman spectroscopy: Increased signal and surface sensitivity.

Raman signal intensity is increased with visible relative to near-infrared excitation due to the frequency to the fourth dependence of the Raman signal and also from possible resonant enhancements. A diblock copolymer film composed of semiconducting P3HT and polystyrene (PS-b-P3HT) forms 10 to 12-nm structures surrounded by P3HT under optimal conditions [34]. Thiophene absorbs across the visible region (Figure 7A). For a PS-b-P3HT copolymer film, the thiophene Raman peaks should exhibit resonance enhancement with 532-nm excitation, whereas polystyrene will not.

Raman spectra in Figure 7B show a comparison of 18-mW excitation for 2.5 and 0.125-s acquisition times. As expected, strong thiophene Raman peaks were measured at 1385 and 1455 cm^{-1} for the block copolymer film collected at 72.50°. The signal-to-noise ratios of the thiophene peaks for 2.5 and 0.125 s acquisition times were 120 and 30, respectively. No polystyrene peaks were measured under these experimental conditions due to a lack of resonant enhancement. Figure 7C depicts a two dimensional plot of the Raman signal that seems to exhibit affects from the PS-b-P3HT film roughness. The signal-to-noise ratio for the block copolymer film was 40 for 785-nm excitation (90 mW, 2.5 seconds, data not shown).

One limitation to visible-wavelength SA Raman spectroscopy occurs when measurements at a gold interface are performed. Excitation with a 785-nm laser generates larger SA Raman signals and enables the measurement of a monolayer with optimized thin films of ~50-nm gold, whereas no signal was generated using 532-nm excitation (data not shown).

3.3. Considerations of the excitation wavelength for SA Raman spectroscopy: Decreased scanning angular range.

In order to demonstrate the ability to measure polymer waveguide thickness using a narrow range of incident angles, SA Raman spectra were collected for a thin polystyrene film prepared by spin coating a 5 wt% solution onto a substrate. The Raman spectra were collected every 0.05° over the angular range 55.50 to 68.00° (Figure 8). The intensity of the Raman signal varies with incident angle, as expected, and the maximum Raman signal was measured at 59.25° . Matching this experimentally determined maximum with calculations of the mean squared electric field [23] within polymer layers of varying thickness, the polystyrene film was measured to be 420 nm (Figure 8). The minimum polystyrene thickness required to support a waveguide using 532-nm excitation is ~ 170 nm (thinner films can be measured as waveguides using visible wavelengths compared to near infrared wavelengths). Thinner waveguides require a larger range of angles to be scanned compared to thicker waveguides (Figure 2). At the opposite thickness extreme, polystyrene films of greater than 1000 nm require a high angular resolution as a result of the narrow waveguide peaks. The instrument described herein has the scanning capabilities and angular resolution to simultaneously measure the thickness and composition at both thickness extremes.

4. Conclusions

An automated visible-wavelength SA Raman instrument was constructed with an angular range of 20.50° to 79.50° , uncertainty of 0.09° and spread of $0.4^\circ \pm 0.2^\circ$. The instrument's function was demonstrated by measuring thin polymer films. It was demonstrated that visible wavelength SA Raman spectroscopy generates better signal-to-noise ratio spectra, better surface sensitivity under TIR, and the need to scan a narrower range of angles when measuring waveguides compared to the use of infrared lasers. Increased surface sensitivity and signals will

make it possible to measure faster kinetics and dynamic events than was previously possible with SA Raman spectroscopy. In addition, the coupling of resonant conditions to enhance sample detection without the use of specialized substrates (e.g., plasmon supporting) will prove beneficial and expand the utility of the technique.

Acknowledgements

This research is supported by the U.S. Department of Energy, Office of Basic Energy Sciences, Division of Chemical Sciences, Geosciences, and Biosciences through the Ames Laboratory. The Ames Laboratory is operated for the U.S. Department of Energy by Iowa State University under Contract No. DE-AC02-07CH11358.

References

1. Delhaye, M., M. Bridoux, and F. Wallart, *Time and/or space resolved laser Raman spectroscopy*. Journal of Molecular Structure, 1982. **79**(0): p. 51-66.
2. Vendrell, M., et al., *Surface-enhanced Raman scattering in cancer detection and imaging*. Trends in Biotechnology, 2013. **31**(4): p. 249-257.
3. Poliakoff, M., S.M. Howdle, and S.G. Kazarian, *Vibrational Spectroscopy in Supercritical Fluids: From Analysis and Hydrogen Bonding to Polymers and Synthesis*. Angewandte Chemie International Edition in English, 1995. **34**(12): p. 1275-1295.
4. Weckhuysen, B.M., *Snapshots of a working catalyst: possibilities and limitations of in situ spectroscopy in the field of heterogeneous catalysis*. Chemical Communications, 2002(2): p. 97-110.
5. Biju, V., et al., *Semiconductor quantum dots and metal nanoparticles: syntheses, optical properties, and biological applications*. Analytical & Bioanalytical Chemistry, 2008. **391**(7): p. 2469-2495.
6. Stuart, D.A., et al., *Biological applications of localised surface plasmonic phenomena*. IEE Proceedings -- Nanobiotechnology, 2005. **152**(1): p. 13-32.
7. Lupoi, J., et al., *Assessment of Lignocellulosic Biomass Using Analytical Spectroscopy: an Evolution to High-Throughput Techniques*. BioEnergy Research, 2014. **7**(1): p. 1-23.

8. Cullum, B.M., et al., *Development of a compact, handheld Raman instrument with no moving parts for use in field analysis*. Review of Scientific Instruments, 2000. **71**(4): p. 1602-1607.
9. Zhang, X., et al., *Rapid Detection of an Anthrax Biomarker by Surface-Enhanced Raman Spectroscopy*. Journal of the American Chemical Society, 2005. **127**(12): p. 4484-4489.
10. Kudelski, A., *Analytical applications of Raman spectroscopy*. Talanta, 2008. **76**(1): p. 1-8.
11. Weiss, I.M., et al., *Mollusc larval shell formation: amorphous calcium carbonate is a precursor phase for aragonite*. Journal of Experimental Zoology, 2002. **293**(5): p. 478-491.
12. Keren, S., et al., *Noninvasive molecular imaging of small living subjects using Raman spectroscopy*. Proceedings of the National Academy of Sciences, 2008. **105**(15): p. 5844-5849.
13. Ikeshoji, T., Y. Ono, and T. Mizuno, *Total Reflection Raman Spectra; Raman Scattering due to the Evanescent Wave in Total Reflection*. Applied Optics, 1973. **12**(10): p. 2236-2237.
14. Iwamoto, R., et al., *Total internal reflection Raman spectroscopy as a new tool for surface analysis*. Journal of the American Chemical Society, 1980. **102**(3): p. 1212-1213.
15. Iwamoto, R., et al., *Total Internal Reflection Raman Spectroscopy at the Critical Angle for Raman Measurements of Thin Films*. Applied Spectroscopy, 1981. **35**(6): p. 584-587.
16. Fujiwara, K. and H. Watarai, *Total Internal Reflection Resonance Raman Microspectroscopy for the Liquid/Liquid Interface. Ion-Association Adsorption of Cationic Mn(III) Porphine*. Langmuir, 2003. **19**(7): p. 2658-2664.
17. Tisinger, L.G. and A.J. Sommer, *Attenuated Total Internal Reflection (ATR) Raman Microspectroscopy*. Microscopy and Microanalysis, 2004. **10**(Supplement S02): p. 1318-1319.
18. Greene, P.R. and C.D. Bain, *Total internal reflection Raman spectroscopy of barley leaf epicuticular waxes in vivo*. Colloids and Surfaces B: Biointerfaces, 2005. **45**(3-4): p. 174-180.
19. Beattie, D.A., M.L. Larsson, and A.R. Holmgren, *In situ total internal reflection Raman spectroscopy of surfactant adsorption at a mineral surface*. Vibrational Spectroscopy, 2006. **41**(2): p. 198-204.
20. McKee, K.J. and E.A. Smith, *Development of a scanning angle total internal reflection Raman spectrometer*. Review of Scientific Instruments, 2010. **81**(4): p. -.

21. McKee, K.J., M.W. Meyer, and E.A. Smith, *Near IR Scanning Angle Total Internal Reflection Raman Spectroscopy at Smooth Gold Films*. Analytical Chemistry, 2012. **84**(10): p. 4300-4306.
22. McKee, K.J., M.W. Meyer, and E.A. Smith, *Plasmon Waveguide Resonance Raman Spectroscopy*. Analytical Chemistry, 2012. **84**(21): p. 9049-9055.
23. Meyer, M.W., et al., *Scanning Angle Plasmon Waveguide Resonance Raman Spectroscopy for the Analysis of Thin Polystyrene Films*. The Journal of Physical Chemistry C, 2012. **116**(47): p. 24987-24992.
24. Woods, D.A. and C.D. Bain, *Total internal reflection Raman spectroscopy*. Analyst, 2012. **137**(1): p. 35-48.
25. Meyer, M.W., V.H.T. Nguyen, and E.A. Smith, *Scanning angle Raman spectroscopy measurements of thin polymer films for thickness and composition analyses*. Vibrational Spectroscopy, 2013. **65**(0): p. 94-100.
26. Greene, P.R. and C.D. Bain, *Spectroscopy Europe*, 2004. **16**(8): p. 8-15.
27. Greene, P., *Total internal reflection Raman spectroscopy*. SpectroscopyEurope, 2004. **16**(4).
28. Paige, M.F., E.J. Bjerneld, and W.E. Moerner, *A Comparison of Through-the-Objective Total Internal Reflection Microscopy and Epifluorescence Microscopy for Single-Molecule Fluorescence Imaging*. Single Molecules, 2001. **2**(3): p. 191-201.
29. Corn, R.M. 2014 [cited 2014 1/18]; Available from: <http://www.corninfo.ps.uci.edu/calculations.html>.
30. Bass, M., et al., *Handbook of Optics, Third Edition Volume IV: Optical Properties of Materials, Nonlinear Optics, Quantum Optics (set)*. 2009: Mcgraw-hill.
31. Kasarova, S.N., et al., *Analysis of the dispersion of optical plastic materials*. Optical Materials, 2007. **29**(11): p. 1481-1490.
32. Ciddor, P.E., *Refractive index of air: new equations for the visible and near infrared*. Applied Optics, 1996. **35**(9): p. 1566-1573.
33. Bradley, M.S. and J.H. Krech, *High-pressure Raman spectra of the acetone carbon-carbon stretch in binary liquid mixtures with methanol*. The Journal of Physical Chemistry, 1992. **96**(1): p. 75-79.
34. Sun, Z., et al., *PS-b-P3HT Copolymers as P3HT/PCBM Interfacial Compatibilizers for High Efficiency Photovoltaics*. Advanced Materials, 2011. **23**(46): p. 5529-5535.

Table 1. Measured instrumental parameters for the 532-nm SA Raman instrument and calculated values for a sapphire/polystyrene interface.

Spectral Range^a	150-2460 cm ⁻¹
Incident angle spread	0.4° ± 0.2°
Incident angle uncertainty	0.09°
Highest angle	79.50°
Lowest angle	20.50°
Values for a sapphire/polystyrene interface (532 nm excitation)	
θ_c	65.05°
D_{RS} range (65.05-79.50°)	1.3 μm-63 nm
Average ΔD_{RS} near the θ_c (65.50-66.00)	7.8 nm
Average ΔD_{RS} far from the θ_c (75.00-79.50)	0.1 nm

a lower value limited by notch filter, upper value limited by grating and detector

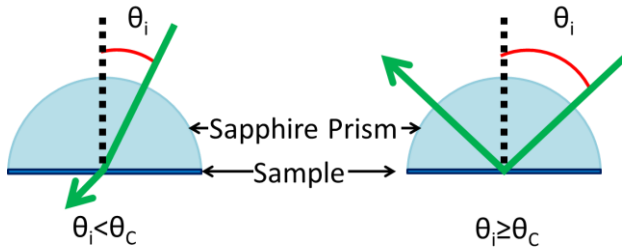


Figure 1. Sapphire/polystyrene interface showing transmission and reflection of the incident excitation light (left) below and (right) at or above the critical angle, respectively.

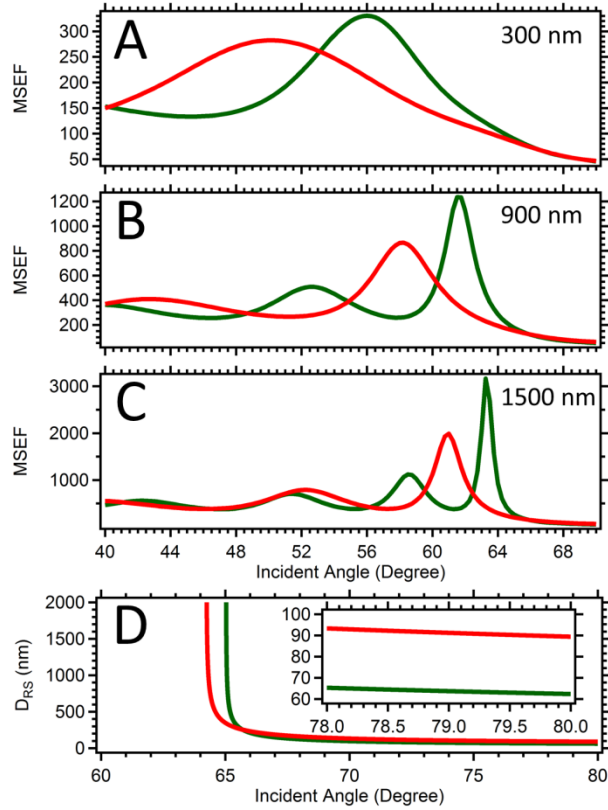


Figure 2: Comparison of the sum of the mean squared electric field (MSEF) for sapphire/(A) 300 nm, (B) 600 nm, and (C) 1500 nm sapphire/polystyrene interfaces for (green) 532 and (red) 785-nm excitation. (D) shows a comparison of the axial distance over which Raman scattering is collected (D_{RS}) as a function of incident angle for (green) 532 and (red) 785-nm excitation, where an enhanced surface sensitivity is visible in the case of the 532-nm excitation.

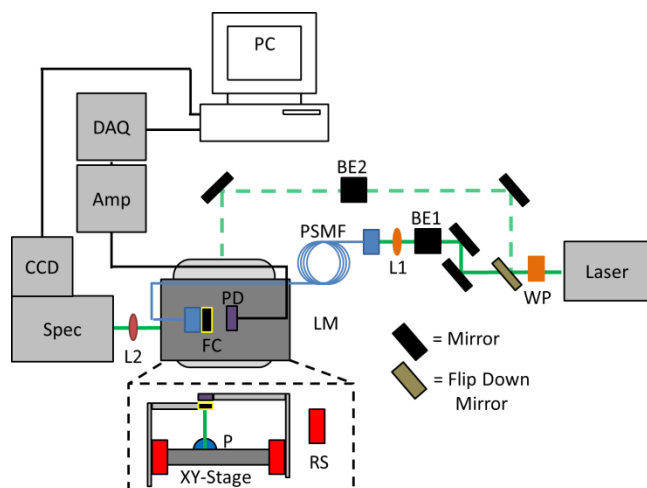


Figure 3: Instrument schematic for a 532-nm SA Raman instrument: half wave-plate (WP), beam expanders (BE1, BE2), Leica microscope (LM), aspheric focusing lens (L1), polarization-maintaining single-mode fiber optic (PSMF), fiber collimator (FC), high index prism (P), photo-diode (PD), rotational stages (RS), amplifier (Amp), data acquisition device (DAQ), computer (CPU), collection lens (L2), spectrometer (Spec), and charged-coupled device (CCD). The dashed view is perpendicular to the table.

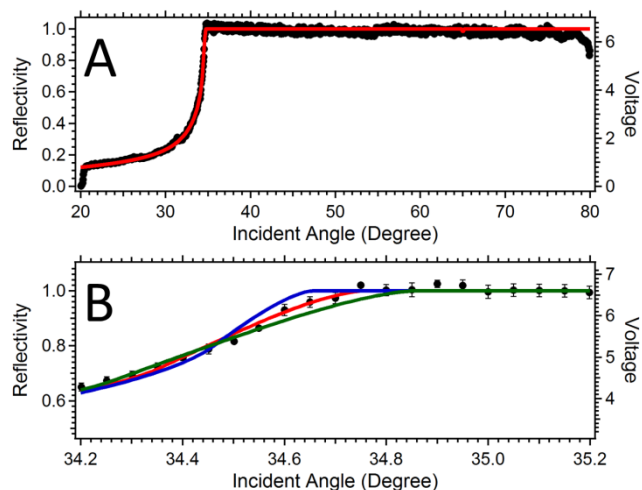


Figure 4: Reflectivity curve from (A) sapphire/ 364 ± 8 nm polystyrene/air interface (black squares) with a best fit Fresnel reflectivity curve that has a $0.4 \pm 0.2^\circ$ incident angle spread (red line). (B) Expanded view of (A) near the critical angle with Fresnel reflectivity curves corresponding to an angle spreads of 0.2° (blue line), 0.4° , and 0.6° (green line). Signal was collected every 0.05° between adjacent data points.

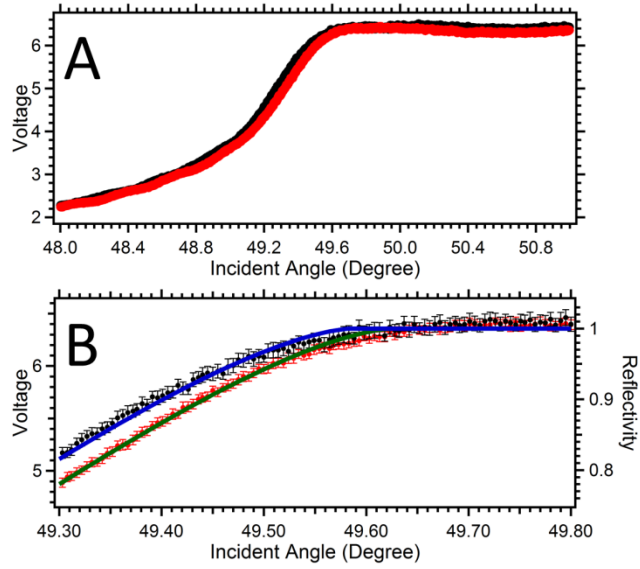


Figure 5: (A) Comparison of the reflectivity curves of a (black circles) 1.00 and (red circles) 1.15 wt% NaCl solutions. (B) An expanded view around the inflection points to accentuate the difference in the two curves.

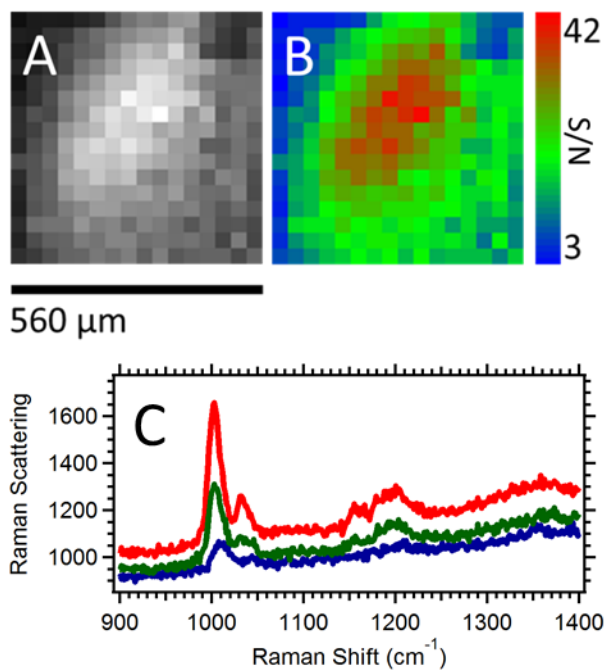


Figure 6: Images taken in the SA mode of a 364 ± 8 nm polystyrene film depicting the (A) magnitude and (B) an associated signal-to-noise ratio of the ~ 1000 cm⁻¹ peak. (C) Raman spectra over the range of signal-to-noise values with corresponding color code shown in (B). Raman measurements were collected with an acquisition time of 15 seconds and a laser power of 15 mW with a step size of 35 μ m.

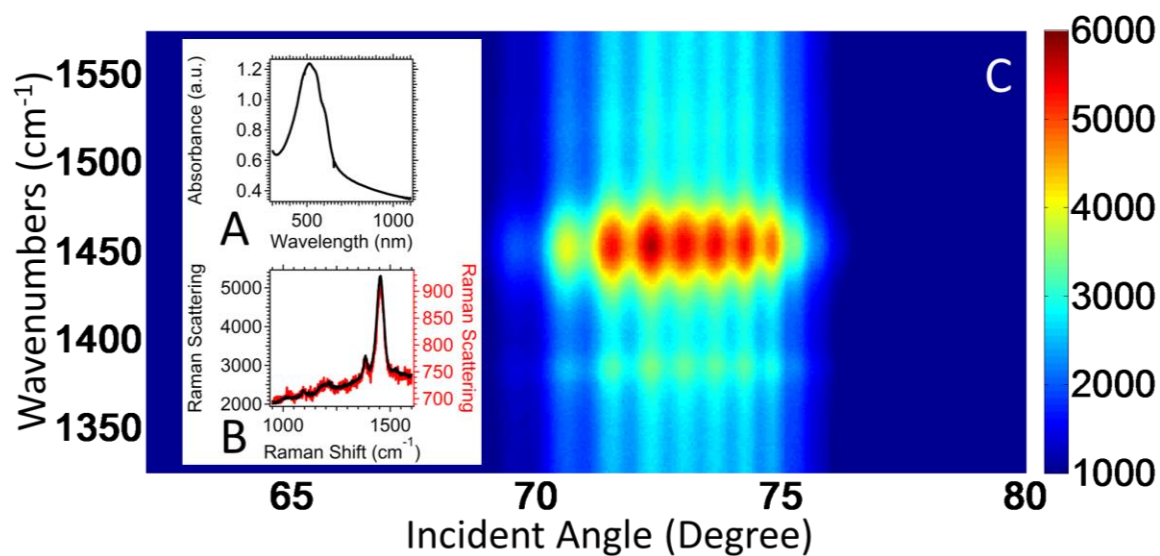


Figure 7: (A) Absorption spectrum of a 490 ± 60 -nm thin film of PS-b-P3HT. (B) Raman measurements of the film at 532 nm with two 2.5 s (black) or 0.125 s (red) collections. (C) A plot of Raman scattering intensity as function of wavenumber and incident angle.

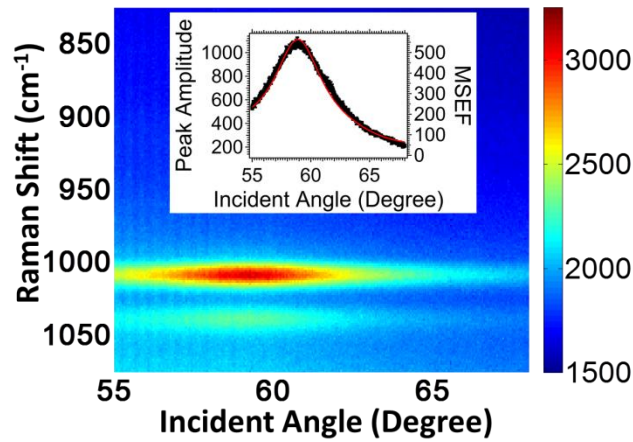


Figure 8: SA Raman spectra of a 420-nm polystyrene film. The $\sim 1007 \text{ cm}^{-1}$ peak exhibits an angle-dependent signal, as expected for a waveguide. The maximum signal is measured at 59.25° . The critical angle for the interface is 65.04° . The thin film's Raman data was best modeled (MSEF) to a 420-nm thickness, as shown in the inset. Two collections of 2.5 minutes were used to obtain each spectrum.

Chapter 5 : QUANTITATIVE COMPARISON OF HIGH EFFICENCY HETEROJUNCTION SOLAR CELL STABILTY UNDER LASER INDUCED PHOTODEGRADATION

Michael D. Lesoine, John A. Carr, Jonathan M. Bobbitt, Daniel J. Freppon, Moneim Elshobaki, Sumit Chaudhary, and Emily A. Smith

Abstract:

Solar cells formed with bulk heterojunctions containing combinations of thiophene based polymer donors poly(3-hexylthiophene-2,5-diyl) (P3HT), poly[[9-(1-octylnonyl)-9H-carbazole-2,7-diyl]-2,5-thiophenediyl-2,1,3-benzothiadiazole-4,7-diyl-2,5-thiophenediyl] (PCDTBT), or poly({4,8-bis[(2-ethylhexyl)oxy]benzo[1,2-b:4,5-b']dithiophene-2,6-diyl}{3-fluoro-2-[(2-ethylhexyl)carbonyl]thieno[3,4-b]thiophenediyl}) (PTB7) and the fullerene acceptor 3'Phenyl-3'H-cyclopropa[8,25] [5,6]fullerene-C70-D5h(6)-3'butanoic acid (PCBM) are examined for stability using resonance Raman spectroscopy with 532-nm laser excitation to induce photodegradation. Four different sample preparations are performed two of which involve allowing the solar heterojunctions to dry under ambient conditions, but different thickness and one thicker and thinner sample undergoing solvent an thermal annealing, respectively. such as the method of drying as well as thermal annealing of the solar cells and the effect is observed For Raman spectra crystallinity is observed by observing a peak corresponding to a thiophene group's full-width at half-maximum and location measured as a function of illumination time with increasing laser power densities from 7×10^2 - 7×10^4 Wcm⁻². The crystallinity of P3HT improves with added preparative steps while PCDTBT ant PTB7 remain with the same order as cast. In addition, changes to luminescence in the collected spectra over time are examined. Average values for spectral quantities for a peak's full-width at half-maximum and location were

obtained for different locations on the heterojunctions and are correlated to relative order and disorder with regard to time and laser power to induce degradation. PTB7 exhibited the highest degree of degradation possibly from oxidative affects.

Introduction:

Solar cell research is typically focused on how efficiently a constructed device can convert solar radiation into an energy source, however, of equal importance is the development of stable solar cells that have long operable lifetimes. [1-9] Polymer solar cells are composed of a donor such as poly(3-hexylthiophene-2,5-diyl) (P3HT), and an acceptor 3'Phenyl-3'H-cyclopropa[8,25] [5,6]fullerene-C₇₀-D₅h(6)-3'butanoic acid (PCBM). Other less studied donors include poly[[9-(1-octylonyl)-9H-carbazole-2,7-diyl]-2,5-thiophenediyl-2,1,3-benzothiadiazole-4,7-diyl-2,5-thiophenediyl] (PCDTBT), and poly({4,8-bis[(2-ethylhexyl)oxy]benzo[1,2-b:4,5-b']dithiophene-2,6-diyl}{3-fluoro-2-[(2-ethylhexyl)carbonyl]thieno[3,4-b]thiophenediyl}) (PTB7). Research to improve heterojunction devices is critical to create devices suitable for real world applications. Polymers used in the heterojunctions have been shown to have a greater longevity when organic impurities are removed having the short-circuit current density of cells stored in inert conditions only dropping ~7% after 111 days. [5] Substituted PCBM's have shown promise in allowing for increased annealing times up to 10 hours while avoiding degradation of device efficiency. [1] Work has also been done with optimization of the PEDOT:PSS layer by treatment with ultraviolet light to improve the wettability that has a direct effect on the solar cell's active layer increasing stability by 2.5 times and improving efficiency from 2.43% to 3.64% of the observed device. [6]

Heterojunction solar cells are being optimized with different preparation conditions involving thermal [1, 4, 9-11] and solvent[12] annealing as well as modifications to the

traditionally used components in a device's strata. Raman spectroscopy is useful in determining differences in chemical structures relating to crystallinity. Correlations have been drawn between the crystallinity of organic photovoltaic materials such as P3HT and the full width at half maximum (FWHM) of thiophene groups [12-16]. The use of resonance Raman spectroscopy facilitates collection of data that can be correlated to crystallinity on the order of seconds [17, 18].

In this work we determine the stability of ultra-thin bulk heterojunction solar cells prepared under differing conditions as determined by laser induced photodegradation and resonance Raman spectroscopy. Trends for changes to crystallinity using thiophene based peaks FWHMs of Raman spectra under low power observation of P3HT:PCBM, PCDTBT:PCBMT, and PTB7:PCBM are comparable with results previously observed using alternate techniques. High power laser induced photodegradation studies reveal changes to the polymer structure involving possible accelerated oxidative damage.

Experimental Methods:

Film preparation:

Solar cells are generated with the strata oriented as in Figure 1 with first taking glass substrates coated with an ~70 nm layer of ITO are first spin coated with a mixture of poly(3,4-ethylenedioxythiophene) and poly(styrenesulfonate) (PEDOT:PSS) at 4,000 rpm for 60 s to form an ~10 nm layer followed by a mix of one of the three donor materials P3HT, PCDTBT, or PTB7 mixed with the acceptor PCBM to generate the solar cells. The specific spin coating parameters for the donors are contained in Table 1. Four samples were made with varying conditions for the three different heterojunction material blends of P3HT, PCDTBT, and PTB7.

The notations of samples superscripted with α and γ correspond to samples that are dried under ambient conditions without annealing being thicker and thinner, respectively, while β and Δ correspond to solvent annealed (thicker) and thermally annealed (thinner) samples, respectively. Preparations were all performed in a nitrogen environment. The PCDTBT:PCBM and PTB7:PCBM samples are allowed to dry for 24 hours in a vacuum.

Spectral measurements:

A lab-built microscope-based Raman spectrometer using a DM IRBE microscope (Leica, Wetzlar, Germany) and with laser excitation at 532-nm (Sapphire SF 532 nm 150 mW, Coherent, Santa Clara, CA) is used to perform the Raman measurements. Laser excitation powers of 50-5000 μW are used in the examination of the samples. The power density for the 50-5000 μW range corresponds to 7×10^2 - $7 \times 10^4 \text{ Wcm}^{-2}$. The laser profile is expanded using a 10 \times beam expander (59-127, Edmund Optics, Barrington, NJ) in order to backfill a 10 \times -magnification 0.25-numerical aperture microscope objective (Leica) to achieve an approximately diffraction limited laser spot with a diameter of $\sim 1 \mu\text{m}$. The objective is used to both focus the laser for excitation as well as collect the Raman scattering signal from the the epi-direction. The Raman signal is focused with a lens onto a HoloSpec $f/1.8i$ spectrograph (Kaiser Optical Systems, Ann Arbor, MI) and directed to a charged coupled device (CCD) (Newton 940, Andor Technology, Belfast, UK) having 2048×512 pixels.

Raman spectra are obtained using Solis software version 4.23.30002.0 (Andor Technology). Collection times between 1-150 s are used depending on the excitation power in order to maintain a consistent S/N ratio through the measurements. Two collections are performed to facilitate cosmic ray removal.

Raman image collection is accomplished by raster scanning with lab developed software generated using Labview. A laser power of 50 μW is used to prevent sample damage with a collection time of 15 s and a stage movement of 1 μm between points is used.

An Agilent 8453 UV-visible spectrophotometer (Santa Clara, CA) is used for the collection of absorption spectra.

Data collection and analysis:

Heterojunction solar cells are either probed at many locations to gain average values or one location over time to track the stability of spectral properties under laser induced photodegradation using controls developed using the 2010 version of Labview (National Instruments, Austin, TX) to translate a sample using a XY-stage (ProScan, Prior Scientific, Rockland, MA). Raman spectra are analyzed using Igor Pro 6.3.2.3 (Wavemetrics, Lake Oswego, OR) using the batch fit function with a Gaussian fit. The spectral properties of a peak of interests FWHM and location are each plotted separately versus time for the stability measurements. In addition, luminescences of the collected Raman spectra are also correlated with time by comparison of spectral changes to the background across samples at a region without spectral features at 2000 cm^{-1} .

Results And Discussion:

Heterojunction solar cell's crystallinity measured by resonance Raman microscopy:

Raman measurements are performed to determine the effect of additional preparative conditions on the crystallinity of ultra-thin heterojunction solar cells. P3HT, PCDTBT, and PTB7 have one, two, and four thiophene groups per monomer, respectively. Thiophene exhibits resonantly enhanced Raman spectra using 532-nm excitation as shown by the absorption spectra

in Figure 2. The Raman spectra measured for bulk heterojunction films containing P3HT:PCBM, PCDTBT:PCBM, or PTB7 are shown in Figure 1. There is an $\sim 10\times$ higher signal for P3HT compared to PCDTBT and PTB7, which have about the same relative signal and similar thicknesses of 180.6 ± 0.7 nm, 180 ± 10 nm, and 160 ± 10 nm, respectively. For all subsequent Raman measurements with the PCDTBT and PTB7 a $10\times$ longer acquisition time is used to achieve a similar signal-to-noise ratio (Table 2) with the P3HT samples.

Comparison of polymer order after different annealing conditions:

Efficiency of solar devices can be correlated to the polymer's crystallinity. Raman spectroscopy gives a measure of crystallinity by examining the changes in the FWHM of the thiophene symmetric stretching as well as the peak location in P3HT based bulk heterojunction solar devices. [12-16] Smaller FWHM or Raman shifts of the thiophene group's Raman peak corresponds to a higher polymer order.

The polymer order is measured for P3HT:PCBM, PCDTBT:PCBM, and PTB7:PCBM films prepared with different processing conditions. The FWHM and peak location was measured for one peak in each Raman spectrum (Table 2). The peaks that were measured are the thiophene group at ~ 1450 cm^{-1} for P3HT [10, 14], a broad ring stretch spanning the two thiophenes and the benzothiadiazole at ~ 1447 cm^{-1} for PCDTBT [19], and the 3-fluorothiophene group at ~ 1490 cm^{-1} for PTB7 [20].

P3HT:PCBM shows significant changes to polymer order with varying sample preparation methods, it is the only sample that shows statistically significant changes in the FWHM and Raman shift for the four preparation methods (Table 2). The relative order is highest for P3HT ^{β} and decreases in the order P3HT ^{Δ} , P3HT ^{γ} , and P3HT ^{α} . In the case of PTB7:PCBM

the only statistically significant change in the thiophene peak properties is a small Raman shift for the thicker PTB7^α and PTB7^β versus the thinner PTB7^γ PTB7^Δ samples. In the case of PTB7, there are no statistically significant changes in the thiophene peak's FWHM. However, due to luminescence evolving in the PTB7:PCBM sample the uncertainty is increased with the peak location and FWHM data deriving from the fits used to model the data. As measured by Raman spectroscopy, PCDTBT:PCBM is relatively unaffected by the preparation conditions, though slight differences are measured in the peak location for annealing conditions of 80 versus 200 C° (Table 3). This finding is supported by neutron reflectivity and grazing incidence wide-angle X-ray scattering measurements that showed thermal annealing has a negligible effect on PCDTBT order. [21] Absorption spectra are susceptible to changes in the aggregation of PCBM [22] and for the three heterojunction materials (Figure 2) the results agree with the polymer order measured by Raman spectroscopy. Changes to the shape of the P3HT:PCBM spectra correspond to changes occurring under solvent and thermal annealing conditions used. PCDTBT:PCBM and PTB7:PCBM both show insignificant changes in their absorption spectra under solvent annealing conditions and differences present are attributable to intensity differences based on sample thicknesses,

The inset for the P3HT:PCBM mixture of Figure 1 corresponds to images generated from FWHM taken from Raman spectra measured about the center of the samples. For the bulk of the sample in each case there is a high degree of uniformity. PCBM enriched domains have been measured (data not shown) but these correspond to a very small portion of the total films as prepared.

Stability measurements with increasing laser power density:

Laser illumination for Raman measurements can degrade bulk heterojunction solar polymers over time. High NA objectives can lead to substantial laser power densities that can hasten a samples degradation. Therefore, there is importance in determining the optimal laser power for Raman excitation to ensure the integrity of data collection. In order to enable easy visualization of the data spectra are background subtracted and normalized to the thiophene Raman peak being observed (Figure 3). The P3HT:PCBM solar cells are illuminated with laser powers from 50-5000 μW to visualize the stability of the device over time (Figure 4). At 50 μW the FWHM visualized in the images of Figure 4 show consistency over time, however, at higher laser powers the FWHM starts to broaden and peak center location undergoes a blue shift. In the case of PCDTBT:PCBM (Figure 5) no significant changes occurred with the different conditions, however, the FWHM of the thiophene peak did progressively increase at higher laser power. Table 4 contains information for P3HT:PCBM and PCDTBT:PCBM for the initial and end time points for FWHM and peak location and displays significant changes to these quantities for increasing laser power. PTB7:PCBM (Figure 6) also follows a trend of no significant change for varied preparation conditions and the evolution of luminescence is present at all excitation powers resulting in complications to fitting the 3-fluorothiophene peak being observed at later time points. Furthermore, not only must each polymer have the most appropriate conditions determined, but also each preparation. In order to simplify this task where many preparations are performed it is best to use a power several order of magnitude below where a damage threshold is found. Even at low powers, however, each of the three solar polymers experienced different trends in regard to luminescence (Figure 7). P3HT:PCBM, PCDTBT:PCBM, and PTB7:PCBM exhibited a decrease, no change, and increase in luminescence, respectively.

The laser power used should not influence the Raman measurement when characterization of a solar cell is performed, however, such influences from photodegradation can be useful in observing the nature of a solar cell's stability. Raman spectroscopic measurements conducted by laser excitation at energy densities of $7 \times 10^2 - 7 \times 10^4 \text{ Wcm}^{-2}$ for P3HT:PCBM and $14 \times 10^2 - 7 \times 10^4 \text{ Wcm}^{-2}$ for PCDTBT:PCBM and PTB7:PCBM are used to determine the stability of the bulk heterojunction solar cells. The bulk material of the films are examined using an approximately $\sim 1.5 \mu\text{m}$ excitation spot size. Images generated from the FWHM's of the thiophene peak in P3HT (Figure 11) show that at a laser power of $\sim 7 \times 10^2 \text{ Wcm}^{-2}$ that there is uniformity for each of the sample preparation conditions (Table 1). In contrast when aggregates of PCBM are observed (Figure 12) there can be significant variance to the FWHM measured that correlates to a perturbation in order around these features from the bulk. Average orders of the solar cells of P3HT:PCBM, PCDTBT:PCBM, and PTB7:PCBM involved point measurements of Raman spectra and the analysis of the FWHM and peak location of the thiophene peak (Table 2). Of note is a phenomenon where the stability of PTB7:PCBM is increased under an aluminum contact relative to the bulk of the solar device where no change occurs over time (Figure 8).

Conclusion:

Heterojunction solar cells probed with increasing laser intensity reveal through laser induced photodegradation facilitated by resonance Raman spectroscopy changes to the order. Solar cells at laser energy densities as low as $\sim 7 \times 10^2 \text{ Wcm}^{-2}$. This is to ensure the fidelity of a measurement is not affected by the laser. Changes to order for different preparation and annealing conditions were most easily observed with statistical changes for P3HT and PTB7, while PCDTBT exhibited not statistical difference to the measured order. Using of higher laser

powers can degrade a sample and result in significant changes to measured order and changes to the luminescence associated with the polymer mixes observed. The use of accelerated degradation of heterojunction solar allows for a rapid means to determine the effect of sample alteration to the end of improving durability.

Acknowledgments:

This research is supported by the U.S. Department of Energy, Office of Basic Energy Sciences, Division of Chemical Sciences, Geosciences, and Biosciences through the Ames Laboratory. The Ames Laboratory is operated for the U.S. Department of Energy by Iowa State University under Contract No. DE-AC02-07CH11358.

References

1. Zhang, Y., et al., *A Simple and Effective Way of Achieving Highly Efficient and Thermally Stable Bulk-Heterojunction Polymer Solar Cells Using Amorphous Fullerene Derivatives as Electron Acceptor*. Chemistry of Materials, 2009. **21**(13): p. 2598-2600.
2. Zimmermann, B., U. Würfel, and M. Niggemann, *Longterm stability of efficient inverted P3HT:PCBM solar cells*. Solar Energy Materials and Solar Cells, 2009. **93**(4): p. 491-496.
3. Hsieh, C.-H., et al., *Highly Efficient and Stable Inverted Polymer Solar Cells Integrated with a Cross-Linked Fullerene Material as an Interlayer*. Journal of the American Chemical Society, 2010. **132**(13): p. 4887-4893.
4. He, D., et al., *Improving the stability of P3HT/PC61BM solar cells by a thermal crosslinker*. Journal of Materials Chemistry A, 2013. **1**(14): p. 4589-4594.
5. Mateker, W.R., et al., *Improving the long-term stability of PBDTTPD polymer solar cells through material purification aimed at removing organic impurities*. Energy & Environmental Science, 2013. **6**(8): p. 2529-2537.
6. Xu, X.-J., et al., *Enhanced Performance and Stability in Polymer Photovoltaic Cells Using Ultraviolet-Treated PEDOT:PSS*. Chinese Physics Letters, 2013. **30**(7): p. 077201.
7. Gevorgyan, S.A., M. Jørgensen, and F.C. Krebs, *A setup for studying stability and degradation of polymer solar cells*. Solar Energy Materials and Solar Cells, 2008. **92**(7): p. 736-745.

8. Krebs, F.C., *Air stable polymer photovoltaics based on a process free from vacuum steps and fullerenes*. Solar Energy Materials and Solar Cells, 2008. **92**(7): p. 715-726.
9. Krebs, F.C. and H. Spanggaard, *Significant Improvement of Polymer Solar Cell Stability†*. Chemistry of Materials, 2005. **17**(21): p. 5235-5237.
10. Carach, C. and M.J. Gordon, *Optical Measures of Thermally Induced Chain Ordering and Oxidative Damage in Polythiophene Films*. The Journal of Physical Chemistry B, 2013. **117**(6): p. 1950-1957.
11. An, L., et al., *Effect of thermal annealing on the microstructure of P3HT thin film investigated by RAIR spectroscopy*. Vibrational Spectroscopy, 2013. **68**(0): p. 40-44.
12. Miller, S., et al., *Investigation of nanoscale morphological changes in organic photovoltaics during solvent vapor annealing*. Journal of Materials Chemistry, 2008. **18**(3): p. 306-312.
13. Yun, J.-J., et al., *Insight into the Raman shifts and optical absorption changes upon annealing polymer/fullerene solar cells*. Applied Physics Letters, 2008. **92**(25): p. -.
14. Wang, X., et al., *High-Resolution Spectroscopic Mapping of the Chemical Contrast from Nanometer Domains in P3HT:PCBM Organic Blend Films for Solar-Cell Applications*. Advanced Functional Materials, 2010. **20**(3): p. 492-499.
15. Tsoi, W.C., et al., *The Nature of In-Plane Skeleton Raman Modes of P3HT and Their Correlation to the Degree of Molecular Order in P3HT:PCBM Blend Thin Films*. Journal of the American Chemical Society, 2011. **133**(25): p. 9834-9843.
16. Meyer, M.W., et al., *Scanning Angle Raman Spectroscopy of Poly(3-hexylthiophene)-Based Films on Indium Tin Oxide, Gold, and Sapphire Surfaces*. ACS Applied Materials & Interfaces, 2013. **5**(17): p. 8686-8693.
17. Gao, Y., et al., *Resonance Raman Spectroscopic- and Photocurrent Imaging of Polythiophene/Fullerene Solar Cells*. The Journal of Physical Chemistry Letters, 2009. **1**(1): p. 178-182.
18. Janssen, G., et al., *Optimization of morphology of P3HT/PCBM films for organic solar cells: effects of thermal treatments and spin coating solvents*. The European Physical Journal - Applied Physics, 2007. **37**(03): p. 287-290.
19. Reish, M.E., et al., *A Spectroscopic and DFT Study of the Electronic Properties of Carbazole-Based D–A Type Copolymers*. The Journal of Physical Chemistry C, 2012. **116**(40): p. 21255-21266.
20. Jameh-Bozorghi, S. and H.S. Il Beigi, *Theoretical study on the electronic, structural, properties and reactivity of a series of mono-, di-, tri- and tetrafluorothiophenes as*

- monomers for new conducting polymers*. Journal of Fluorine Chemistry, 2011. **132**(3): p. 190-195.
21. Staniec, P.A., et al., *The Nanoscale Morphology of a PCDTBT:PCBM Photovoltaic Blend*. Advanced Energy Materials, 2011. **1**(4): p. 499-504.
 22. Sun, Y.-P. and C.E. Bunker, *C70 in solvent mixtures*. Nature, 1993. **365**(6445): p. 398-398.

Table 1: Spin coating, drying, and thermal conditions for the different polymers.

Polymer	Symbol in text	Ratio ¹	RPM ²	Time (s) ²	Drying	Thermal annealing	Thickness (nm) ⁴
P3HT	P3HT ^α	1:1	600	40	Ambient	NA	277 ± 3
	P3HT ^β	1:1	600	40	Solvent ³	NA	278 ± 5
	P3HT ^γ	1:1	1000	40	Ambient	NA	180.6 ± 0.7
	P3HT ^Δ	1:1	1000	40	Ambient	100 °C; 600 s	170 ± 20
PCDTBT	PCDTBT ^α	1:3.5	600	40	Ambient	NA	180 ± 10
	PCDTBT ^β	1:3.5	600	40	Solvent ³	NA	170 ± 20
	PCDTBT ^γ	1:3.5	1500	40	Ambient	NA	111 ± 8
	PCDTBT ^Δ	1:3.5	1500	40	Ambient	80 °C; 600 s	81 ± 3
PTB7	PTB7 ^α	1:1.5	600	60	Ambient	NA	160 ± 10
	PTB7 ^β	1:1.5	600	60	Solvent ³	NA	190 ± 10
	PTB7 ^γ	1:1.5	1000	60	Ambient	NA	114 ± 4
	PTB7 ^Δ	1:1.5	1000	60	Ambient	80 °C; 600 s	103 ± 6

Footnote 1: Ratio of polymer to fullerene acceptor PCBM.

Footnote 2: Parameters used for spin coating.

Footnote 3: Solvent used was 1,2-dichlorobenze

Footnote 4: As determined by profilometry.

Table 2: Different statistical parameters associated with the solar polymers as well as quantitative determinations from collected Raman spectra.

Polymer	Symbol in text	Power (μW)	FWHM (cm^{-1})	Peak Location (cm^{-1})	S/N
P3HT	P3HT ^{α}	50	34.4 ± 0.6	1452.1 ± 0.3	51 ± 7
	P3HT ^{β}	50	31.3 ± 0.4	1450.3 ± 0.2	65 ± 8
	P3HT ^{γ}	50	33.3 ± 0.5	1451.1 ± 0.3	62 ± 8
	P3HT ^{Δ}	50	32.5 ± 0.3	1450.9 ± 0.2	73 ± 9
PCDTBT	PCDTBT ^{α}	100	22.2 ± 0.2	1449.07 ± 0.09	50 ± 10
	PCDTBT ^{β}	100	22.1 ± 0.2	1449.05 ± 0.07	60 ± 8
	PCDTBT ^{γ}	100	22.3 ± 0.4	1449.0 ± 0.2	39 ± 4
	PCDTBT ^{Δ}	100	22.4 ± 0.4	1448.7 ± 0.2	34 ± 5
PTB7¹	PTB7 ^{α}	100	20.9 ± 0.8	1496.0 ± 0.2	49 ± 5
	PTB7 ^{β}	100	21 ± 1	1496.2 ± 0.4	50 ± 10
	PTB7 ^{γ}	100	22.1 ± 0.8	1495.0 ± 0.3	44 ± 5
	PTB7 ^{Δ}	100	21 ± 1	1495.5 ± 0.4	40 ± 6

Footnote 1: The confidence in the fit of PTB7 is reduced due to the convolution of peaks and the rapid evolution of luminescence during measurement.

Table 3: Statistical parameters derived from Raman spectroscopic measurements for thermally annealed PCDTBT:PCBM.

Polymer	Thermal annealing	Power (μW)	FWHM (cm^{-1})	Peak Location (cm^{-1})	S/N
PCDTBT	80 °C; 600 s	100	21.8 ± 0.2	1447.2 ± 0.1	40 ± 10
	200 °C; 600 s	100	22.3 ± 0.3	1446.8 ± 0.2	70 ± 10

Table 4: Different statistical parameters associated with the solar polymers at selected powers for initial and end time points for P3HT and PCDTBT.

	Symbol In text	Power (μW)	FWHM (cm^{-1}) at t_0	FWHM (cm^{-1}) at t_{end}	Peak Location (cm^{-1}) at t_0	Peak Location (cm^{-1}) at t_{end}
P3HT	P3HT ^{α}	50	34.1 ± 0.7	35.3 ± 0.4	1454.1 ± 0.1	1452.5 ± 0.1
	P3HT ^{α}	500	34.4 ± 0.2	35.1 ± 0.3	1453.00 ± 0.05	1448.69 ± 0.09
	P3HT ^{α}	5000	34.3 ± 0.1	36.3 ± 0.4	1452.0 ± 0.1	1449.0 ± 0.3
	P3HT ^{β}	50	31.3 ± 0.4	31.23 ± 0.09	1451.29 ± 0.05	1450.67 ± 0.06
	P3HT ^{β}	500	31.3 ± 0.2	34.8 ± 0.8	1451.02 ± 0.05	1447.4 ± 0.3
	P3HT ^{β}	5000	32.03 ± 0.09	36.4 ± 0.5	1450.5 ± 0.1	1448.1 ± 0.2
	P3HT ^{γ}	50	34.73 ± 0.07	34.0 ± 0.9	1453.65 ± 0.09	1451.49 ± 0.05
	P3HT ^{γ}	500	35.4 ± 0.3	37.8 ± 0.8	1453.40 ± 0.04	1448.2 ± 0.4
	P3HT ^{γ}	5000	34.1 ± 0.3	36.4 ± 0.05	1451.36 ± 0.06	1448.3 ± 0.2
	P3HT ^{Δ}	50	32.2 ± 0.3	32.2 ± 0.5	1451.8 ± 0.1	1451.0 ± 0.1
	P3HT ^{Δ}	500	32.6 ± 0.1	36.8 ± 0.5	1451.5 ± 0.1	1447.5 ± 0.1
	P3HT ^{Δ}	5000	33.6 ± 0.2	36 ± 1	1450.30 ± 0.06	1448.9 ± 0.2
PCDTBT	PCDTBT ^{α}	100	22.2 ± 0.6	22.9 ± 0.6	1449.00 ± 0.04	1448.33 ± 0.07
	PCDTBT ^{α}	500	22.1 ± 0.2	24.0 ± 0.3	1448.69 ± 0.05	1447.32 ± 0.07
	PCDTBT ^{α}	5000	23.0 ± 0.1	25 ± 1	1447.75 ± 0.06	1446.5 ± 0.7
	PCDTBT ^{β}	100	22.2 ± 0.3	23.3 ± 0.4	1449.01 ± 0.06	1448.3 ± 0.1
	PCDTBT ^{β}	500	22.2 ± 0.2	23.8 ± 0.2	1448.77 ± 0.02	1447.4 ± 0.1
	PCDTBT ^{β}	5000	23.7 ± 0.2	25 ± 1	1447.4 ± 0.1	1446.3 ± 0.2
	PCDTBT ^{γ}	100	22.0 ± 0.6	21.8 ± 0.8	1449.07 ± 0.08	1448.3 ± 0.2
	PCDTBT ^{γ}	500	23.0 ± 0.7	26 ± 1	1448.5 ± 0.5	1447 ± 1
	PCDTBT ^{γ}	5000	22.4 ± 0.1	27.3 ± 0.9	1448.8 ± 0.2	1446.8 ± 0.2
	PCDTBT ^{Δ}	100	22.5 ± 0.8	22.9 ± 0.6	1449.3 ± 0.3	1448.16 ± 0.06
	PCDTBT ^{Δ}	500	22.9 ± 0.2	24.9 ± 0.2	1448.5 ± 0.1	1447.1 ± 0.2
	PCDTBT ^{Δ}	5000	28 ± 3	27 ± 2	1450.6 ± 0.6	1446.8 ± 0.8

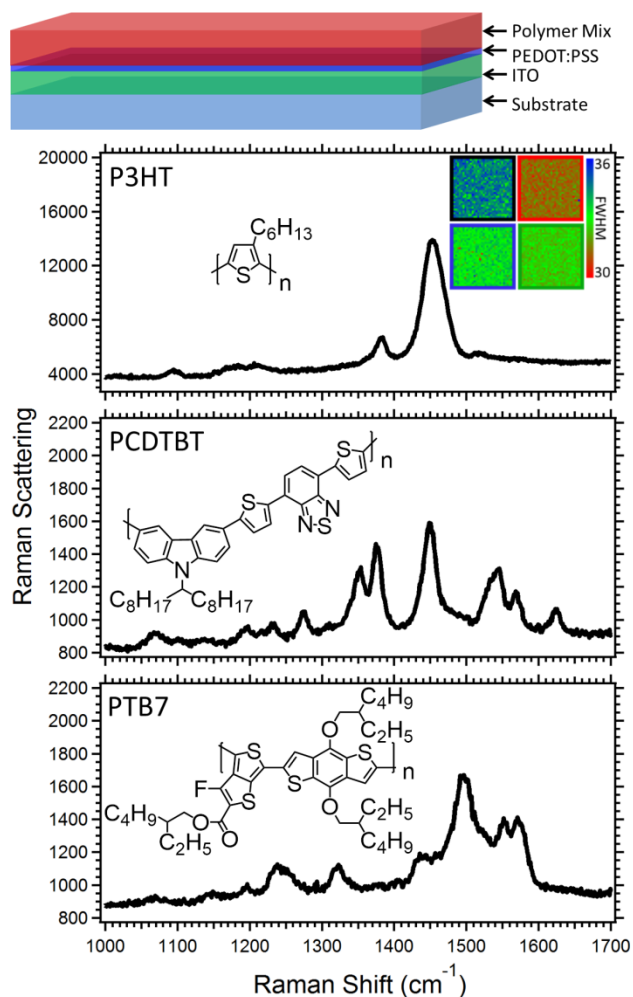


Figure 1: Depiction (top) of a solar cell with the different strata labeled. The bottom portion contains structures for different polymer donors that are mixed with the acceptor PCBM along with the Raman spectra of the structures. P3HT:PCBM, PCDTBT:PCBM, and PTB7:PCBM all were formed without annealing steps and had thicknesses of 180.6 ± 0.7 nm, 180 ± 10 nm, and 160 ± 10 nm, respectively. Inset of P3HT displays images of the P3HT:PCBM film with the outline color coded to the conditions used. (P3HT α [black], P3HT β [red], P3HT γ [blue], and P3HT Δ [green])

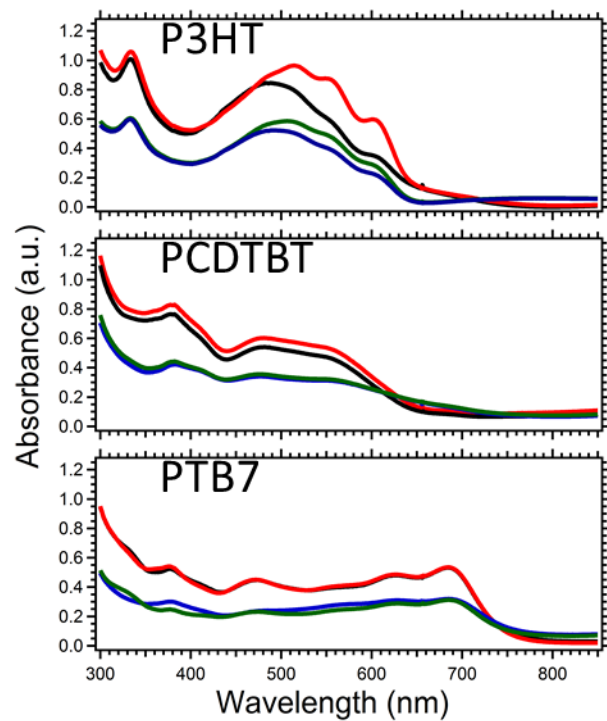


Figure 2: UV-Vis spectra for the three polymers under conditions of spin coating at slower relative rpm with slow drying (red) and fast drying (black) of the polymer as well as spin coating at higher rpm with fast drying (green) and fast drying with thermal annealing (blue).

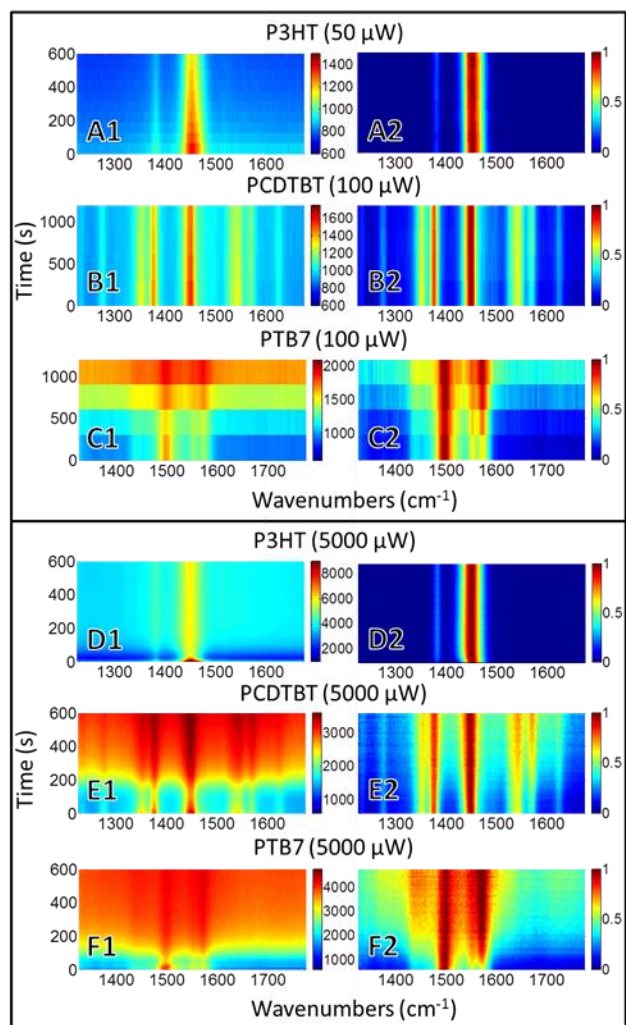


Figure 3: Raw data (A1-F1) versus normalized background subtracted data (A2-F2) presented for Raman spectra versus time.

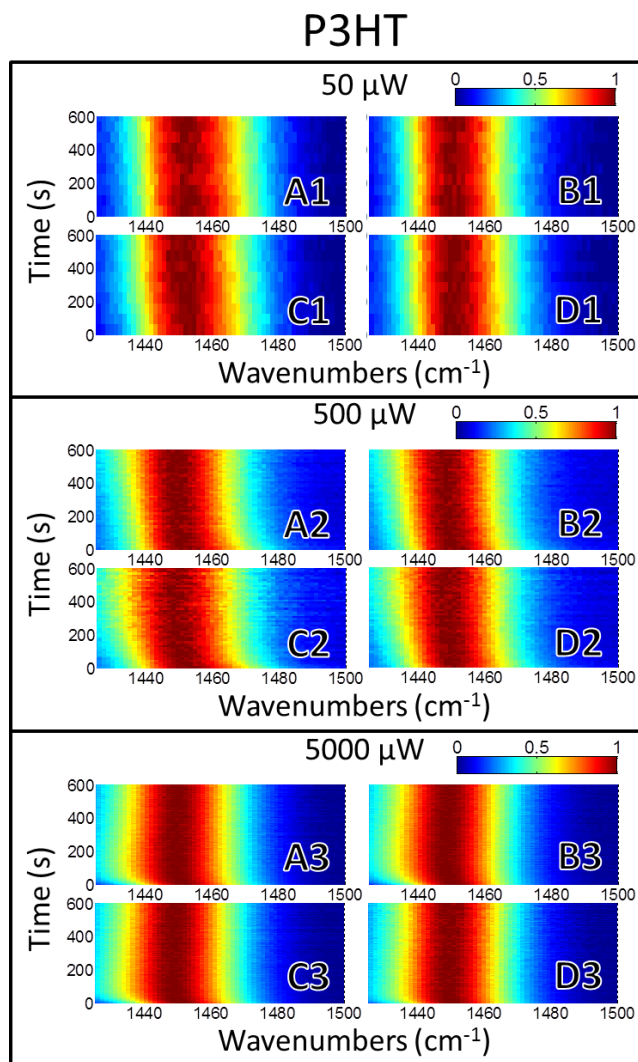


Figure 4: An expanded view of the normalized thiophene peak in P3HT:PCBM versus time for increasing excitation powers for conditions P3HT^α (A1-A3), P3HT^β (B1-B3), P3HT^γ (C1-C3), and P3HT^Δ (D1-D3).

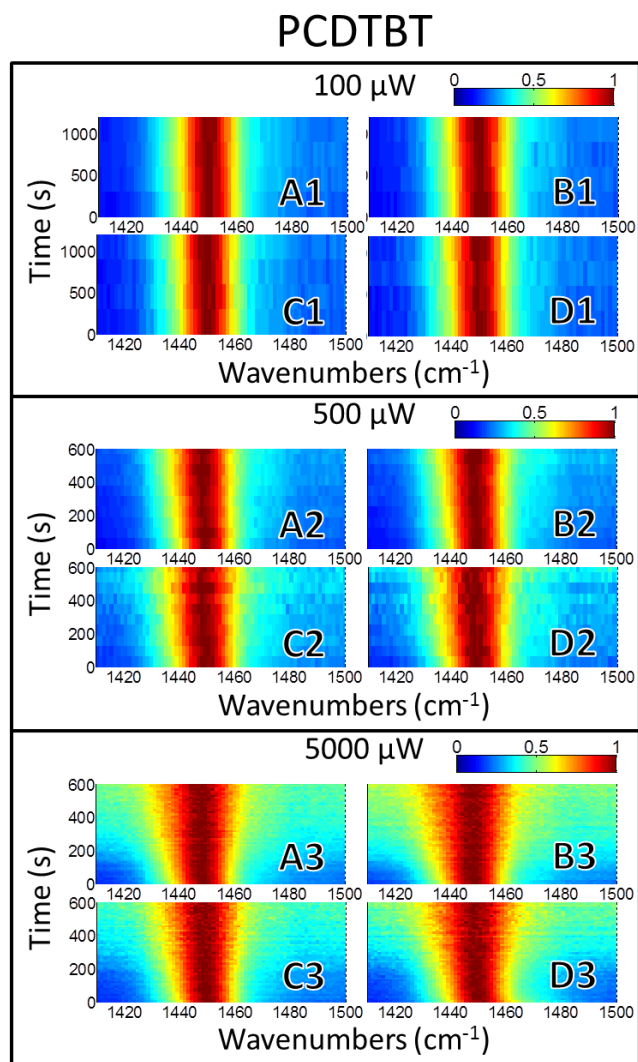


Figure 5: An expanded view of the normalized thiophene peak in PCDTBT:PCBM versus time for increasing excitation powers for conditions PCDTBT ^{α} (A1-A3), PCDTBT ^{β} (B1-B3), PCDTBT ^{γ} (C1-C3), and PCDTBT ^{Δ} (D1-D3).

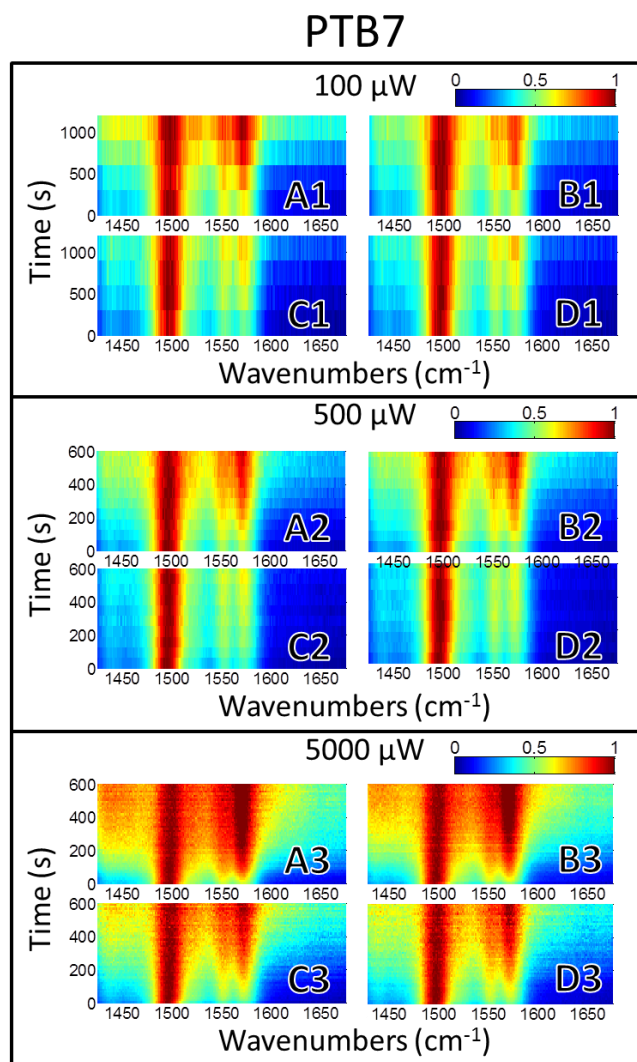


Figure 6: An expanded view of the normalized thiophene peak in PTB7:PCBM versus time for increasing excitation powers for conditions PTB7 ^{α} (A1-A3), PTB7 ^{β} (B1-B3), PTB7 ^{γ} (C1-C3), and PTB7 ^{Δ} (D1-D3).

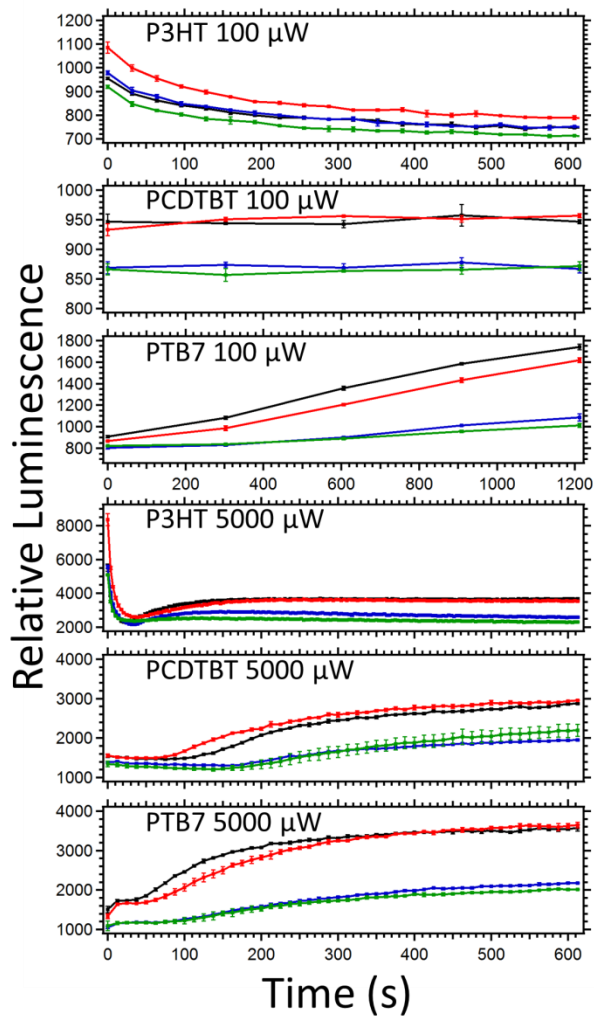


Figure 7: Luminescence changes in the background of the polymers Raman spectra visualized at $\sim 2000 \text{ cm}^{-1}$.

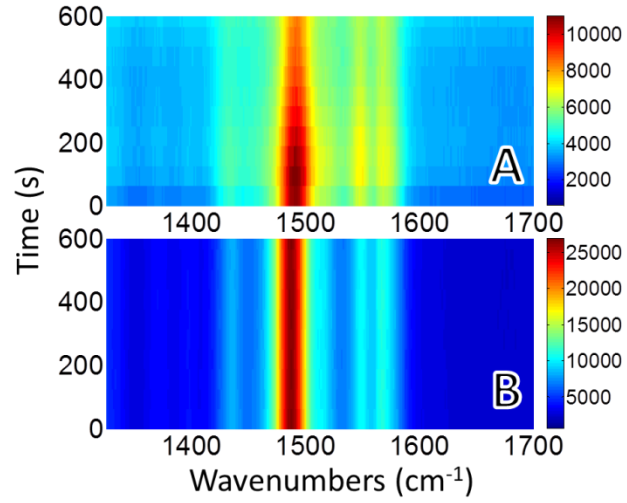


Figure 8: PTB7:PCBM measured at the exposed portion of the solar cell (A) and under the aluminum contact (B).

Chapter 6 : Conclusion

The primary focuses of this thesis were: (1) subdiffraction instrumentation for imaging of biological as well as novel inorganic samples, and (2) SA/conventional Raman instrumentation development with an emphasis on the examination of thin films and organic photovoltaics.

LD and STED microscopies were shown to achieve spatial resolutions of ≈ 40 nm for both traditional dyes and giant nanocrystal quantum dots. The actin network of cultured cells was elucidated with STED fluorescence lifetime imaging. Changes in local lifetime in the actin network could be attributed to the presence of quenchers such as tryptophan present in the cells. In living cells many structures are smaller than the diffraction limit of light and can be visualized with techniques such as STED. With faster scan times it would become possible to measure biological systems and changes that occur under dynamic conditions. In addition, kinetic information can be obtained. One of the downsides to STED imaging is that photobleaching is increased relative to confocal imaging and can limit the ability to observe a system for an extended period of time. The use of LD imaging with extremely photostable non-blinking giant nanocrystal quantum dots was one possible solution to the issue of photobleaching that occurred with STED microscopy. Giant nanocrystal quantum dots have shown stable emission on the order of days. Depletion of the luminescence emission was $\approx 92\%$ with LD. LD of giant nanocrystal quantum dots only required half the depletion energy to achieve a ≈ 40 -nm spatial resolution compared to STED measurements that used an Alexa Fluor 594-phalloidin conjugate. LD microscopy could achieve long term observation of biological systems with the steady highly photostable signal provided by giant nanocrystal quantum dots. In addition, replicate images of uniform intensity could ensure image fidelity in a raster scanning format.

Automated SA Raman spectroscopy in the visible spectrum can facilitate simple data collection with enhancement to signal from resonance conditions and high surface sensitivity. The developed instrumentation had an angle spread of $\approx 0.4^\circ$ and angle resolution of ≈ 0.09 . To accurately associate Raman spectra with the correct angle information, reflectivity data could be collected simultaneously. Thin films of polystyrene and PS-b-P3HT were measured with 532-nm excitation over angle ranges around their critical angles and compared to results from 785-nm excitation. Resonant conditions at 532-nm allowed for total collection times from 0.25 to 5 seconds to be used for a thin layer of PS-b-P3HT with signal-to-noise ratios of 30 and 120, respectively. The use of automated instrumentation can streamline data collection by improving repeatability over manual instrumentation. In addition, an increased throughput from automation allows the observation of samples with a greatly decreased operation time versus manual instrumentation. For ultra-thin films less than 200 nm Raman signal can be very weak, however, under resonant conditions ultra-thin films can be measured with high signal-to-noise ratios and sub-second collection times. The ability to perform measurements rapidly allows for kinetic measurements.

Resonance Raman spectroscopy achieves high signal in a conventional epi-illumination direction and can determine chemical and structural information useful for quantitation and image generation. Order and stability of solar heterojunction films comprised of P3HT:PCBM, PCDTBT:PCBM, and PTB7:PCBM were examined. The FWHM and peak location of thiophene groups were used to determine order. PCDTBT:PCBM and PTB7:PCBM were determined to be optimized as cast and P3HT:PCBM was shown to undergo improvements in relative order when solvent or thermally annealed. Accelerated laser induced photodegradation was observed to degrade all the heterojunction films. Such measurements obtained with a

conventional format were possible due to a sample throughput that was greatly increased with resonance Raman spectroscopy. The decrease in collection time also makes it possible to image samples with signal-to-noise ratios well above the limit of quantitation.